

Topics in Higgs Physics and Dark Matter

by

Gage Bonner

A thesis submitted to the Faculty of Graduate and
Postdoctoral Affairs in partial fulfillment of the
requirements for the degree of

Master of Science

in

Physics

Ottawa-Carleton Institute for Physics
Carleton University
Ottawa, Ontario

©2016, Gage Bonner

Abstract

This thesis is organized into two independent parts. In the first part, we study the prospects for constraining the Higgs boson's couplings to up and down quarks using kinematic distributions in Higgs production at the CERN Large Hadron Collider. With 3000 fb^{-1} of data in the four-lepton decay channel, we find that the Higgs p_T distribution can be used to constrain these couplings with precision competitive to other proposed techniques. We find $-0.73 \lesssim \bar{\kappa}_u \lesssim 0.33$ and $-0.88 \lesssim \bar{\kappa}_d \lesssim 0.32$, where $\bar{\kappa}_q = (m_q/m_b)\kappa_q$ and κ_q is a multiplicative factor that modifies the Standard Model q quark Yukawa coupling. We consider some prospects for improving this method by using additional decay channels.

In the second part of the thesis, we perform the standard thermal relic abundance calculation for a generic WIMP for three different forms of the self-annihilation cross section. We apply a numerical integration technique from the mathematical literature that does not appear to be well-known, but is particularly suited to this problem. First we consider s-wave annihilation and show that we are able to reproduce well-known results in the literature for the required cross section as a function of dark matter mass. Next we consider p-wave annihilation, $\sigma v_{\text{rel}} = \beta v_{\text{rel}}^2/c^2$ and show that the general

shape of the required value of β is similar to the s-wave case but about an order of magnitude larger. The canonical estimate of thermally averaging the cross section at $T = m_{\text{DM}}/20$ underestimates the general magnitude of the required value of β by a factor of ≈ 2 . We point out that, in the case where the effective number of relativistic degrees of freedom is constant, the required cross section for s and p-wave annihilation is a logarithmically increasing function of the dark matter mass. This is relevant when the dark matter mass is greater than about 10^3 GeV. Finally, we consider the case in which the dark matter annihilates through a scalar mediator with mass and width equal to the Standard Model Higgs boson mass and width.

Acknowledgments

I'm not a monkey, I'm a scientist!

Winston, *Overwatch*

I would like to thank:

My supervisor Prof. Heather Logan for effectively teaching me every useful thing I know about particle physics.

Andrea Peterson for helping me to get started with MadGraph (especially the NLO calculations) and for generously providing the HEFT model file.

My peers Will Scott and Alex Poulin for their helpful discussions about physics and especially for their helpful discussions about everything else.

Past iterations of myself for working on this thesis instead of goofing around.

My friends and family for putting up with me.

Statement of Originality

All of the content presented in this thesis is the original work of the author. The MadGraph model file which employs the extension of the HEFT discussed in Section 4.3 was provided by Andrea Peterson. The Möbius scheme discussed in Section 9 was introduced in Ref. [81] as a generic mathematical tool. Their method is applied to a physical problem in a way that, to the best of our knowledge, has not been done before. The implementation of the effective relativistic degrees of freedom $g(T)$ shown in Figure 10 benefited from discussions with Alex Poulin.

Contents

Abstract	i
Acknowledgments	iii
Statement of Originality	iv
Contents	v
List of Tables	ix
List of Figures	xi
List of Appendices	xvii
1 General Introduction	1
2 Introduction to Part 1	4
3 Where do the quark masses come from?	10
3.1 The Dirac Equation and Handedness	11
3.2 QED	13
3.3 The Higgs Mechanism	19
3.4 Quarks In the Standard Model	25

4	Higgs Production in Hadron Collisions	32
4.1	Parton Distribution Functions	32
4.2	The Constraint From the $pp \rightarrow h \rightarrow 4\ell$ Rate	36
4.3	MadGraph Simulations	46
4.4	Numerical Cross Sections	47
5	Constraints From Simulated Kinematic Data	53
5.1	The Asymmetry Parameter	53
5.2	Optimization of p_{cut}	58
5.3	Constraints From the Asymmetry Parameter	62
6	Discussion and Conclusions to Part 1	66
7	Introduction to Part 2	71
8	Theoretical Foundations of Dark Matter Freeze-Out	76
8.1	Introduction to Freeze-Out	76
8.2	The Effective Relativistic Degrees of Freedom	78
8.3	The Relic Density Equation	83
8.3.1	S-Wave Annihilation	87
8.3.2	P-Wave Annihilation	88

8.3.3	Resonant Annihilation	89
9	Integration of the Boltzmann Equation Using Möbius Schemes	94
9.1	Preliminary Computations	94
9.2	Introduction to Möbius Schemes	95
9.3	Application to the Relic Density	100
9.4	Comparison with Runge-Kutta	104
9.5	Far-field Approximations	108
9.6	Summary of Algorithm	112
10	Results	114
10.1	S-Wave	114
10.2	P-Wave	115
10.3	Resonant Annihilation Through the Higgs Pole	128
11	Conclusions to Part 2	131
	Appendices	134
A	Statistical Uncertainty On the Asymmetry	134
B	Group Theory	135
B.1	Introduction to Groups	136

B.2	Group Classification	137
B.3	Representations	138
B.4	Reducible Representations	142
B.5	Lie Groups	145
B.6	Generators	148
B.7	Lie Algebras	150
C	Fitting Functions	151
C.1	Fit: $g(T)$	152
C.2	Fit: $g_D(T)$	154
C.3	Fit: $\mathcal{G}(m_\chi, x = 100)$	157
D	Evaluation of the Thermally Averaged Resonant Annihilation Cross Section	160
	References	165

List of Tables

1	Cross sections and decay widths at leading order from MadGraph simulations.	48
2	Cross sections and decay widths at next-to-leading order from MadGraph simulations.	49
3	Simulated branching ratios from MadGraph.	50
4	Efficiency coefficients for $h \rightarrow 4\ell$ computed using MadGraph for the lepton acceptances in Eqs. (38) and (39).	51
5	Numerical constraint coefficients computed using MadGraph simulated data with LO decay partial widths.	52
6	Numerical constraint coefficients computed using partial widths extracted from Ref. [61] (see text for details.)	52
7	Asymmetry parameters for each production process calculated using optimized cuts at LO and NLO.	61
8	Expected number of observed events for gluon-initiated Higgs decay to four leptons. The error on the asymmetry is σ_A	63
9	Constraints on the couplings from the NLO contours of Figure 9.	64

10	The effect of enhanced light quark Yukawa couplings equal to the tightest constraints (at 3000 fb^{-1} ; see Figure 9 and Table 9) obtained from the asymmetry parameter analysis. The quantities in square brackets are the percentage increases in the SM Higgs total width or SM gluon-initiated Higgs production cross section assuming the couplings given in the first column.	67
11	Intrinsic degrees of freedom g_χ for various particle types. . . .	112
12	Coefficients of Eq. (136) for this work.	152
13	Coefficients of Eq. (136) for $g(T)$ in Figure 5 of Ref. [67]. . .	153
14	Coefficients of Eq. (137) for this work.	154
15	Coefficients of Eq. (137) for [67].	154
16	Coefficients of Eq. (138) for this work.	157
17	Coefficients of Eq. (138) using $g(T)$ in Figure 5 of Ref. [67]. .	157

List of Figures

1	The basic particle content of the Standard Model.	2
2	Parton density functions at a factorization scale equal to the Higgs mass ≈ 125 GeV. This is the PDF set NNPDF2.3_QED [55] with every PDF shown as its central value. This plot was made using the NNPDF Mathematica interface [56].	35
3	The leading order Feynman diagrams for quark and gluon fusion.	39
4	Some real next-to-leading order Feynman diagrams for quark and gluon fusion which lead to interference.	39
5	The dominant Feynman diagram for the decay $h \rightarrow 4\ell$	42
6	Sample momentum distributions (p_T and p_z) for $xx \rightarrow h \rightarrow 4\ell, x = g, u, d$ at leading order from 10,000 generated events. Gray is for gluons, solid black is for up quarks and dashed black is for down quarks.	54
7	The same as Fig. 6 but at next-to-leading order.	55
8	The same as Fig. 7 but without the lepton rapidity cut in Eq. (39).	60

9	Coupling constraints from p_T at leading order (dashed) and next-to-leading order (solid) at 300 fb^{-1} (gray) and 3000 fb^{-1} (black) obtained from requiring that A_T be within $\pm 2\sigma_A$ (Table 8) of the SM prediction - pure gluon fusion. Note that the case of 30 fb^{-1} is not good enough to put any constraints on the couplings, as is the case of A_z	65
10	The number of effective relativistic degrees of freedom $g(T)$ of Ref. [67] (black line) and this work (blue line). Note that Ref. [67] only shows $g(T)$ for $-3 < \log_{10}(T) < 3$, so the values of T outside this range were extrapolated.	84
11	Convergence analysis of two different Möbius schemes for s-wave annihilation. The black dots correspond to $a(t) = 0$ and the black line has equation $y = 2.01x + 3.24$. The red dots correspond to $a(t) = b(t)c(t)$ and the red line has equation $y = 2.19x + 2.52$	102

12	<p>The value of α as a function of m_χ for s-wave annihilation with $g_\chi = 2$ using the Möbius scheme of Algorithm 1. For s-wave annihilation, the thermally averaged cross section is equal to α. Results are shown using the $g(T)$ of Ref. [67] (gray line) and this work (black line). The dashed horizontal black line is the canonical value $\langle\sigma v_{\text{rel}}\rangle = 3 \times 10^{-26} \text{cm}^3 \text{s}^{-1}$.</p>	116
13	<p>The effect of the number of internal degrees of freedom g_χ on the required cross section for s-wave annihilation. The particle types corresponding to each g_χ are given in Table 11. These results were all calculated using the $g(T)$ of this work and the Möbius scheme of Algorithm 1. Note that the general magnitude of α increases with increasing g_χ.</p>	117
14	<p>The value of β as a function of m_χ for p-wave annihilation with $g_\chi = 2$ using the Möbius scheme of Algorithm 1. For p-wave annihilation, the thermally averaged cross section is equal to $6\beta/x$. Results are shown using the $g(T)$ of Ref. [67] (black line) and this work (blue line). The dashed horizontal black line is the canonical value $\beta = 1 \times 10^{-25} \text{cm}^3 \text{s}^{-1}$; see text for details.</p>	119

15	<p>The effect of the number of internal degrees of freedom g_χ on the required cross section for p-wave annihilation. The particle types corresponding to each g_χ are given in Table 11. These results were all calculated using the $g(T)$ of this work and the Möbius scheme of Algorithm 1. Note that the general magnitude of β increases with increasing g_χ.</p>	120
16	<p>Illustration of the increase of the required s-wave cross section at high masses. The red dots show the same calculation as in Figure 12. The cyan dots show the same calculation as in Figure 12, except with $g(T)$ set equal its maximum value g_{\max}. The blue line is the approximate analytic prediction of Eq. (128). All calculations in this Figure have been done using $g_\chi = 2$.</p>	125

17	<p>Illustration of the increase of the required p-wave cross section at high masses. The red dots show the same calculation as in Figure 14. The cyan dots show the same calculation as in Figure 14, except with $g(T)$ set equal its maximum value g_{\max}. The blue line is the approximate analytic prediction of Eq. (132). All calculations in this Figure have been done using $g_\chi = 2$.</p>	127
18	<p>The value of μ as a function of m_χ for resonant annihilation through a Standard Model Higgs boson (solid black line). For resonant annihilation, the thermally averaged cross section is given in Eqs. (82) and (83). The dashed black line is the expected cross section obtained by assuming that freeze-out happens exactly at $x = 20$ (see text for details). All results were calculated using $g_\chi = 2$; the results for $g_\chi = 1$ is negligibly different.</p>	130

19	The derivative term $g_D(T) = d(\ln g)/d(\ln T)$ of Ref. [67] (black line) and this work (blue line). Evidently the greatest disagreement occurs for $\log_{10} T \approx -1$, around the QCD phase transition. This is to be expected since we mostly ignored the details in this region.	156
20	The function $\mathcal{G}(m, x = 100)$ of Ref. [67] (black line) and this work (blue line).	159

List of Appendices

Appendix A: Statistical Uncertainty On the Asymmetry	134
Appendix B: Group Theory	135
Appendix C: Fitting Functions	151
Appendix D: Evaluation of the Thermally Averaged Resonant Annihilation Cross Section	160

1 General Introduction

Reader, this is Document.
Document, this is Reader.
Consider yourselves introduced.

Flip Tanedo, *Monte Carlo with Madgraph*

The Standard Model is a very successful theory which distills all of the knowledge of twentieth century particle physicists. The general idea is that all matter can be decomposed into fundamental particles called fermions, of which there are 12. Fermions are further subdivided into quarks and leptons, which each have 6 named members. The lightest particles are especially important because heavier particles will all decay down eventually. In particular, up and down quarks (the lightest “first generation” quarks; discovered first along with the strange quark) are the main constituents of the familiar proton and neutron. Fermions interact with one another via mediator particles called bosons, of which there are 4. These bosons explain three of the fundamental forces, excluding gravity. In our familiar proton, quarks are held together by the strong force which is mediated by gluons. In order to explain why most particles in the Standard Model are massive, there is an “extra” boson called the Higgs boson. A general overview of the particle content of the Standard Model is shown in Figure 1. Experimental evidence has shown that the Higgs mechanism, the mechanism by which

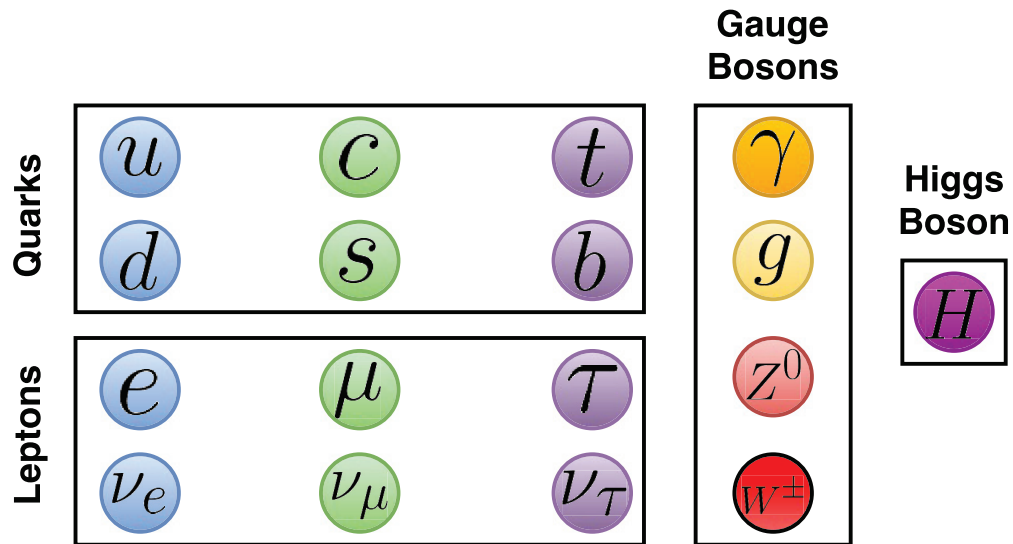


Figure 1: The basic particle content of the Standard Model.

the W and Z bosons specifically acquire mass, is consistent with Standard Model predictions. However, the question remains as to whether or not the same principle can be applied to all fermions as well. The situation looks promising for the heaviest quarks, but relatively little is known about the first generation quarks. This is mainly due to the fact that the Standard Model prediction of the interaction strength between the Higgs boson and a given fermion is proportional to the mass of the fermion. Hence, for very light fermions, this interaction is very weak and difficult to constrain without a great deal of statistics.

Despite all the triumphs of the Standard Model, there are several well-

known problems it can not solve (physics “beyond” the Standard Model). One of the most important is the issue of so-called dark matter - an exotic kind of matter which does not interact with light. Fortunately, dark matter does interact gravitationally and its effect on the rotational velocities of stars (among other factors) has led to the conclusion that it is even more abundant than “normal” matter. The problem for the Standard Model is that it does not contain a particle with all of the known properties of dark matter. One of the most promising candidates is a class of new particles called weakly interacting massive particles. We can infer, for example, the mass of these candidates using measurements of the amount of dark matter left over from the early Universe. This is vital information when attempting to build extensions of the Standard Model which hope to explain dark matter.

This thesis is organized into two independent parts, each of which addresses one of the previous issues. The first part introduces a novel method of constraining the Higgs couplings to light quarks. The second part provides helpful reference plots giving the required self-annihilation cross section and mass of a dark matter particle for consistency with observations. Each part contains a more detailed introduction with a section-by-section outline.

2 Introduction to Part 1

I don't know anything, but I do know that everything is interesting if you go into it deeply enough.

Richard Feynman, *The Pleasure of Finding Things Out*

If the Standard Model (SM) of particle physics is to be complete, then there must be a mechanism through which elementary particles acquire mass. The Higgs boson provides such a mechanism and an object with the required properties was recently observed by the ATLAS and CMS collaborations [1, 2]. We can test some of the predictions of the SM by studying the Higgs boson's couplings to other particles. The SM does not numerically predict these couplings directly; it postulates relatively simple expressions for their size in terms of other free parameters. Therefore, if we can measure these free parameters (particle masses, mixing angles etc.) while characterizing the strength of the Higgs couplings via its production and decay cross sections, we can determine whether or not the functional forms forecasted by the SM are correct. This gives us a clue as to whether or not the SM Higgs mechanism actually provides masses for all constituents of the SM. This thesis considers a new way to probe Higgs couplings to up and down quarks.

For heavy gauge bosons W and Z we expect the Higgs couplings to be equal to $2m_{W,Z}^2/v$ in the SM, where $v \approx 246$ GeV is the Higgs vacuum expect-

tation value. The measured couplings have been found to be consistent with the SM within experimental error [3, 4]. In the fermion sector, we expect the Higgs couplings to quarks q to be equal to m_q/v in the SM. This is also true for leptons, but we do not consider these couplings here. The quantities m_q/v are usually called the Yukawa couplings y_q . Since the couplings are linear in the quark masses, we expect Higgs-mediated processes to be dominated by the heavy (top and bottom) quark contributions. Indeed, Higgs production is controlled mainly by gluon fusion whereby two gluons initiate a heavy quark loop which ejects a Higgs boson. Since the mass of the Higgs is less than $2m_W, 2m_Z$ and $2m_t$, the heaviest particle to which it can decay is the bottom quark, the dominant mode. There are several experimental analyses which probe the Higgs couplings to the heavy (bottom and top) quarks [5, 6, 7, 8, 9, 10, 11, 12]. These are also found to be consistent with the SM prediction, so we conclude that the SM Higgs mechanism is a valid theory for the origin of the heavy gauge bosons' and quarks' masses.

The situation is less clear for lighter quarks. Constraining the light quark Yukawa couplings is important since there are alternate models in which they differ from the SM expectation [13, 14, 15, 16] or don't enter at all [17]. For constraints on charm and strange Yukawa couplings based on the

inclusive Higgs production rate, see Refs. [18, 19, 20, 21, 22]. Up and down quark Yukawa couplings are by far the hardest to constrain; without very efficient quark flavor tagging, it is nearly impossible to observe Higgs decays to up and down quarks. Furthermore, since the cross section for quark fusion $q\bar{q} \rightarrow h$ is proportional to y_q^2 , proton collisions are much more likely to result in $b\bar{b} \rightarrow h$ than $u\bar{u} \rightarrow h$ and $d\bar{d} \rightarrow h$ even though u, d are the valence quarks of the proton. In particular we have $m_u = 2.3_{-0.5}^{+0.7}$ MeV, $m_d = 4.8_{-0.3}^{+0.5}$ MeV and $m_b = 4.18 \pm 0.03$ GeV [23]; evidently, probing y_u and y_d will require a great deal of statistics.

It is customary to parametrize the deviation of the Yukawa couplings from their SM values by inserting a prefactor κ in front of the relevant y so the terms in the Lagrangian become $-\kappa_q y_q^{\text{SM}} \bar{q} q h$ where $\kappa_q = 1$ corresponds to the SM. We will adopt the convention of Ref. [26] where the quark couplings are all scaled relative to the bottom quark coupling. The bottom quark mass has a much smaller experimental uncertainty than the up and down quark masses and this rescaling facilitates comparisons with the literature. Since the Yukawa couplings are proportional to the relevant quark mass, we have

$$\kappa_q = \frac{m_b}{m_q} \bar{\kappa}_q, \tag{1}$$

where $\bar{\kappa}$ is the scaled coupling. The current tightest constraints on up and down quark Yukawa couplings come from Ref. [28]. They write down the observed cross section for gluon-initiated Higgs decays to two Z bosons in terms of the signal strength μ_{ggh} for gluon fusion (i.e. the SM signal strength for Higgs production). Given that $\mu_{ggh}^{\text{SM}} = 0.85_{-0.16}^{+0.19}$ [3], calculating this cross section as a function of the couplings leads to constraints at the 95% confidence level. They find that $-1.2 \lesssim \bar{\kappa}_u \lesssim 1.1$ and $-1.5 \lesssim \bar{\kappa}_d \lesssim 1.4$. If we fix every Higgs coupling to its SM expectation except for up, down and strange quarks, we can obtain $|\bar{\kappa}_u| < 0.98$ and $|\bar{\kappa}_d| < 0.93$ [26]. Recently, a completely different method for constraining y_u and y_d was proposed based on measuring isotope shifts in atomic clock transitions [24]. This method depends strongly on the precision of isotope shift measurements, but current data gives constraints comparable to the standard global fits. Yet another method is discussed in Ref. [25], where they show that direct detection searches for dark matter (assuming that Higgs-portal dark matter is discovered) can put upper bounds on the light quark Yukawa couplings, immediately leading to $|\bar{\kappa}_{u,d}| \lesssim 0.01$.

We study a complementary technique to constrain the Higgs couplings to up and down quarks using the Higgs boson production kinematics at the

LHC. The general idea is to write down an asymmetry parameter which only depends on the shape of the kinematic distributions. We expect Higgs-mediated decay products seen in a detector to be produced mainly by gluon fusion in the SM. If the shape of this distribution is sufficiently different from the shape of the same process initiated by quark fusion, then the asymmetry parameter will allow us to discriminate between them. There are good theoretical reasons to expect the kinematic distributions for Higgs production via $u\bar{u}$ or $d\bar{d}$ fusion to be different from those via gluon fusion. The Higgs transverse momentum, p_T , distribution is shaped mainly by the additional jet radiation from the initial-state partons, which is controlled by the strong charges and spins of the initial-state partons. Indeed, we find that the gluon-fusion process has a harder p_T distribution than quark-fusion, allowing these to be discriminated. We would also expect the Higgs longitudinal momentum in the detector frame, p_z , to be smaller (more central) in the gluon-fusion process and larger in the quark-fusion processes. However, after taking into account detector acceptance of the Higgs decay products in the four-lepton decay channel, the p_z distributions do not provide additional sensitivity. This distribution may be worthy of further study in the diphoton decay channel.

The organization of this part of the thesis is as follows. We begin with

Section 3, which contains a summary of some gauge theoretic aspects of the Standard Model along with an explanation of how the Higgs Mechanism generates fermion masses. In Section 4 we review some aspects of proton collisions and derive the condition on the gluon and up/down quark couplings which ensures that the total rate is like the SM. We compute cross sections, branching ratios and detection efficiencies for all the relevant processes with Monte Carlo simulation. Section 5 defines the main observable of our method and provides sample momentum distributions from simulations. We implement the method in a real-world context to obtain the expected constraints on the couplings. Finally, Section 6 summarizes our conclusions. There are two appendices that are relevant to Part 1. Appendix A contains a derivation of the statistical error on our observable and Appendix B contains a general review of some important aspects of group theory.

3 Where do the quark masses come from?

An author never does more damage to his readers than when he hides a difficulty.

Évariste Galois, *Deux mémoires d'Analyse pure*

No self-respecting architect leaves the scaffolding in place after completing the building.

Carl F. Gauss, quoted in *Mathematics and the Physical World*

The Standard Model is complicated. A complete description of the underlying group-theoretic structure that doesn't beg too many questions would be instructive, but certainly overkill. In any case, there exist a number of detailed descriptions of all the moving parts [29, 30, 31, 32, 33, 34, 35, 36] and we will not reproduce them here. That being said, it seems far too terse to simply start with phenomenological implications of the Higgs. In principle one could answer the question "Where do the quark masses come from?" with "They come from the Higgs." and be done with it. It is our goal to reach a compromise; we will provide a concise but plausible summary of the parts of the Standard Model required to understand the quark masses. It is likely that neither Galois nor Gauss would be satisfied.

3.1 The Dirac Equation and Handedness

In quantum field theory, particles are not treated as points but instead as excitation of fields ϕ_i which are functions of spacetime. For our purposes, we will take “spacetime” to be 3 + 1 dimensional Minkowski space with metric $\eta = \text{diag}(1, -1, -1, -1)$.

Consider a spin 1/2 particle of mass m . In natural units $c = \hbar = 1$ this particle is described by a four-component spinor field ψ by the Dirac equation

$$(i\gamma^\mu\partial_\mu - m)\psi = 0, \tag{2}$$

where ∂_μ is the covariant 4-derivative. Also, γ^μ for $\mu = 0, 1, 2, 3$ are the 4-dimensional gamma matrices which obey the algebra $\{\gamma^\mu, \gamma^\nu\} = 2\eta^{\mu\nu}I_4$ with I_4 being the 4×4 identity matrix. The Dirac equation is formulated such that it transforms in a consistent way under Lorentz transformations and we can say in the language of group theory that we require it to be invariant under the Lorentz group $SO(1, 3)$. What does this actually mean? Well, $SO(3)$ is a literal rotation in space, so $SO(1, 3)$ is some kind of general rotation through spacetime which takes into account spatial rotations and boosts (which happen when we “rotate through” time.) It can be shown that

$SO(1, 3)$ is isomorphic to $SU(2) \otimes SU(2)$, which very loosely means that this generalized rotation in Minkowski space can be written as two generalized rotations in distinct Minkowski subspaces. In other words, the structure of ψ is such that it Lorentz transforms as the direct product of two $SU(2)$ representations. This is a useful fact, since we're somewhat familiar with $SU(2)$ from spin. For a short review of some of the fundamentals of group theory, see Appendix B.

Let us consider the $j = 0$ and $j = 1/2$ representations of $SU(2)$, which accordingly correspond to particles of spin 0 and spin 1/2. For $j = 0$, the only representation which preserves the structure of $SU(2)$ is the trivial representation consisting of all unit matrices. This makes sense: since $j = 0$ has no spin it should be operated on by a representation of $SU(2)$ which does nothing; multiplication by a unit matrix accomplishes this. For $j = 1/2$, the generators are given by the Pauli matrices. The smallest representation of $SU(2) \otimes SU(2)$ is given when we use the $j = 0$ representation for each subspace. This is labeled as $(0, 0)$ and describes a scalar field. The next possibility is that we take one representation to be $j = 0$ and the other to be $j = 1/2$. The representation $(0, 1/2)$ is called the left-handed spinor representation and the representation $(1/2, 0)$ is called the right-handed spinor

representation. These two representations must always appear together as $(0, 1/2) \oplus (1/2, 0)$. This describes how spin $1/2$ Dirac spinors Lorentz transform (note that neutrinos, which are strictly left-handed, appear only as $(0, 1/2)$.) We can write the four-component spinor ψ as $\psi = (\psi_L, \psi_R)^T$ and then the left-handed field ψ_L transforms under $(0, 1/2)$ and the right-handed field ψ_R transforms under $(1/2, 0)$. When it is said that something “transforms as a singlet or doublet of $SU(2)$,” it means that it transforms under the $j = 0$ or $j = 1/2$ representations of $SU(2)$, respectively. As a final note, the representation where we take $j = 1/2$ twice describes the way in which spacetime 4-vectors transform.

3.2 QED

We will illustrate the basics of gauge field theory using the simplest example: quantum electrodynamics (QED). In terms of a Lagrangian density $\mathcal{L}(\phi_i, \partial_\mu \phi_i)$, the relativistic Euler-Lagrange equations state that

$$\partial_\mu \left(\frac{\partial \mathcal{L}}{\partial (\partial_\mu \phi_i)} \right) = \frac{\partial \mathcal{L}}{\partial \phi_i}, \quad (3)$$

where the index i runs over the total number of fields. One of the most important Lagrangians is the Dirac Lagrangian, which describes a model that contains one free spin 1/2 particle of mass m . In natural units $c = \hbar = 1$, we have

$$\mathcal{L}_{\text{Dirac}} = \bar{\psi}(i\gamma^\mu\partial_\mu - m)\psi. \quad (4)$$

In this case, ψ is a spinor field with four components and $\bar{\psi}$ is the adjoint spinor defined by $\bar{\psi} = \psi^\dagger\gamma^0$. The quantity $\bar{\psi}\psi$ is Lorentz invariant. One can easily show that by treating $\bar{\psi}$ and ψ as independent fields, applying Eq. (3) to Eq. (4) for $\bar{\psi}$ gives Eq. (2). By examining Eq. (4), we see that since all spacetime indices are contracted, the entire Lagrangian is Lorentz invariant. Since the Lagrangian is Lorentz invariant the theory is by definition consistent with relativity. Another quality of the Dirac Lagrangian is that it is invariant under the transformation $\psi \rightarrow e^{i\alpha}\psi$ where α is some real constant. The factor $e^{i\alpha}$ passes through the derivatives and cancels with its complex conjugate since $\bar{\psi} \rightarrow e^{-i\alpha}\bar{\psi}$. This property is called global phase invariance; evidently multiplying a Dirac spinor by $e^{i\alpha}$ doesn't change the physics. In some ways, this is trivial since multiplying the Dirac Lagrangian by any constant doesn't change the equations of motion. The more interesting question is what happens to the Dirac Lagrangian under the transforma-

tion $\psi \rightarrow e^{i\alpha(x)}\psi$. Now the phase depends on the spacetime coordinate, so if the Lagrangian is invariant under this transformation, it is said to be locally phase invariant. As it is written, Eq. (4) is not locally phase invariant; in fact we have that

$$\mathcal{L}_{\text{Dirac}} \rightarrow \mathcal{L}_{\text{Dirac}} - (\bar{\psi}\gamma^\mu\psi)\partial_\mu\alpha. \quad (5)$$

If we want the Dirac Lagrangian to be locally phase invariant, we need to add something to it to cancel out the term $-(\bar{\psi}\gamma^\mu\psi)\partial_\mu\alpha$. By inspection, it seems like we're stuck with the factor $(\bar{\psi}\gamma^\mu\psi)$ so we could try to add a term like $(\bar{\psi}\gamma^\mu\psi)A_\mu$ for some new field A_μ . The modified Dirac Lagrangian would then read

$$\mathcal{L}_{\text{Dirac}+} = \mathcal{L}_{\text{Dirac}} + (\bar{\psi}\gamma^\mu\psi)A_\mu. \quad (6)$$

It's easy to see that if A_μ changes under a local phase transformation as $A_\mu \rightarrow A_\mu + \partial_\mu\alpha$ then Eq. (6) is invariant. Therefore, we can impose local phase invariance on the Dirac Lagrangian at the expense of introducing this new field A_μ . However, by applying the Euler-Lagrange equations for A_μ to this modified Dirac Lagrangian, we see that they read $\bar{\psi}\gamma^\mu\psi = 0$, which seems to defeat the original purpose. We still need to add another term which must depend on $\partial_\nu A_\mu$ to obtain something non-trivial. We know from

electrodynamics that the four-potential $A_\mu = (\phi, \mathbf{A})$ solves Maxwell's equations and is also invariant under the transformation $A_\mu \rightarrow A_\mu + \partial_\mu \alpha$. To wit, we recall the free Maxwell Lagrangian

$$\mathcal{L}_{\text{Maxwell}} = -\frac{1}{16\pi} F^{\mu\nu} F_{\mu\nu}, \quad (7)$$

where $F_{\mu\nu} = \partial_\mu A_\nu - \partial_\nu A_\mu$. Indeed, operating on Eq. (7) with the Euler-Lagrange equations recovers the source-free Maxwell equations and one can easily verify that it is invariant under $A_\mu \rightarrow A_\mu + \partial_\mu \alpha$. Therefore, we can interpret A_μ as the field of a photon. But wait, does it have to be a photon? Could we also insert a term like $m A_\mu A^\mu$ into the Lagrangian and thereby obtain a massive gauge boson? Well, under a local phase transformation, we have

$$A_\mu A^\mu \rightarrow A_\mu A^\mu + (A_\mu \partial^\mu + A^\mu \partial_\mu) \alpha + (\partial_\mu \alpha)(\partial^\mu \alpha), \quad (8)$$

which is clearly not invariant. Therefore, we see that the price of introducing a mass term for the boson is that the Lagrangian is no longer locally phase invariant. For this reason, we will only consider massless gauge bosons for now. Let us write $\alpha(x) \rightarrow q\alpha(x)$ for a real constant q (for now, this is conventional). Adding the Maxwell Lagrangian to the modified Dirac Lagrangian

gives

$$\mathcal{L}_{\text{QED}} = \mathcal{L}_{\text{Dirac}} + \mathcal{L}_{\text{Maxwell}} + q(\bar{\psi}\gamma^\mu\psi)A_\mu. \quad (9)$$

This is the Lagrangian of a model that contains a massive spin 1/2 particle ($\mathcal{L}_{\text{Dirac}}$) and a photon ($\mathcal{L}_{\text{Maxwell}}$) plus their interactions in the extra term $q(\bar{\psi}\gamma^\mu\psi)A_\mu$. In other words, \mathcal{L}_{QED} describes electrons, positrons and photons, which justifies its name.

We can now introduce and explain some of the jargon of gauge theory. One can think of the transformation $\psi \rightarrow e^{i\alpha(x)}\psi$ as a set of transformations given by $U = e^{i\alpha(x)}$ and write $\psi \rightarrow U\psi$. Since $U^\dagger U = 1$, we have that U is a unitary transformation. Since it is a 1×1 matrix (i.e. a number) it is referred to as the $U(1)$ group. A Lagrangian that is invariant under transformations from the $U(1)$ group is said to possess $U(1)$ gauge invariance where, as in electrodynamics, the function $\alpha(x)$ is the gauge function. So if we take the free Dirac Lagrangian (free electrons and positrons) and require that the Lagrangian be $U(1)$ gauge invariant, we get an additional field (photons) and some interactions. In general, by taking a fermion Lagrangian and imposing a local gauge invariance with transformations given by a unitary group G_U , we introduce massless boson fields (remember that Eq. (8) shows that mass terms for the bosons are not gauge invariant) plus some interactions. This is

why most bosons are called gauge bosons in the Standard Model. This also explains why it is said that a given interaction is a G_U interaction. In the previous example, electrodynamics constitutes a $U(1)$ interaction since it has $U(1)$ gauge invariance. The actual content of electrodynamics enters in the term $q(\bar{\psi}\gamma^\mu\psi)A_\mu$ which contains the new field A_μ . This field is a boson and it couples to the fermion fields with strength q . In this case, the interpretation of q is naturally the elementary electric charge e . Therefore, through the term $q(\bar{\psi}\gamma^\mu\psi)A_\mu$, the field A_μ serves the purpose of telling electrons and positrons about each others' electric charge. This is why it is said that photons mediate the electromagnetic force.

The general idea of promoting a global symmetry to a local one is usually calculated most quickly using the minimal coupling rule. If we replace the ∂_μ in Eq. (4) with the covariant derivative $D_\mu = \partial_\mu - iqA_\mu$ it is easy to show that this is equivalent to $U(1)$ gauge invariance. In particular, under the transformation $\psi \rightarrow e^{i\alpha(x)}\psi$ we have $D_\mu\psi \rightarrow e^{i\alpha(x)}D_\mu\psi$ as long as $A_\mu \rightarrow A_\mu + (1/q)\partial_\mu\alpha(x)$. In group theoretic language, ψ has $U(1)$ charge q and in general there is a charge (not necessarily electric) associated with every gauge group. Another thing to note is that $U(1)$ is an Abelian group with only one generator (namely, the number 1). More complicated gauge theories will

be non-Abelian and will have many generators. Fortunately, the minimal coupling rule still works in these situations.

The problem with this whole setup so far is that it seems like we can only have massless gauge bosons. This is fine for the photon and gluon but we know from experiment that at least the W and Z bosons should have mass. This is where the Higgs mechanism comes into play; we will now see how we can give a gauge boson a mass with this method.

3.3 The Higgs Mechanism

Spontaneous symmetry breaking is a phenomenon in which there exists some setup with symmetry and Nature is forced to “take a stand” and break it. We can imagine pushing straight down on a vertical plastic rod. This configuration has cylindrical symmetry, but if we push with enough force, the rod will eventually bend in some direction which breaks the symmetry. Alternatively, one can imagine a 2-dimensional ball at the bottom of a parabolic well. If we suddenly create a small hill for the ball to rest on, the ball will have to decide whether to roll to the left or right to get to the bottom of the well. It is not known which direction the ball will pick, but in either case, the left-right symmetry of the setup is broken. We can apply the same idea

to particle physics. More specifically, this spontaneous symmetry breaking is the cornerstone of the Higgs mechanism [37, 38]. We will see how it can be used to give a mass to the photon in the QED theory (this is sometimes called the Abelian Higgs model [39]).

We introduce the Higgs boson generally as a complex scalar field. If the field is free, we can describe it in terms of the Klein-Gordon Lagrangian. However, we will add a term quartic in the fields and define the Higgs potential

$$V(\Phi) = \mu^2\Phi^*\Phi + \lambda|\Phi^*\Phi|^2, \quad (10)$$

which means that the Higgs Lagrangian is simply

$$\mathcal{L}_{\text{Higgs}} = \partial_\mu\Phi^*\partial^\mu\Phi - V(\Phi). \quad (11)$$

Now we can add this to the QED Lagrangian Eq. (9) to see how it will give the photon a mass. Calling it a photon is somewhat misleading (it's really just some gauge boson) but the language is familiar so we will continue this way for now. We also need to replace the partial derivative in Eq. (11) with

the covariant derivative $D_\mu = \partial_\mu - iqA_\mu$. Therefore, we have

$$\mathcal{L}_{\text{Higgs+QED}} = \mathcal{L}_{\text{QED}} + D_\mu \Phi^* D^\mu \Phi - V(\Phi). \quad (12)$$

Much like in the case of the Dirac Lagrangian, Eq. (12) is invariant under transformations of the form $\Phi \rightarrow e^{i\alpha(x)}\Phi$ which we now know is equivalent to saying that Eq. (12) is invariant under $U(1)$. Furthermore, Φ now has $U(1)$ charge q . The real Higgs boson is electrically neutral so clearly this model is not completely accurate, but it does illustrate all the main ideas.

Now let us examine the potential $V(\Phi)$ more closely. We will write $\Phi = re^{i\theta}$ so that the potential can be expressed as

$$V(\Phi(r, \theta)) = \lambda r^2(\mu^2/\lambda + r^2). \quad (13)$$

If $\lambda < 0$ the potential can become arbitrarily negative so there is no real ground state and we must take $\lambda > 0$. Now, if $\mu^2 > 0$ the potential is strictly positive with one local minimum exactly at $r = 0$. In this case, since the ground state (vacuum) corresponds to $\Phi_{\text{min}} = 0$ we say that Φ has zero vacuum expectation value. Finally, we turn to the most interesting case where μ^2 is negative. Now we have a local minimum when $r^2 = -\mu^2/2\lambda > 0$.

Since the form of the potential only contains terms like $\Phi^*\Phi$, it is insensitive to changes in θ , so the minimum of the potential is a ring of radius $r_{\min} = \sqrt{-\mu/2\lambda}$. In other words, we have $\Phi_{\min} = r_{\min}e^{i\theta}$ where θ is arbitrary. Clearly, Φ now has a nonzero vacuum expectation value. It is conventional to define the vacuum expectation value v as $v = \sqrt{-\mu/\lambda}$ so we have $\Phi_{\min} = (v/\sqrt{2})e^{i\theta}$.

We've effectively done the same thing that we did to the ball at the bottom of the well. In this case, Φ has not taken a stand as to which direction it will 'roll' because we still have the factor of $e^{i\theta}$ left over. Furthermore, the Lagrangian is still invariant under $U(1)$ transformations. The $U(1)$ symmetry does not appear to be broken, because this is not the "true" Lagrangian. That isn't to say that it's incorrect, but rather that we want to express Lagrangians in terms of variations of fields about their minima i.e. their vacuum expectation values. This is necessary in order to perturbatively calculate functions which depend on the fields. In the case of QED, the Dirac field and the photon field each have zero expectation value so everything just works. In our new Higgs/QED theory, the Higgs has a vacuum expectation value of $v/\sqrt{2}$, so we should rewrite the field as an expansion around this. Again, we begin with $\Phi = re^{i\theta}$ but now $r = (v+h)/\sqrt{2}$ where h now has zero

expectation value. Variations in h correspond to variations up and down the hills of the Higgs potential. Variations in θ corresponds to rotations around the origin which all have the same energy. Therefore excitations of the field corresponding to θ cost zero energy, so it must be massless. These massless fields are called Goldstone bosons, and they always show up when a global symmetry is spontaneously broken [40]. For a gauged symmetry they are unphysical and we would like to remove them.

We can get rid of the Goldstone bosons by making the $U(1)$ transformation $\Phi \rightarrow e^{-i\theta(x)}\Phi$ which leads to $\Phi = (v + h)/\sqrt{2}$. However, since the $U(1)$ invariance is broken in the vacuum, a $U(1)$ transformation on Φ will have an apparent effect on the Lagrangian. We know that under a $U(1)$ transformation, the covariant derivative transforms as $D_\mu\Phi \rightarrow e^{-i\theta(x)}D_\mu\Phi$ as long as $A_\mu \rightarrow A_\mu + (1/q)\partial_\mu\theta(x)$. Substituting $\Phi = (v + h)/\sqrt{2}$ along with the transformation rules into Eq. (12) gives

$$\begin{aligned}
\mathcal{L}_{\text{Higgs+Massive QED}} &= \frac{1}{2}\partial_\mu h\partial^\mu h - \frac{1}{2}M_h^2 h^2 \\
&\quad - \frac{1}{4}F_{\mu\nu}F^{\mu\nu} + \frac{1}{2}M_A^2 A_\mu A^\mu \\
&\quad - \sqrt{\frac{\lambda}{2}}M_h h^3 - \frac{1}{4}\lambda h^4 \\
&\quad + qM_A A_\mu A^\mu h + \frac{1}{2}q^2 A_\mu A^\mu h^2 + \mathcal{L}_{\text{Dirac+}}, \tag{14}
\end{aligned}$$

where $M_A = qv$ and $M_h = \sqrt{2}\mu$. Before we discuss what this means, let's return to the issue of $U(1)$ invariance. We started with Eq. (12), which was manifestly $U(1)$ invariant. Then, we used this fact to rotate Φ in such a way that it does not introduce the unphysical Goldstone bosons. The Lagrangian is still invariant under $U(1)$ transformations since we could in principle just rotate back the other way. However, when we choose a particular $U(1)$ transformation, it is said that we have “fixed” the gauge because the gauge function $\theta(x)$ is known. In particular, it's whatever it needs to be to make Φ strictly real; this is called the unitary gauge. Then, we can write $\Phi = (v + h)/\sqrt{2}$ to express the Lagrangian in terms of the field h which has zero vacuum expectation value. It is this translation that apparently breaks the $U(1)$ invariance of the Lagrangian - it's clear that Eq. (14) is not invariant under $h \rightarrow e^{i\alpha}h$. However, the physics can't change just because we made a rotation and wrote Φ in terms of h so obviously this is still the same system as Eq. (12). The $U(1)$ invariance isn't really broken so much as it is hidden.

Now let's look at the new Lagrangian more closely. The first line in Eq. (14) is exactly the Lagrangian of a scalar field of mass M_h ; this is “the” Higgs boson. The second line is the Proca Lagrangian: the Lagrangian of a spin 1 particle of mass M_A . The third line contains the Higgs self-interaction terms

and fourth line contains the interactions between the Higgs and the photon plus the modified Dirac Lagrangian from Eq. (6) (electrons and positrons plus their interaction with the photon). In any case, we see that the Higgs mechanism has in fact generated a mass for the photon. Now we see why calling A_μ a photon was misleading - what we really have is a massive gauge field. This toy model is essentially analogous with the rest of the Standard Model. We have fermions described by the Dirac equation which interact with each other through mediation by gauge bosons. In order to give the gauge bosons a mass, we introduce the Higgs mechanism. Now that we have some intuition about the function of the Higgs boson, we can finally discuss quark masses in the Standard Model.

3.4 Quarks In the Standard Model

So far, we've gotten away with only talking about $U(1)$ interactions, i.e. QED. The Standard Model contains a $U(1)$ interaction, but the charge is not necessarily equal to the electric charge of the particles, it is a generalized quantity called the hypercharge. We assign hypercharges to particles to reproduce their electric charges Q via $Q = Y + T_3$, where Y is the hypercharge and T_3 is the third generator of $SU(2)$.

To model the weak interaction, the Standard Model contains an $SU(2)$ gauge interaction. It is an experimental fact that the weak interaction violates parity [41, 42], which can be implemented by giving left and right handed fermions different representations under $SU(2)$. Left handed fermions participate in the weak interaction and so transform as doublets of $SU(2)$. We can write the left-handed first generation quarks in the field $q_L = (u_L, d_L)^T$. Recall that the doublet representation of $SU(2)$ has generators given by $\sigma^a/2$, where σ^a are the Pauli matrices, so under an $SU(2)$ transformation we have $q_L \rightarrow \exp(-i\omega^a \sigma_a/2)q_L$. Right handed fermions do not participate in the weak interaction and so transform as singlets of $SU(2)$. We can write the right-handed first generation quarks as the fields u_R, d_R where under an $SU(2)$ transformation they are invariant.

We would like these quarks to have masses and therefore, since they are spin 1/2 fermions, we look to the Dirac Lagrangian. Given the fact that we're forced to deal with left and right handed fermions separately, we must write $\psi = \psi_L + \psi_R$ in Eq. (4). Considering the mass term $m\bar{\psi}\psi$, we quickly find that it can be expressed as $m\bar{\psi}_L\psi_R + m\bar{\psi}_R\psi_L$. Under an $SU(2)$ transformation, the right handed fields are invariant, but the left handed fields contribute an exponential factor. No modification of the covariant derivative will save this

term, so we must conclude that gauge invariance implies that the quarks (and in fact, all fermions) should be massless. This is where the Higgs mechanism enters.

The true Higgs of the Standard Model is an $SU(2)$ doublet of complex scalars, which means it can be written as $\Phi = (\phi^+, \phi^0)^T$, where $\phi^+ = (\phi_1 + i\phi_2)/\sqrt{2}$ and $\phi^0 = (\phi_3 + i\phi_4)/\sqrt{2}$ with ϕ_i all real scalar fields [43]. The Higgs potential is still given by Eq. (10) which again has a minimum at $|\Phi|^2 = \mu^2/2\lambda$. As we saw previously, one can write Φ in “polar form” with some radial part multiplied by an exponential. In this case the exponential in general contains 2×2 matrices which are related to the Pauli matrices. The exact form isn’t important here since in any case the Lagrangian will be explicitly constructed to be $SU(2)$ invariant so we can get rid of this exponential factor with an $SU(2)$ rotation. This is exactly analogous to the QED + Higgs model where we got rid of a factor like $\exp(i\theta)$ with a $U(1)$ rotation. The final result is the same, except in this case the Higgs is a doublet so we’ll have $\Phi = (0, (v + h)/\sqrt{2})^T$.

Let’s return to the task at hand. If the masses of the quarks don’t come from the Dirac Lagrangian, where do they come from? The answer comes in the form of the Yukawa interaction, which postulates a form for the in-

teraction between the Higgs and the fermions. Since the Higgs is an $SU(2)$ doublet, it must enter into the Lagrangian with an $SU(2)$ anti-doublet to preserve $SU(2)$ invariance. The only candidate is the conjugate (i.e. anti-particle) left-handed quark field \bar{q}_L . By definition, the Higgs has $U(1)$ hypercharge equal to $1/2$. Hence, the combination $\bar{q}_L\Phi$ has effective hypercharge $1/2 - 1/6 = 1/3$. In order to preserve $U(1)$ invariance, we need to multiply by an $SU(2)$ singlet with hypercharge $-1/3$. The only candidate is the right handed down quark field d_R which has both of these properties, again, by definition. Therefore, we declare that the term $-y_d\bar{q}_L^i\Phi_i d_R$ is invariant under $U(1) \otimes SU(2)$ and is valid to insert into the Lagrangian. The real constant y_d (note that technically it can be complex, but that is beyond the scope of this thesis) is referred to as the Yukawa coupling; in this case it is specifically the down Yukawa coupling. If we take the complex conjugate of the entire Yukawa term to get $-y_d\bar{d}_R\Phi_i^\dagger q_L^i$, we note that this is also invariant under $U(1) \otimes SU(2)$, so we need to keep both factors together. Substituting our expressions for the quark field and the transformed Higgs field, we find

$$-y_d\bar{q}_L^i\Phi_i d_R - y_d\bar{d}_R\Phi_i^\dagger q_L^i \rightarrow -\left(\frac{y_d v}{\sqrt{2}}\right)\bar{d}d - \left(\frac{y_d}{\sqrt{2}}\right)h\bar{d}d, \quad (15)$$

where we have used the fact that $\bar{d}d = \bar{d}_L d_R + \bar{d}_R d_L$. Comparing the first term with the Dirac Lagrangian, we see that the factor in brackets must be the mass of the down quark. In other words, we have $m_d = y_d v / \sqrt{2}$; the factor of $\sqrt{2}$ is usually absorbed into y , but we will leave it there for now. Furthermore, the second term is an interaction between the Higgs and a down/anti-down quark pair with coupling given by $y_d / \sqrt{2}$. We conclude that measuring the coupling strength of the Higgs to the down quark allows us to test this prediction of the Standard Model, namely whether or not the relationship $m_d = y_d v / \sqrt{2}$ is actually valid.

Obviously the situation should be nearly identical for the up quark, but the argument is slightly more complicated. We're tempted to switch the symbols u and d and just write $-y_u \bar{q}_L^i \Phi_i u_R$, but u_R has hypercharge $2/3$, giving an effective hypercharge of 1. If Φ had hypercharge $-1/2$ but still transformed like a doublet of $SU(2)$, that term would have the required gauge invariance.

The solution is to replace Φ by the conjugate Higgs doublet, given by $\Phi_i^c = \epsilon_{ij} \Phi^{j*}$, where ϵ_{ij} is the Levi-Civita symbol. Under an $SU(2)$ transformation, we have $\Phi^* \rightarrow \exp(i\omega^a \sigma_a^* / 2) \Phi^*$. By inspection, we see that $\sigma_1^* = \sigma_1$, $\sigma_2^* = -\sigma_2$ and $\sigma_3^* = \sigma_3$; these matrices also satisfy the algebra of $SU(2)$ and therefore

so do $(-\sigma_1, \sigma_2, -\sigma_3)$. One can show with a short calculation that the Levi-Civita matrix satisfies $\epsilon \exp(i\omega^a \sigma_a^*/2) \epsilon^{-1} = \exp(-i\omega^a \sigma_a/2)$. This is exactly the definition of unitary equivalence, so Φ^c transforms like a doublet of $SU(2)$ [44]. Furthermore, since the third generator of $SU(2)$ is now $-\sigma_3/2$ instead of $\sigma_3/2$, the conjugate Higgs doublet has hypercharge $-1/2$ as required. To summarize, our new term in the Lagrangian from which we expect to extract the up quark mass is $-y_u \bar{q}_L^i \Phi_i^c u_R$ plus its complex conjugate. Since the transformed Higgs field is just $\Phi^c = ((v+h)/\sqrt{2}, 0)^T$, we quickly find

$$-y_u \bar{q}_L^i \Phi_i^c u_R - y_u \bar{u}_R \Phi_i^{c\dagger} q_L^i \rightarrow -\left(\frac{y_u v}{\sqrt{2}}\right) \bar{u}u - \left(\frac{y_u}{\sqrt{2}}\right) h \bar{u}u. \quad (16)$$

We see that the right hand side of Eq. (16) is the same as the right hand side of Eq. (15), except with u and d switched. The implication is that the mass of the up quark is given by $m_u = y_u v/\sqrt{2}$ and its coupling to the Higgs is given by $y_u/\sqrt{2}$.

This concludes our discussion on the origin of the up and down quark masses in the Standard Model. There is still perhaps the lingering issue of how one could hope to determine the mass of an up or down quark experimentally if they can not be isolated. A full discussion is far beyond the scope

of this thesis, but the general idea is to use lattice QCD to compare the free quark masses in terms of the known spectrum of meson masses. See Ref. [47] for a broad overview and Ref. [48] for recent detailed calculations.

In any case, we see that the interaction strength between the Higgs and the up/down quarks will allow us to test the Standard Model prediction that $m_q = y_q v / \sqrt{2}$. We will now turn to the more phenomenological arguments which will allow us to do just that.

4 Higgs Production in Hadron Collisions

A man concerned about the state of his soul will not usually be much helped by thinking about the spheres or the structure of the atom.

C. S. Lewis, *The Discarded Image*

4.1 Parton Distribution Functions

We would like to study collisions between protons. We now know that protons are composed of three valence quarks (uud) along with a sea of quark/antiquark pairs continuously being created and destroyed from the vacuum. The entire proton is held together by strong color interactions mediated by gluons. When dealing with composite objects, we need to take into account the large range of energy scales at which the various interactions can occur. For example, when two protons collide at a very high energy (i.e. a hard collision) the main interaction may be a quark/antiquark pair annihilating into a Higgs boson. This constitutes a hard interaction and can be described by a perturbative QCD calculation. However, there will also be several low energy interactions (i.e. soft collisions) such as initial and final state radiation (technically part of the main hard collision, though they can be soft). Byproducts of the interactions will cascade away from the main collision zone

and undergo a chain of soft interactions until they eventually recombine into hadrons which are seen in the detector. This entire process is called the parton shower and can be numerically simulated by tools such as Pythia 6 [58] and Herwig++ [57].

In order to deal with these complicated hadron collisions, we turn to the parton model [45, 46]. The general idea is to write a proton-proton collision as the convolution of a hard process (calculable in QCD perturbation theory) and a soft process which takes everything else into account. The separation between the two regimes is referred to as factorization and occurs at the factorization scale μ . The cross section for a collision between protons which results in the final state X is given by

$$\sigma(pp \rightarrow X) = \sum_{a,b \in \{q,\bar{q},g\}} \int dx_a dx_b f_a(x_a, \mu^2) f_b(x_b, \mu^2) \hat{\sigma}(ab \rightarrow X; x_a, x_b). \quad (17)$$

Let us examine the components of this formula. First of all, $\hat{\sigma}(ab \rightarrow X; x_a, x_b)$ is the cross section for the partons a and b to produce X , assuming a and b are essentially free. This cross section is the cross section of an assumed hard process and can therefore be computed in perturbation theory. This cross section depends on x_a and x_b which correspond to the fraction of the

relevant proton's momentum that parton a or b carries. Evidently if x_a and x_b are small, $\hat{\sigma}(ab \rightarrow X; x_a, x_b)$ becomes soft and the calculation is no longer perturbative. In order to account for this, the hard cross section is integrated over all possible momentum fractions, weighted by $f_i(x, \mu^2)$ for each parton. The function $f_i(x, \mu^2)$ is a process-independent factor that contains all of the soft physics; its dependence on x is determined through experiment. The physical interpretation is that $f_i(x, \mu^2)$ represents the probability that parton i has momentum fraction x at factorization scale μ . For this reason, we call f the parton distribution function (PDF) - one can define PDFs for any hadron, but here we are only concerned with protons. Plots of the PDFs for the most relevant partons are shown in Figure 2.

As we can see from Figure 2 most of the momentum of the proton is carried by up and down quarks, which is exactly as expected since these are the valence quarks. We also see that, for example, the strange quark carries much less momentum than the up/down quarks. This is also true for the bottom quark, but we have not shown it to avoid clutter. The reason $\sigma(s\bar{s} \rightarrow h)$ is much higher than $\sigma(u\bar{u} \rightarrow h)$ or $\sigma(d\bar{d} \rightarrow h)$ is simply because the strange quark is much more massive. Of particular interest to us is the observation that gluons have a very high probability of being soft, whereas the quarks

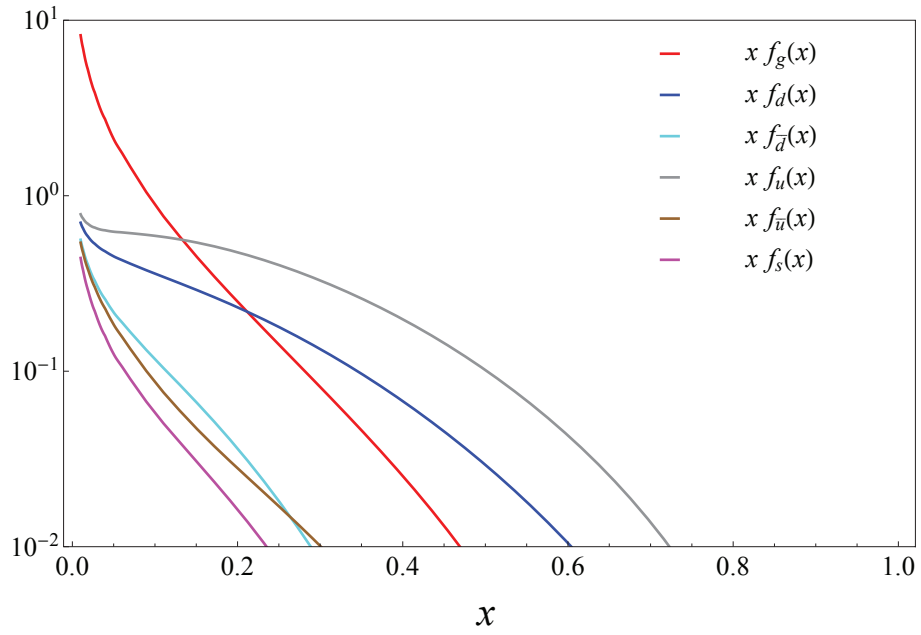


Figure 2: Parton density functions at a factorization scale equal to the Higgs mass ≈ 125 GeV. This is the PDF set NNPDF2.3_QED [55] with every PDF shown as its central value. This plot was made using the NNPDF Mathematica interface [56].

are generally shifted to higher values of x . This would suggest that the $|p_z|$ distribution (the momentum distribution along the proton beam axis) of processes initiated by quark fusion should be centered at a higher value than the $|p_z|$ distribution of processes initiated by gluon fusion. Perhaps more importantly, if we compare the distribution of u/d with the corresponding distribution of \bar{u}/\bar{d} , we see that the antiquark distributions, like the other sea quark distributions, are ≈ 10 times lower than the valence quark distributions. The implication is that when two protons collide and we have an event like $u\bar{u} \rightarrow h$, we would expect the event to be significantly asymmetric since the u should, on average, have much more momentum than the \bar{u} . On the other hand, clearly gluon fusion should be symmetric on average which will ideally let us distinguish it from the quark fusion process.

4.2 The Constraint From the $pp \rightarrow h \rightarrow 4\ell$ Rate

We consider $pp \rightarrow h \rightarrow 4\ell$, with $\ell = e$ or μ . The background for the four-lepton final state is created mainly by direct ZZ^* production via quark and gluon fusion [53]. The reason for using the 4ℓ final state is that this

background is very small, and we ignore it here. The rate for this process is

$$R(pp \rightarrow h \rightarrow 4\ell) = \sigma(pp \rightarrow h) \cdot \text{BR}(h \rightarrow 4\ell). \quad (18)$$

Let us first consider the cross section $\sigma(pp \rightarrow h)$. Note that we are ignoring other Higgs production mechanisms since these processes can be separated out using other kinematic features. At leading order (LO) we can separate gluon fusion and up/down quark fusion as

$$\sigma_{\text{LO}}(pp \rightarrow h) = \sigma_{\text{LO}}(gg \rightarrow h) + \sum_{q=u,d} \sigma_{\text{LO}}(q\bar{q} \rightarrow h). \quad (19)$$

In this case, the only two diagrams contributing to Higgs production are shown in Figure 3. The Higgs boson is a color singlet, so it can not interact directly with gluons. However, one can introduce an effective vertex (shown in Figure 3 as a black dot) which takes into account the fact that $gg \rightarrow h$ is mediated by a heavy quark loop. These diagrams are independent, so the matrix element for $pp \rightarrow h$ must be separable into two pieces which each correspond to just gluon fusion or quark fusion. At next-to-leading order (NLO) the situation is more complicated. When we add strong vertices to the LO diagrams, we create new diagrams which add corrections to each

process in Figure 3. We also create some diagrams of the forms in Figure 4. These diagrams have the same initial and final states, but different structure. The total matrix element is the sum of all the individual matrix elements and in this case, when we compute the absolute value, the individual terms mix which leads to an extra “interference” contribution. Since the matrix elements are complex, this term can be positive or negative, which is to say that it can increase or decrease the overall cross section. Put simply the total cross section will be the total cross sections for gluon and quark fusion, plus an extra cross section which takes into account interactions which are, in some sense, both of those. We therefore write

$$\sigma_{\text{NLO}}(pp \rightarrow h) = \sigma_{\text{NLO}}(gg \rightarrow h) + \sum_{q=u,d} \sigma_{\text{NLO}}(q\bar{q} \rightarrow h) + \sum_{q=u,d} \sigma_{\text{int}}^q, \quad (20)$$

for an interference cross section σ_{int}^q . It is understood that this is the cross section for interference between $q\bar{q}$ fusion and gluon fusion. The fusion amplitudes depend linearly on the effective ggh coupling y_g and the Yukawa couplings y_q and hence the cross sections are each proportional to y_g^2 and y_q^2 . Similarly, the interference term is proportional to $y_g y_q$. Let us introduce the multiplicative factors κ_g and κ_q such that $y_g = \kappa_g y_g^{\text{SM}}$ and $y_q = \kappa_q y_q^{\text{SM}}$; this

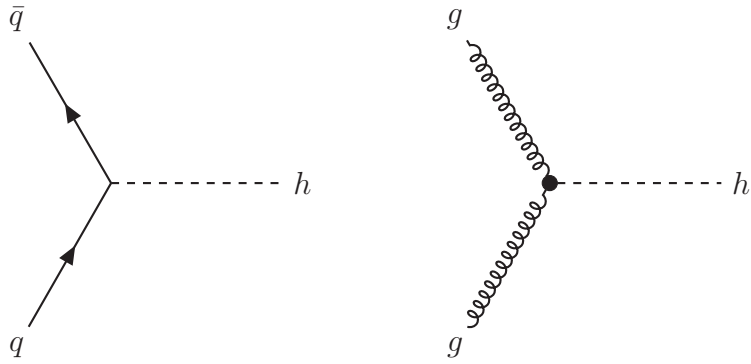


Figure 3: The leading order Feynman diagrams for quark and gluon fusion.

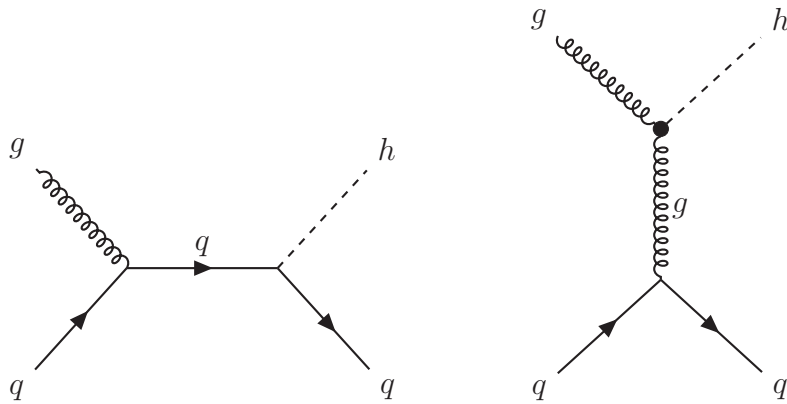


Figure 4: Some real next-to-leading order Feynman diagrams for quark and gluon fusion which lead to interference.

means that the SM has $\kappa_g = \kappa_q = 1$. Hence, we can factor out the couplings and write

$$\begin{aligned} \sigma(pp \rightarrow h) &= \kappa_g^2 \sigma_{gg \rightarrow h}(\kappa_g = 1) + \sum_{q=u,d} \kappa_q^2 \sigma_{q\bar{q} \rightarrow h}(\kappa_q = 1) \\ &\quad + \sum_{q=u,d} \kappa_g \kappa_q \sigma_{\text{int}}^q(\kappa_g = 1, \kappa_q = 1). \end{aligned} \quad (21)$$

Note that we have dropped the subscript identifying the order of the computation. This calculation is understood to be performed at NLO; one can convert it to explicitly LO by setting $\sigma_{\text{int}}^q = 0$. We would like to scale the quark couplings relative to the bottom quark coupling to compare our results with the literature. Since the SM prediction is that Yukawa couplings are proportional to the relevant quark mass, we have $y_q \propto m_q = (m_q/m_b)m_b \propto (m_q/m_b)y_b$. This quickly implies that $\kappa_q = (m_b/m_q)\bar{\kappa}_q$, where $\bar{\kappa}$ is the scaled coupling. Under this transformation, we see that

$$\begin{aligned} \kappa_q^2 \sigma_{q\bar{q} \rightarrow h}(\kappa_q = 1) &= \bar{\kappa}_q^2 (m_b/m_q)^2 \sigma_{q\bar{q} \rightarrow h}(\bar{\kappa}_q = m_q/m_b) \\ &= \bar{\kappa}_q^2 (m_b/m_q)^2 (m_q/m_b)^2 \sigma_{q\bar{q} \rightarrow h}(\bar{\kappa}_q = 1) \\ &= \bar{\kappa}_q^2 \sigma_{q\bar{q} \rightarrow h}(\bar{\kappa}_q = 1), \end{aligned} \quad (22)$$

which isn't surprising since the size of the cross section can't depend on how we label the couplings. Using Eq. (22), Eq. (21) becomes

$$\begin{aligned}
\sigma(pp \rightarrow h) &= \kappa_g^2 \sigma_{gg \rightarrow h}(\kappa_g = 1) + \sum_{q=u,d} \bar{\kappa}_q^2 \sigma_{q\bar{q} \rightarrow h}(\bar{\kappa}_q = 1) \\
&\quad + \sum_{q=u,d} \kappa_g \bar{\kappa}_q \sigma_{\text{int}}^q(\kappa_g = 1, \bar{\kappa}_q = 1) \\
&= \kappa_g^2 \sigma_{gg} + \sum_{q=u,d} \bar{\kappa}_q^2 \bar{\sigma}_{q\bar{q}} + \sum_{q=u,d} \kappa_g \bar{\kappa}_q \bar{\sigma}_{\text{int}}^q, \tag{23}
\end{aligned}$$

where we have defined the following

$$\sigma_{gg} \equiv \sigma_{gg \rightarrow h}(\kappa_g = 1), \tag{24}$$

$$\bar{\sigma}_{q\bar{q}} \equiv \sigma_{q\bar{q} \rightarrow h}(\bar{\kappa}_q = 1), \tag{25}$$

$$\bar{\sigma}_{\text{int}}^q \equiv \sigma_{\text{int}}^q(\kappa_g = 1, \bar{\kappa}_q = 1). \tag{26}$$

Now let us consider the branching ratio $\text{BR}(h \rightarrow 4\ell)$. The full process is primarily mediated by two Z bosons (where one is off-shell) as in Figure 5. We would like to write this branching ratio in terms of the κ couplings as we have already done with the cross section. Let $\Gamma_{\text{tot}}(h)$ be the partial width

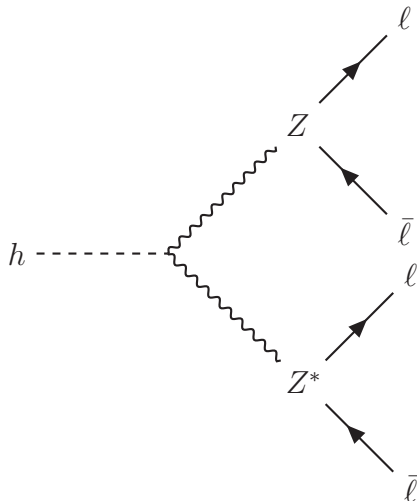


Figure 5: The dominant Feynman diagram for the decay $h \rightarrow 4\ell$.

for all possible Higgs decays. Then, by definition, we have

$$\text{BR}(h \rightarrow 4\ell) = \frac{\Gamma(h \rightarrow 4\ell)}{\Gamma_{\text{tot}}(h)}. \quad (27)$$

In the same manner as Eqs. (21) and (23), we can write the partial width for $h \rightarrow \bar{q}q$ as $\Gamma(h \rightarrow q\bar{q}) = \bar{\kappa}_q^2 \Gamma_{h \rightarrow q\bar{q}}(\bar{\kappa}_q = 1)$. The partial width for $h \rightarrow gg$ is $\Gamma(h \rightarrow gg) = \kappa_g^2 \Gamma_{h \rightarrow gg}(\kappa_g = 1)$. We can therefore decompose the total Higgs width as

$$\Gamma_{\text{tot}}(h) = \kappa_g^2 \Gamma_{h \rightarrow gg}(\kappa_g = 1) + \sum_{q=u,d} \bar{\kappa}_q^2 \Gamma_{h \rightarrow q\bar{q}}(\bar{\kappa}_q = 1) + \Gamma_{\text{else}}(h), \quad (28)$$

where $\Gamma_{\text{else}}(h)$ is the partial width for Higgs decay to anything else allowed in the SM other than gluons or up/down quarks. The largest contribution to this term comes from $h \rightarrow b\bar{b}$, followed by $h \rightarrow WW^*$. Substituting Eq. (28) into Eq. (27) gives

$$\text{BR}(h \rightarrow 4\ell) = \frac{\Gamma(h \rightarrow 4\ell)}{\kappa_g^2 \Gamma_{gg} + \sum_{q=u,d} \bar{\kappa}_q^2 \bar{\Gamma}_{q\bar{q}} + \Gamma_{\text{else}}}, \quad (29)$$

where we have dropped the argument of Γ_{else} (it will be implicit) and made the following definitions

$$\Gamma_{gg} \equiv \Gamma_{h \rightarrow gg}(\kappa_g = 1) \quad (30)$$

$$\bar{\Gamma}_{q\bar{q}} \equiv \Gamma_{h \rightarrow q\bar{q}}(\bar{\kappa}_q = 1). \quad (31)$$

Let us consider the quantity $\Gamma_{h \rightarrow q\bar{q}}(\bar{\kappa}_q = 1)$ as in Eq. (28). Since $\bar{\kappa}_q = 1 \implies y_q \rightarrow y_b$, one can show with a standard calculation that the partial width of the Higgs decay to $q\bar{q}$ at leading order is given by

$$\Gamma_{h \rightarrow q\bar{q}}(\bar{\kappa}_q = 1) = \frac{(y_b^{\text{SM}})^2 N_c}{16\pi} m_h \left[1 - \frac{4m_q^2}{m_h^2} \right]^{3/2}, \quad (32)$$

where $N_c = 3$ is the color factor which takes into account the possible colors of final state quarks. The factor in Eq. (32) in square brackets contains the term m_q/m_h which is much less than one for light quarks. The implication is that to a very good approximation, we have $\Gamma_{h \rightarrow q\bar{q}}(\bar{\kappa}_q = 1) \approx (y_b^{\text{SM}})^2 N_c m_h / 16\pi$. Note that the right hand side is a constant, so we expect the branching ratios for up and down quarks to be the same in the bottom quark scaled formalism when $\bar{\kappa}_u = \bar{\kappa}_d = 1$.

Returning to the task at hand, combining Eq. (29) with Eq. (23) gives the rate in terms of the coupling constants. We would like to constrain this rate with the requirement that it should be equal to the Standard Model rate. In the Standard Model, we have that $\bar{\kappa}_u = \bar{\kappa}_d \approx 0$ and $\kappa_g = 1$, hence we can write

$$R_{\text{SM}}(pp \rightarrow h \rightarrow 4\ell) = \frac{\sigma_{gg}\Gamma(h \rightarrow 4\ell)}{\Gamma_{gg} + \Gamma_{\text{else}}}. \quad (33)$$

Setting $R(\kappa_g, \bar{\kappa}_q) = R_{\text{SM}}$ allows us to write the Standard Model constraint. Before doing this, we note that in order to take detector acceptance into account, these cross sections need to be corrected with multiplicative factors - the efficiencies ϵ_i . We are doing this because we expect the efficiencies for gluon and quark fusion to be different; see Section 4.1. The efficiency for

gluon fusion can be written as

$$\epsilon_g = \frac{\sigma(gg \rightarrow h \rightarrow 4\ell)}{\sigma(gg \rightarrow h)\text{BR}(h \rightarrow 4\ell)}, \quad (34)$$

and the quark fusion efficiencies are defined similarly. The numerator in Eq. (34) is the full process which includes cuts on the four leptons' rapidities and transverse momenta; see Section 4.4. Of course, if the detector is perfect and isotropic, then $\epsilon_i = 1$. In summary, we substitute Eq. (23) and Eq. (29) into Eq. (18) and set the result equal to Eq. (33) to obtain a relationship for the κ couplings which must be satisfied in the Standard Model. We then “correct” the result by inserting the ϵ from Eq. (34) to obtain

$$\kappa_g^2 + \alpha_u \bar{\kappa}_u^2 + \alpha_d \bar{\kappa}_d^2 + \beta_u \kappa_g \bar{\kappa}_u + \beta_d \kappa_g \bar{\kappa}_d = 1, \quad (35)$$

where

$$\alpha_q = \frac{\epsilon_q \bar{\sigma}_{q\bar{q}}(\Gamma_{gg} + \Gamma_{\text{else}}) - \epsilon_g \sigma_{gg} \bar{\Gamma}_{q\bar{q}}}{\epsilon_g \sigma_{gg} \Gamma_{\text{else}}}, \quad (36)$$

$$\beta_q = \frac{\epsilon_{\text{int}}^q \bar{\sigma}_{\text{int}}^q (\Gamma_{gg} + \Gamma_{\text{else}})}{\epsilon_g \sigma_{gg} \Gamma_{\text{else}}}, \quad (37)$$

and $q = u$ or d . As long as $\bar{\sigma}_{\text{int}}^q$ is not too large, Eq. (35) defines an ellipsoid

for the allowed values of the couplings. This in itself can be used to put constraints on $\bar{\kappa}_u$ and $\bar{\kappa}_d$ [28].

4.3 MadGraph Simulations

In order to simulate Higgs events, we use MadGraph5_aMC@NLO 2.2.3 [54]. MadGraph automatically generates matrix elements for a process in terms of initial, final (and possibly intermediate) particles specified by the user. To calculate a given process, it makes a list of subprocesses and calculates the matrix element for each. In order to calculate the cross section, one needs to perform the standard phase space integral over these matrix elements. MadGraph solves this problem by dividing the integration into pieces based on the diagrams and using Monte Carlo integration algorithms to evaluate the contributions independent of the dimensionality. Each Monte Carlo event in the integrator is generated randomly with a statistical weight in terms of the matrix element for that process. These events can not be used directly as kinematic data, since natural events are unweighted. In other words, suppose we have a histogram of the differential distribution of the cross section $d\sigma/d\mathcal{O}$ in some observable \mathcal{O} . A given bin may have, say, n_1 events which each contribute a height w_i to $d\sigma/d\mathcal{O}$. The unweighting procedure converts

these n_1 events to N_1 events such that each of the new events has a weight $(1/N_1) \sum_i w_i$. Hence, each event has the same weight which can be rescaled as necessary. These unweighted events are taken to be “the” underlying events that we see in a detector. One quirk of this procedure is that events at NLO may have negative weights since an interference diagram may give a negative contribution.

MadGraph comes parceled with many different models, including the SM. This model explicitly sets the Yukawa couplings of the Higgs to up and down quarks equal to zero. Furthermore, one can not easily generate $gg \rightarrow h$ since this coupling does not exist at tree level in the SM (see Section 4.2.) In order to generate events which contain all the required Higgs interactions, we begin with the NLO Higgs Characterization model [49, 50, 51, 52]. This model allows us to explicitly define the coupling scale factors κ_i for $i = g, u, d$. Note that this implies an effective vertex for Higgs to gluon coupling as in Figure 3.

4.4 Numerical Cross Sections

We use MadGraph to simulate Higgs events at the 13 TeV LHC at leading and next-to-leading order in QCD, with the NLO results matched to the

i	$\bar{\sigma}(ii \rightarrow h)$ (pb)	$\bar{\sigma}(ii \rightarrow h \rightarrow 4\ell)$ (pb)	$\Gamma(h \rightarrow ii)$ (MeV)
g	16.55 ± 0.02	$(1.44 \pm 0.01) \times 10^{-4}$	0.183 ± 0.001
u	13.44 ± 0.02	$(7.06 \pm 0.01) \times 10^{-5}$	4.34 ± 0.01
d	9.48 ± 0.01	$(6.19 \pm 0.01) \times 10^{-5}$	4.34 ± 0.01
			$\Gamma_{\text{else}} = 5.95 \pm 0.01$

Table 1: Cross sections and decay widths at leading order from MadGraph simulations.

parton shower. We use the NNPDF2.3_QED (LHAPDFID = 244600) parton distribution function sets [55] at the appropriate order in perturbation theory. We shower the events using Herwig++ 2.7.1 [57] and cluster jets using the anti- k_T algorithm in FastJet 3.1.3 [59]. To determine the detector acceptance of the four-lepton final state we employ the following cuts at generator level

$$p_{T,\ell} > 10 \text{ GeV}, \quad (38)$$

$$|\eta_\ell| < 2.5. \quad (39)$$

Directly from MadGraph, we can compute the cross sections and branching ratios; the results are shown in Tables 1 and 2. Note that the uncertainties shown in these tables are a result of the error on the internal Monte Carlo integration and not a physical effect. MadGraph 2.2.3 always computes the branching ratios at LO, even when cross sections are being generated at NLO, which is why Table 2 does not have any branching ratios. When simulating

i	$\bar{\sigma}(ii \rightarrow h)$ (pb)	$\bar{\sigma}(ii \rightarrow h \rightarrow 4\ell)$ (pb)
g	37.3 ± 0.3	$(5.25 \pm 0.02) \times 10^{-4}$
u	15.4 ± 0.1	$(1.24 \pm 0.01) \times 10^{-4}$
d	11.2 ± 0.1	$(1.09 \pm 0.03) \times 10^{-4}$
ug (int)	14.5 ± 0.5	$(1.09 \pm 0.02) \times 10^{-4}$
dg (int)	10.6 ± 0.5	$(8.85 \pm 0.02) \times 10^{-5}$

Table 2: Cross sections and decay widths at next-to-leading order from Mad-Graph simulations.

the full process $ii \rightarrow h \rightarrow 4\ell$ (for either quark or gluon fusion) there are a small ($\approx 10\%$) number of events which contain a largely off-shell Higgs. We eliminate this contribution by discarding any events with an invariant mass that differs by more than 1 GeV from m_h . This changes the “raw” cross section σ to a cut cross section σ_{cut} (already taken into account in Tables 1 and 2) given by

$$\sigma_{\text{cut}} = \sigma \left(\frac{\sum w_{\text{on}}}{\sum w_{\text{on}} + \sum w_{\text{off}}} \right), \quad (40)$$

where w_{on} is the weight of an on-shell event, w_{off} is the weight of an off-shell event and the sums range over all events. Note that, at NLO, these weights can be positive or negative. To extract the interference cross sections, for example between gluon fusion and up quark fusion, we define a multiparticle χ^{gu} which contains only gluons and $u\bar{u}$ quarks. We then compute $\sigma(\chi^{gu}\chi^{gu} \rightarrow$

Process	BR
$h \rightarrow ZZ^*$	6.05×10^{-3}
$Z \rightarrow e^+e^-$	3.43×10^{-2}
$Z \rightarrow \mu^+\mu^-$	3.43×10^{-2}
$h \rightarrow 4\ell$	2.85×10^{-5}

Table 3: Simulated branching ratios from MadGraph.

h). In the same manner as Eq. (20) we can write

$$\sigma(\chi^{gu}\chi^{gu} \rightarrow h) = \sigma(gg \rightarrow h) + \bar{\sigma}(u\bar{u} \rightarrow h) + \bar{\sigma}_{\text{int}}^u. \quad (41)$$

The cross sections $\sigma(gg \rightarrow h)$ and $\bar{\sigma}(u\bar{u} \rightarrow h)$ are computed as normal, so we can use Eq. (41) to simply solve for the interference term. This entire method also applies to the case of $\sigma(ii \rightarrow h \rightarrow 4\ell)$ and for the down quark interference term.

To compute the efficiencies, we still need the term $\text{BR}(h \rightarrow 4\ell)$ which is given by

$$\text{BR}(h \rightarrow 4\ell) = \text{BR}(h \rightarrow ZZ^*)[\text{BR}(Z \rightarrow e^+e^-) + \text{BR}(Z \rightarrow \mu^+\mu^-)]^2. \quad (42)$$

All of these terms are quickly obtainable from MadGraph using the automatic computation of widths. Tables 3 and 4 show the numerical results. Note that $\text{BR}(h \rightarrow 4\ell)$ from Table 3 can not directly be substituted into Eq. (34)

i	ϵ_i (LO)	ϵ_i (NLO)
g	0.306	0.204
u	0.184	0.196
d	0.229	0.237
ug (int)	0	0.186
dg (int)	0	0.207

Table 4: Efficiency coefficients for $h \rightarrow 4\ell$ computed using MadGraph for the lepton acceptances in Eqs. (38) and (39).

since this branching ratio applies only to the case where all couplings are turned on. Since to generate (for example) $gg \rightarrow h \rightarrow 4\ell$ at NLO, we need to set $\bar{\kappa}_u = \bar{\kappa}_d = 0$ in that particular simulation, the “true” branching ratio is $\Gamma(h \rightarrow 4\ell)/(\Gamma_{gg} + \Gamma_{\text{else}})$ as opposed to $\Gamma(h \rightarrow 4\ell)/(\Gamma_{gg} + \Gamma_{u\bar{u}} + \Gamma_{d\bar{d}} + \Gamma_{\text{else}})$. These LO branching ratios are used to consistently determine the efficiencies ϵ_i from the MadGraph simulations using Eq. (34).

We can incorporate better precision on the decay partial widths for the total $h \rightarrow 4\ell$ rate constraint in Eq. (35) by using state-of-the-art computations from the LHC Higgs Cross Section Working Group [61]. These include higher order QCD and electroweak corrections to Higgs decay partial widths, which can be quite sizable for Higgs decays to $q\bar{q}$. Using the results in Ref. [61] for $m_h = 125$ GeV, we have $\Gamma_{gg} = 0.349$ MeV, $\bar{\Gamma}_{u\bar{u}} = \bar{\Gamma}_{d\bar{d}} = 2.35$ MeV and $\Gamma_{\text{else}} = 3.72$ MeV. Note that we are taking $\bar{\Gamma}_{u\bar{u}} = \bar{\Gamma}_{d\bar{d}} = \Gamma_{b\bar{b}}^{\text{SM}}$; the error from neglecting the finite bottom quark kinematic mass is at the percent

	LO	NLO
α_u	-0.226 ± 0.001	-0.321 ± 0.001
α_d	-0.287 ± 0.001	-0.369 ± 0.001
β_u	0	0.365 ± 0.001
β_d	0	0.297 ± 0.001

Table 5: Numerical constraint coefficients computed using MadGraph simulated data with LO decay partial widths.

	LO	NLO
α_u	-0.098 ± 0.001	-0.197 ± 0.001
α_d	-0.162 ± 0.001	-0.250 ± 0.001
β_u	0	0.387 ± 0.001
β_d	0	0.315 ± 0.001

Table 6: Numerical constraint coefficients computed using partial widths extracted from Ref. [61] (see text for details.)

level. Numerical results are given in Tables 5 and 6. The difference between Tables 5 and 6 is simply whether we use partial widths computed from MadGraph (Table 1) or high-precision partial widths from Ref. [61] in Eqs. (36) and (37). For the actual analysis we will use the data from the high-precision widths, i.e. Table 6.

5 Constraints From Simulated Kinematic Data

I know too well that these arguments from probabilities are impostors, and unless great caution is observed in the use of them, they are apt to be deceptive.

Plato, *Phaedo*

5.1 The Asymmetry Parameter

From interaction simulations, in addition to the total cross section of the process, we also obtain kinematic information. In other words, we have access to the four-momenta of outgoing particles. The *shape* of the distribution of the transverse momentum $p_T = \sqrt{p_x^2 + p_y^2}$ and the z momentum p_z of the Higgs can be used to construct an observable quantity that can put independent constraints on couplings. Figures 6 and 7 show these momentum distributions for our $gg \rightarrow h \rightarrow 4\ell$, $u\bar{u} \rightarrow h \rightarrow 4\ell$ and $d\bar{d} \rightarrow h \rightarrow 4\ell$ processes.

We define the asymmetry parameter of a kinematic distribution as

$$A_{i,j} = \frac{N(p_{i,j} > p_{i,j}^{\text{cut}}) - N(p_{i,j} < p_{i,j}^{\text{cut}})}{N(p_{i,j} > p_{i,j}^{\text{cut}}) + N(p_{i,j} < p_{i,j}^{\text{cut}})}, \quad (43)$$

where $i = z, T$ and $j = g, u, d$ and $p_{i,j}^{\text{cut}}$ is some critical momentum value around which the asymmetry parameter is calculated. The quantity $N(p_{i,j} > p_{i,j}^{\text{cut}})$ is how many events of fusion type j have momentum type i greater than

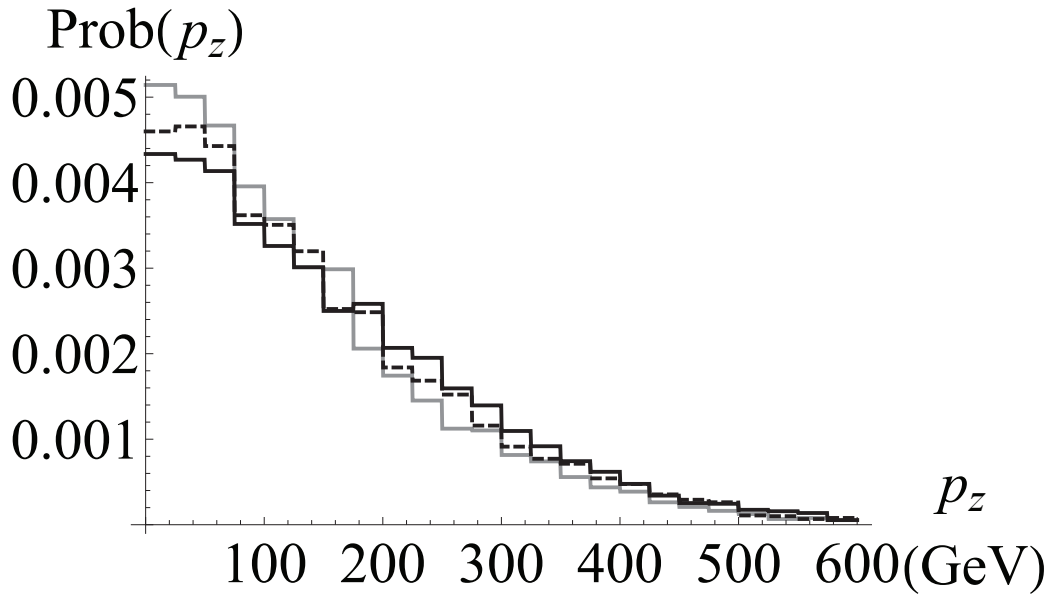
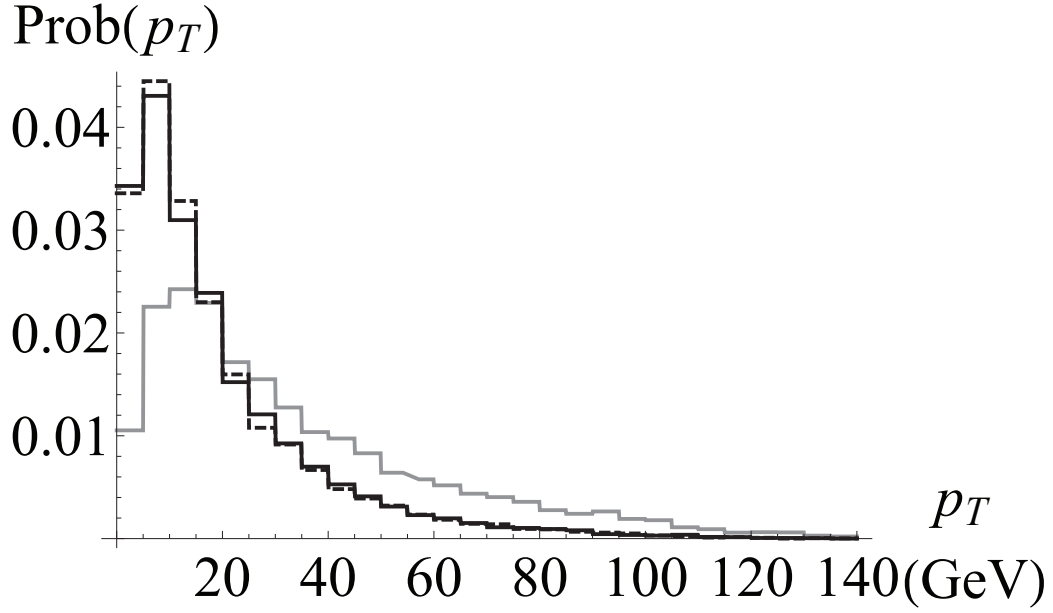


Figure 6: Sample momentum distributions (p_T and p_z) for $xx \rightarrow h \rightarrow 4\ell$, $x = g, u, d$ at leading order from 10,000 generated events. Gray is for gluons, solid black is for up quarks and dashed black is for down quarks.

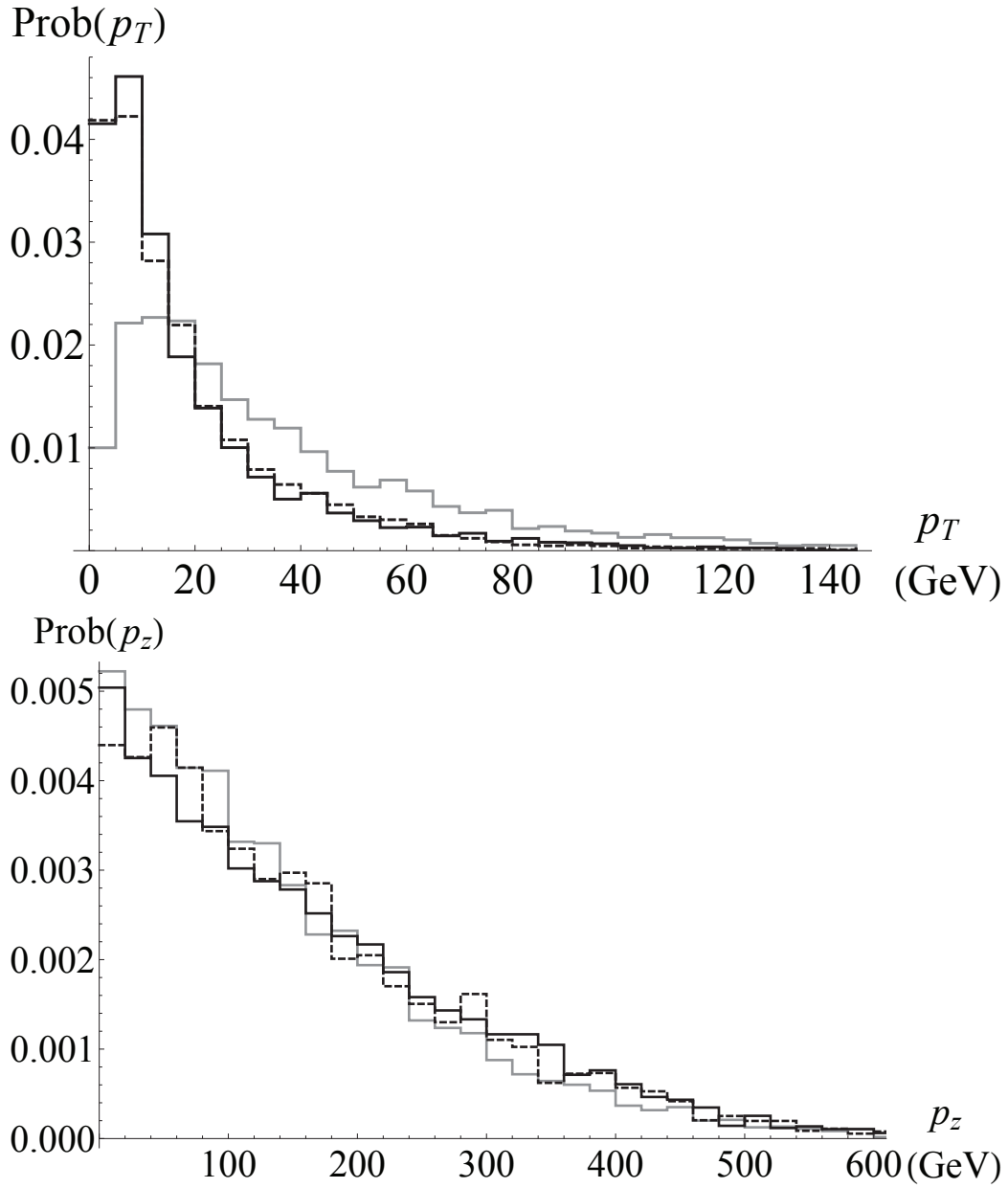


Figure 7: The same as Fig. 6 but at next-to-leading order.

$p_{i,j}^{\text{cut}}$ and similarly for $N(p_{i,j} < p_{i,j}^{\text{cut}})$. Using $N_{\text{tot}} = N(p_{i,j} > p_{i,j}^{\text{cut}}) + N(p_{i,j} < p_{i,j}^{\text{cut}})$, we can write

$$A_{i,j} = 1 - 2 \frac{N(p_{i,j} < p_{i,j}^{\text{cut}})}{N_{\text{tot}}}. \quad (44)$$

Given a measurement of $A_{i,j}$, the statistical uncertainty is given by

$$\sigma_{A_{i,j}}^{\text{stat.}} = \sqrt{\frac{1 - A_{i,j}^2}{N_{\text{tot}}}}; \quad (45)$$

see Appendix A for a derivation. When we make an experimental measurement of the asymmetry parameter, it is not known *a priori* which processes made which contributions to the momentum distributions. Hence, the measured asymmetry parameter will be a linear combination of the asymmetry parameter for each of the contributing processes, weighted by the rate for that process. Since the branching ratios are all the same for each production process, we can write

$$A = \frac{A_{gg} \kappa_g^2 \epsilon_g \sigma_{gg} + \sum_{q=u,d} A_{q\bar{q}} \bar{\kappa}_q^2 \epsilon_q \bar{\sigma}_{q\bar{q}} + \sum_{q=u,d} A_{\text{int}}^q \kappa_g \bar{\kappa}_q \epsilon_{\text{int}}^q \bar{\sigma}_{\text{int}}^q}{\kappa_g^2 \epsilon_g \sigma_{gg} + \sum_{q=u,d} \bar{\kappa}_q^2 \epsilon_q \bar{\sigma}_{q\bar{q}} + \sum_{q=u,d} \kappa_g \bar{\kappa}_q \epsilon_{\text{int}}^q \bar{\sigma}_{\text{int}}^q}. \quad (46)$$

We can eliminate κ_g from Eq. (46) by imposing the requirement that the total Higgs event rate to 4ℓ is exactly consistent with the SM prediction, Eq.

(35), as observed at the LHC. Hence, we can analytically write $A(\bar{\kappa}_u, \bar{\kappa}_d)$ which already takes care of the gluon coupling in a consistent way.

To illustrate how this procedure will work, let us first consider the LO case. Supposing that we have a method of choosing $p_{i,j}^{\text{cut}}$ (see Section 5.2) and given an experiment which provides kinematic data of the form shown in Figures 6 and 7, we can compute A_{gg} and A_{qq} for $q = u, d$. Since the cross sections and efficiencies are known, we can assume that the total asymmetry parameter will be equal to its SM expectation (i.e. A_{gg} plus its statistical error) and thereby obtain a constraint contour for $\bar{\kappa}_u$ and $\bar{\kappa}_d$. If the gluon fusion and quark fusion distributions are very similar, or if $p_{i,j}^{\text{cut}}$ is not well chosen, then $A_{gg} \approx A_{qq}$ and Eq. (46) is reduced to the meaningless statement that $A_{gg} \approx A_{gg}$. Therefore, we would like to maximize the difference between A_{gg} and A_{qq} . We will see shortly that this is sufficient at LO, but the presence of interference terms at NLO means that maximizing the difference between A_{gg} and A_{qq} will not necessarily lead to the tightest constraints on the couplings.

5.2 Optimization of p_{cut}

In order to actually use the asymmetry value, a suitable $p_{i,j}^{\text{cut}}$ must be chosen before the fact. At leading order, we would like the difference between the quark and gluon asymmetries to be as large as possible in order to maximize the resolving power between the processes. If $f_{i,j}(p_{i,j})$ is the underlying physical distribution of $p_{i,j}$, then Eq. (44) can be written as

$$A_{i,j} = 1 - 2 \int_0^{p_{i,j}^{\text{cut}}} f_{i,j}(p_{i,j}) dp_{i,j}. \quad (47)$$

We would like to choose $p_{i,q}^{\text{cut}}$ so that $\Delta A_{i,q} = A_{i,g} - A_{i,q}$ for $q = u, d$ is as large as possible in order to maximize the resolving power between gluon and quark fusion distributions. Note that every distribution in principle has its own cut $p_{i,j}^{\text{cut}}$, but for a given set of data (i.e. transverse or longitudinal momentum distributions) we have to use the same cut on all fusion distributions. The implication is that we can not necessarily maximize $\Delta A_{i,q}$ for both up and down quarks simultaneously. In any case, for a given quark distribution, we want to maximize

$$\Delta A_{i,q} = 2 \left(\int_0^{p_i^{\text{cut}}} f_{i,g}(p_{i,g}) dp_{i,g} - \int_0^{p_i^{\text{cut}}} f_{i,q}(p_{i,q}) dp_{i,q} \right). \quad (48)$$

By differentiating with respect to p_i^{cut} , we see the optimal choice is the value such that $f_{i,g}(p_i^{\text{cut}}) = f_{i,q}(p_i^{\text{cut}})$. Of course there is no guarantee that either of the p_i^{cut} will be equal. At next-to-leading order, the situation is more complicated due to the interference terms. Clearly we would like the resolving power to be as good as possible, which translates into the requirement that whatever p_i^{cut} may be, the area of the constraint contours from Eq. (46) should be minimized. We also note that p^{cut} can in principle be an arbitrary function in the two-dimensional parameter space (p_T, p_z) ; we could for example write $p_T^{\text{cut}}(p_z) = ap_z + b$ and find the best choice of a and b as opposed to treating p_z and p_T separately. Physically this means drawing an arbitrary line through a two-dimensional histogram of p_T vs. p_z and setting $N(p < p_{i,j}^{\text{cut}})$ from Eq. (44) equal to the number of points below the line. Since the p_z and p_T distributions are independent, we could hope to increase the significance of the constraints by combining the measurements in this way. However, by examining Figures 6 and 7, we can see that there is almost no resolving power between gluons and quarks from p_z ; the distributions are nearly identical. The cut on the leptons' rapidities in Eq. (39) has the effect of removing the long tail of the Higgs p_z distribution for quark fusion. This tail, shown in Figure 8, is completely expected as we discussed in Section 4.1

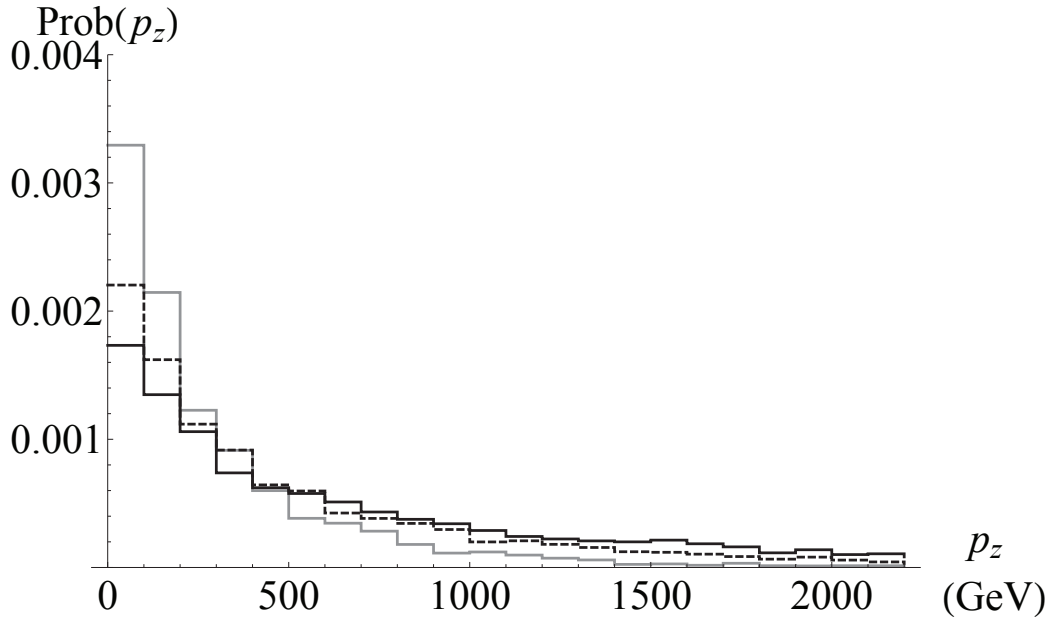


Figure 8: The same as Fig. 7 but without the lepton rapidity cut in Eq. (39).

and without it we lose the most important feature for distinguishing quark fusion from gluon fusion. We are therefore forced to conclude that treating p_z and p_T simultaneously is not significantly better than exclusively considering p_T ; hence we ignore p_z .

To find the optimal cut at next-to-leading order we use a heuristic procedure. By computing all the asymmetries beforehand on a grid of trial p_T^{cut} values, we can plot the constraint ellipses for each cut and select the smallest one. Using this procedure we find that $p_T^{\text{cut}} = 18 \pm 1$ GeV at leading order and $p_T^{\text{cut}} = 20 \pm 1$ GeV at next-to-leading order. The fact that the optimal cut

i	$A_T^{\text{LO}}(p_T^{\text{cut}} = 18 \text{ GeV})$	$A_T^{\text{NLO}}(p_T^{\text{cut}} = 20 \text{ GeV})$
g	0.29 ± 0.01	0.27 ± 0.01
u	-0.24 ± 0.01	-0.35 ± 0.01
d	-0.26 ± 0.01	-0.32 ± 0.01
ug (int)	0	0.070 ± 0.001
dg (int)	0	-0.014 ± 0.001

Table 7: Asymmetry parameters for each production process calculated using optimized cuts at LO and NLO.

is close to 20 GeV in either case is useful and easy to remember. It also gives some confidence that the NLO corrections do not overwhelmingly change the picture. Using these cuts we find the results in Table 7. To extract the “pure” asymmetries A_{qq} and A_{gg} , we simply examine the kinematic distributions of $ii \rightarrow h \rightarrow 4\ell$ for $ii = gg, u\bar{u}$ and $d\bar{d}$. We need to do a bit more work to obtain the interference asymmetry parameters A_{int}^q . To do this, we use the trick discussed in Section 4.4 where we define a multiparticle which contains only gluons and $u\bar{u}$ quarks. The kinematic distribution from this process is the sum of the distributions of the individual processes. The total asymmetry $A_{u\bar{u}g}$ will then be the weighted sum of individual asymmetries as

$$A_{u\bar{u}g} = \frac{A_{gg}\epsilon_g\sigma_{gg} + A_{u\bar{u}}\epsilon_u\bar{\sigma}_{u\bar{u}} + A_{\text{int}}^u\epsilon_{\text{int}}^u\bar{\sigma}_{\text{int}}^u}{\epsilon_g\sigma_{gg} + \epsilon_u\bar{\sigma}_{u\bar{u}} + \epsilon_{\text{int}}^u\bar{\sigma}_{\text{int}}^u}. \quad (49)$$

This is enough to determine A_{int}^u , since every other term is known. Note that

this is essentially Eq. (46) with $\bar{\kappa}_d = 0$. To extract A_{int}^d we replace u with d in Eq. (49) and follow the same procedure.

5.3 Constraints From the Asymmetry Parameter

Suppose that we make a measurement of A that is consistent with the SM, i.e. $A_T^{\text{LO}} = A_{g,T}^{\text{LO}} = 0.29$ and $A_T^{\text{NLO}} = A_{g,T}^{\text{NLO}} = 0.27$. The error on this value puts constraints on the couplings and, since σ_A only depends on A and N , we need to estimate the number of observed events. This is given by

$$N_{\text{exp}} = \epsilon_{gg} \sigma(gg \rightarrow h) \text{BR}^{\text{SM}}(h \rightarrow 4\ell) \int \mathcal{L} dt, \quad (50)$$

where $\int \mathcal{L} dt$ is the integrated luminosity and $\text{BR}^{\text{SM}}(h \rightarrow 4\ell) = 1.26 \times 10^{-4}$ from Ref. [61]. Table 8 shows the expected number of events and statistical error on the asymmetry for various integrated luminosities. The LHC will achieve an integrated luminosity of 30 fb^{-1} in 2016 and should achieve 300 fb^{-1} by 2021. After the High-Luminosity Phase II upgrade, it may reach 3000 fb^{-1} by 2030. Now, we can substitute Eq. (35) with the values in Table 6 into Eq. (46) and use our numerical results for the cross sections (Tables

$\int \mathcal{L} dt \text{ (fb}^{-1}\text{)}$	$N_{\text{exp}} \text{ (LO)}$	$\sigma_A \text{ (LO)}$	$N_{\text{exp}} \text{ (NLO)}$	$\sigma_A \text{ (NLO)}$
30	20	0.22	30	0.18
300	200	0.071	300	0.056
3000	2000	0.022	3000	0.018

Table 8: Expected number of observed events for gluon-initiated Higgs decay to four leptons. The error on the asymmetry is σ_A .

1 and 2), efficiencies (Table 4) and asymmetries (Table 7) to write

$$A_T^{\text{LO}}(\bar{\kappa}_u, \bar{\kappa}_d) = \frac{0.29 - 0.089\bar{\kappa}_u^2 - 0.064\bar{\kappa}_d^2}{1.0 + 0.59(\bar{\kappa}_u^2 + \bar{\kappa}_d^2)}. \quad (51)$$

At next-to-leading order, the functional form is considerably more complicated; we have

$$\kappa_g = -0.19\bar{\kappa}_u - 0.16\bar{\kappa}_d \pm \sqrt{1.0 + 0.23\bar{\kappa}_u^2 + 0.27\bar{\kappa}_d^2 + 0.061\bar{\kappa}_u\bar{\kappa}_d}, \quad (52)$$

$$A_T^{\text{NLO}}(\bar{\kappa}_u, \bar{\kappa}_d) = \frac{0.27\kappa_g^2 - 0.14\bar{\kappa}_u^2 - 0.11\bar{\kappa}_d^2 + 0.025\bar{\kappa}_u\kappa_g - 0.0040\bar{\kappa}_d\kappa_g}{1.0\kappa_g^2 + 0.40\bar{\kappa}_u^2 + 0.35\bar{\kappa}_d^2 + 0.35\bar{\kappa}_u\kappa_g + 0.29\bar{\kappa}_d\kappa_g}. \quad (53)$$

Unlike the LO asymmetry, the NLO asymmetry contains terms which depend on κ_g as well as κ_g^2 , so we have to take a stand on the plus-or-minus sign in Eq. (52). We choose the plus sign to ensure that κ_g is positive. Finally, to create limits on $\bar{\kappa}_u$ and $\bar{\kappa}_d$ at a 95% confidence level, we set the asymmetry

300 fb^{-1}	3000 fb^{-1}
$-1.3 \lesssim \bar{\kappa}_u \lesssim 0.67$	$-0.73 \lesssim \bar{\kappa}_u \lesssim 0.33$
$-1.6 \lesssim \bar{\kappa}_d \lesssim 0.69$	$-0.88 \lesssim \bar{\kappa}_d \lesssim 0.32$

Table 9: Constraints on the couplings from the NLO contours of Figure 9.

parameters in Eqs. (51) and (53) equal to their SM expectations (i.e. the gluon fusion asymmetry) with the expected statistical uncertainty of $2\sigma_A$. In other words, we have the implicit equations $A_T^{\text{LO}}(\bar{\kappa}_u, \bar{\kappa}_d) = A_{g,T}^{\text{LO}} \pm 2\sigma_A$ and $A_T^{\text{NLO}}(\bar{\kappa}_u, \bar{\kappa}_d) = A_{g,T}^{\text{NLO}} \pm 2\sigma_A$, where the error σ_A depends on the integrated luminosity and is given in Table 8. Figure 9 shows the 95% confidence limits on the scaled up and down quark couplings. These limits are given numerically in Table 9.

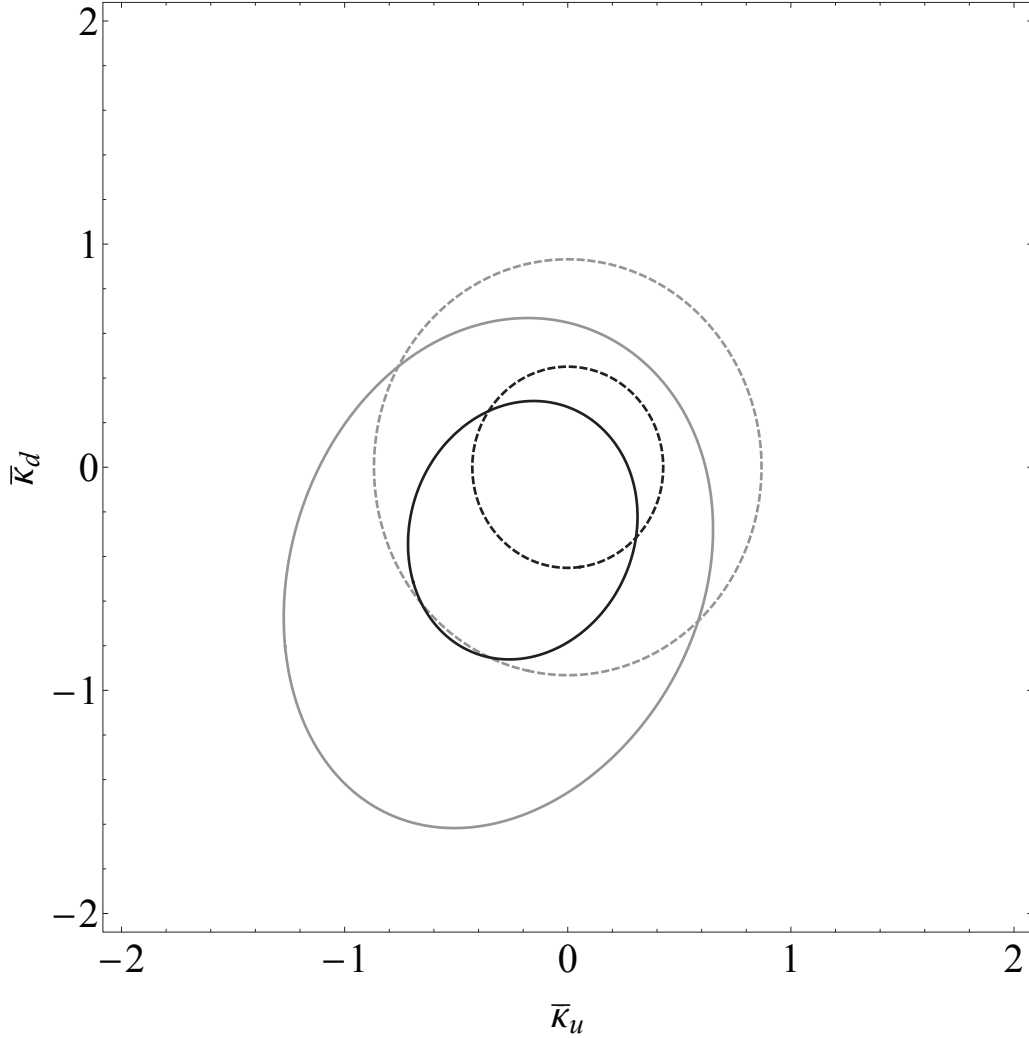


Figure 9: Coupling constraints from p_T at leading order (dashed) and next-to-leading order (solid) at 300 fb^{-1} (gray) and 3000 fb^{-1} (black) obtained from requiring that A_T be within $\pm 2\sigma_A$ (Table 8) of the SM prediction - pure gluon fusion. Note that the case of 30 fb^{-1} is not good enough to put any constraints on the couplings, as is the case of A_z .

6 Discussion and Conclusions to Part 1

To understand this for sense it is not required that a man should be a geometrician or a logician, but that he should be mad.

Thomas Hobbes, quoted in *Mathematical Maxims and Minims*

To get a feel for the results in Section 5.3, we will compute the contribution to the Higgs total width and production cross section for our best limits at 3000 fb^{-1} . From Table 9, we see that the tightest constraints obtainable by this method are $\bar{\kappa}_u < 0.33$ and $\bar{\kappa}_d < 0.32$. The following conclusions are all summarized numerically in Table 10. Let us begin by considering the effect of the new light quark couplings on the Higgs width. In the SM, $\Gamma_{\text{tot}} = 4.08 \text{ MeV}$. For $\bar{\kappa}_u = 0.33$ and $\bar{\kappa}_d = 0$, we have $\Gamma_{u\bar{u}} = 0.256 \text{ MeV}$ and for $\bar{\kappa}_u = 0$ and $\bar{\kappa}_d = 0.32$ we have $\Gamma_{d\bar{d}} = 0.241 \text{ MeV}$. We conclude that the enhanced couplings each constitute an increase in the Higgs total width by about 6 percent. This is comparable to the SM $h \rightarrow \tau^+\tau^-$ branching ratio of ≈ 0.063 . Now let us consider the Higgs production cross section. In the SM, we have $\sigma(gg \rightarrow h) = 43.92 \text{ pb}$ from Ref. [61]. For $\bar{\kappa}_u = 0.33$ and $\bar{\kappa}_d = 0$, we compute $\kappa_g = 0.949$ which gives $\sigma(gg \rightarrow h) = 39.55 \text{ pb}$, $\sigma(u\bar{u} \rightarrow h) = 1.68 \text{ pb}$ and $\sigma_{\text{int}}(ug \rightarrow h) = 5.14 \text{ pb}$. For $\bar{\kappa}_u = 0$ and $\bar{\kappa}_d = 0.32$ we compute $\kappa_g = 0.963$ which gives $\sigma(gg \rightarrow h) = 40.73 \text{ pb}$, $\sigma(d\bar{d} \rightarrow h) = 1.15 \text{ pb}$ and $\sigma_{\text{int}}(dg \rightarrow h) = 3.27 \text{ pb}$. We conclude that each of the pure quark fusion

$(\bar{\kappa}_u, \bar{\kappa}_d)$	$\Gamma(h \rightarrow q\bar{q})$ (MeV)	$\sigma(q\bar{q} \rightarrow h)$ (pb)	$\sigma_{\text{int}}(q\bar{q} \rightarrow h)$ (pb)
(0.33, 0)	0.256 [6.2%]	1.68 [3.8%]	5.14 [12%]
(0, 0.32)	0.241 [5.9%]	1.15 [2.6%]	3.27 [7.4%]

Table 10: The effect of enhanced light quark Yukawa couplings equal to the tightest constraints (at 3000 fb^{-1} ; see Figure 9 and Table 9) obtained from the asymmetry parameter analysis. The quantities in square brackets are the percentage increases in the SM Higgs total width or SM gluon-initiated Higgs production cross section assuming the couplings given in the first column.

processes would enhance the gluon-initiated Higgs production cross section by about 3 percent, comparable to the Wh associated Higgs production contribution of 1.38 pb in the SM. The quark fusion interference cross sections are more significant; each gives about 10 percent. This is comparable to the SM vector boson fusion cross section of 3.75 pb.

We note that the SM expectations of the couplings are $\bar{\kappa}_u^{\text{SM}} = m_u/m_b \approx 5.5 \times 10^{-4}$ and $\bar{\kappa}_d^{\text{SM}} = m_d/m_b \approx 1.2 \times 10^{-3}$. Hence, if this method performs exactly as advertised, it will not be able to exclude the SM prediction. As it stands, due to the lack of statistics, we can only exclude models with hugely enhanced light quark couplings. One way to improve the prospects is to use the fact that the constraints from our method are independent of the constraints from the global signal rate. Ref. [28] gives, for example, $\bar{\kappa}_u \lesssim 1.1$ with 20 fb^{-1} . With 3000 fb^{-1} , they have access to roughly 100 times more events. This corresponds to a decrease by a factor of 10 in the

error, assuming that it is dominated by statistics. But then, the rate is proportional to the square of the coupling, so the upshot is that we expect that the rate constraint $\bar{\kappa}_u \lesssim 1.1$ will be decreased by around $\sqrt{10}$ with 3000 fb^{-1} integrated luminosity. This leads to $\bar{\kappa}_u^{\text{rate}} \lesssim 0.35$ as a fair estimate for the constraining power of the rate method. We compute the combined constraint via

$$\delta\bar{\kappa}_u^{\text{comb.}} = \frac{(\delta\bar{\kappa}_u^A)(\delta\bar{\kappa}_u^{\text{rate}})}{\sqrt{(\delta\bar{\kappa}_u^A)^2 + (\delta\bar{\kappa}_u^{\text{rate}})^2}}, \quad (54)$$

where $\delta\bar{\kappa}_u^A = 0.33$ is the constraint from the asymmetry method and $\delta\bar{\kappa}_u^{\text{rate}} = 0.35$ is the constraint from the rate. Eq. (54) gives $\delta\bar{\kappa}_u^{\text{comb.}} = 0.24$; a similar calculation gives $\delta\bar{\kappa}_d^{\text{comb.}} = 0.26$.

One way to improve the asymmetry method is to make use of final states other than the 4ℓ channel considered here. The most promising choice is the diphoton channel mentioned in Section 4.2. This channel has more statistics (Ref. [61] gives $\text{BR}(h \rightarrow \gamma\gamma) \approx 2.27 \times 10^{-3}$, approximately 17 times higher than the 4ℓ branching ratio) at the expense of a higher background. It's true that the shapes of the Higgs p_T and p_z distributions are controlled by initial state radiation and the proton PDF respectively and, if these were the only contributing factors, the diphoton asymmetries should be very similar to the

4ℓ asymmetries. However, we note that the difference between Figures 7 and 8 implies that the lepton acceptance cuts have a significant effect on the shape of the momentum distributions. In particular, we can reasonably expect that the efficiencies will be different between the two channels since the cuts are different, and since we're only looking for two particles as opposed to four. This gives another independent constraint and could plausibly contribute another factor of at least $1/\sqrt{2}$ to the coupling, depending on how much of an overlap there is between the two constraint ellipses (of the form in Figure 9).

An issue we have glossed over is the effect of systematic uncertainties on the results. These will strictly weaken the constraints, but it is beyond the scope of this work to calculate the exact contribution. We note that with 3000 fb^{-1} , the statistical uncertainty on the asymmetry in the 4ℓ channel is 7%; this sets the scale for whether systematic uncertainties will have a significant effect on our results.

In conclusion, we have presented a method for constraining the up and down quark Yukawa couplings at a level comparable to competing approaches. Since our method is independent, it can be combined with limits from the Higgs signal strength to further increase the precision. We find that 3000 fb^{-1}

of integrated luminosity can lead to $\bar{\kappa}_u \lesssim 0.33$ and $\bar{\kappa}_d \lesssim 0.32$ in the best case.

Future analyses can consider the diphoton final state in addition to the four-lepton final state to decrease the statistical error.

7 Introduction to Part 2

And now for something completely different ...

Monty Python, *Monty Python's Flying Circus*

Newtonian gravity predicts that the rotational velocity of luminous objects like stars and gas clouds should decrease as they get farther away from the center of a galaxy. Astronomical and cosmological observations instead show that the rotational velocity profile tends to become roughly constant. One explanation is that there must be some extra matter permeating the galaxy contributing enough mass to cancel out the expected decrease. Since this extra matter must be massive, and since it must interact very weakly with electromagnetic radiation (otherwise it would be luminous matter, by definition) we call it Dark Matter (DM). There are several possible DM candidates (see Ref. [23] for a detailed review) but the top contenders are weakly interacting massive particles (WIMPs). One reason that the WIMP paradigm is useful is that the present relic density (the amount of dark matter left over since the early Universe) can be calculated assuming that the WIMPs were in thermal and chemical equilibrium with the rest of the SM in the early Universe. Comparison of this calculation with the measured value allows us to infer some useful physical properties of the WIMPs.

To understand this, we introduce the mechanism of freeze-out. In the early Universe, as long as the WIMPs are non-relativistic (in other words, as long as their thermal energy is less than their rest energy) their number density is exponentially suppressed by Boltzmann statistics. As the Universe evolves, it expands and cools, so the WIMP number density in a comoving volume is a decreasing function of time. During this era, WIMPs are common enough to self-annihilate regularly. However, eventually the expansion rate of the Universe becomes so large that WIMPs become too rare to ever meet each other (so, their annihilation rate becomes small) and their number density approaches a constant value. The transition from an exponentially decaying number density to a constant one is what we mean when we say “freeze-out.” This gives us a clue as to how we can predict at least two properties of the WIMP. The exact point at which the number density becomes constant must depend on both the self-annihilation cross section and mass of the dark matter. The constant number density persists until the present day and is directly related to the aforementioned relic density. Hence, given a measurement of this quantity, we can calculate the required dark matter self-annihilation cross section as a function of the dark matter mass needed to reproduce the observed result.

The exact form of the self-annihilation cross section depends on the particular dark matter model. Models with scalar dark matter have s-wave annihilation in which the product of the cross section and the relative velocity of the dark matter particles is independent of velocity, i.e. $\sigma v_{\text{rel}} = \text{constant}$. This is the simplest case and the results of the relic density calculation are well-known. In particular, the details are outlined in Ref. [67] - this paper is very useful as a quick reference for model-building. Our work is a spiritual successor of sorts, extending to p-wave and resonant annihilation mechanisms. P-wave annihilation generally arises in models which contain fermionic dark matter. Here, the product of the cross section and the relative velocity of the dark matter particles is proportional to the square of the relative velocity, i.e. $\sigma v_{\text{rel}} \propto v_{\text{rel}}^2$. The relic density calculation determines the observationally required proportionality constant as a function of the dark matter mass. We also consider models which contain dark matter annihilation through a scalar mediator. This is referred to as resonant annihilation since the cross section increases by several orders of magnitude when the dark matter's mass is approximately half of the mediator's mass. For concreteness, we take the scalar mediator to be a particle with mass and width equal to the SM Higgs boson mass and width. The relic density calculation

determines the overall proportionality constant (the exact functional form is fairly complicated) as a function of the dark matter mass.

The calculation we have been alluding to involves the integration of a stiff ordinary differential equation (ODE) over a large range. This is a difficult numerical problem that evades a solution via standard Runge-Kutta algorithms. Ref. [81] introduced a general numerical method for integrating ODEs of the form that we are interested in. This method is called the “Möbius” method and, to the best of our knowledge, it has not been previously applied to dark matter freeze-out. We find that the Möbius method is fast, accurate and very easy to implement in practice - requiring no complicated transformations or other manipulations from the user.

The outline of Part 2 of the thesis is as follows. In Section 8 we explain how the freeze-out process leads to thermal WIMP relics that we observe today. In terms of the WIMP mass and annihilation cross section, we state the canonical differential equation to be solved in order to determine the present relic abundance. We introduce a parameterization for the number of effective relativistic SM degrees of freedom $g(T)$ and compare it to the state-of-the-art calculation. We consider the cases of s-wave, p-wave and resonant annihilation in turn. In Section 9 we outline the Möbius scheme and compare

it with explicit Runge-Kutta methods as applied to this problem. We discuss a short analytic argument based on a far-field approximation which allows us to reduce the computational effort of the integration by a factor of 10. In Section 10, we apply these methods to the integration of the relic density to reproduce the standard plot (as in Figure 5 of Ref. [67]) of the required WIMP annihilation cross section as a function of mass for s-wave annihilation, and produce analogous plots for p-wave and resonant annihilation. In Section 11, we summarize our conclusions and outline possible future work. There are two appendices that are relevant to Part 2. Appendix C contains a series of fitting functions for $g(T)$ and its derivatives. Appendix D contains a derivation of the thermally averaged cross section for resonant annihilation.

8 Theoretical Foundations of Dark Matter Freeze-

Out

If someone points out to you that your pet theory of the universe is in disagreement with Maxwell's equations - then so much the worse for Maxwell's equations. If it is found to be contradicted by observation - well, these experimentalists do bungle things sometimes. But if your theory is found to be against the second law of thermodynamics I can give you no hope; there is nothing for it but to collapse in deepest humiliation.

Sir Arthur Eddington, *The Running-Down of the Universe*

We begin by reviewing the physical basis for standard freeze-out calculations. The information in this chapter follows primarily Ref. [62]. See also Refs. [63, 64, 65].

8.1 Introduction to Freeze-Out

Consider a Majorana WIMP χ of mass m and spin $1/2$; hence it has $g_\chi = 2$ internal degrees of freedom. The number density $n(t)$ of χ is given by the Boltzmann equation. As the Universe expands, the number of particles per unit volume decreases by definition. The expansion rate of the Universe is characterized by the Hubble parameter $H = a^{-1}(da/dt)$, where $a(t)$ is the scale factor in the Robertson-Walker metric. Therefore, in the absence of self-annihilation, we expect something like $dn/dt \propto -Hn$. On the other hand, given a finite self-annihilation cross section σ , two χ particles with

relative velocity v_{rel} will annihilate at a rate proportional to $\sigma \times (nv_{\text{rel}}) \times n$. Since the annihilation can take place at any temperature, weighted by the relevant thermal distribution, we take the annihilation rate to be equal to $-\langle\sigma v_{\text{rel}}\rangle_T n^2$. The quantity $\langle\sigma v_{\text{rel}}\rangle_T$ is the thermally weighted average of σv_{rel} . If the particles are non-relativistic, the thermal average is taken over the Maxwell-Boltzmann distribution. We will drop the subscript T and simply write $\langle\sigma v_{\text{rel}}\rangle$ and call it the thermally weighted cross section, or just “the” cross section. Finally, there will be some critical number density n_{eq}^2 such that thermal production and annihilation reach equilibrium, hence we expect something like $dn/dt \propto -\langle\sigma v_{\text{rel}}\rangle(n^2 - n_{\text{eq}}^2)$. The Boltzmann equation takes both of these factors into account via

$$\frac{dn}{dt} = -3Hn - \langle\sigma v_{\text{rel}}\rangle(n^2 - n_{\text{eq}}^2). \quad (55)$$

In the early Universe, the second term (i.e. production/annihilation rates) is much larger than the first term, so $n \approx n_{\text{eq}}$. As the Universe expands, the temperature T goes down, so WIMPs are less likely to be thermally produced and n_{eq} drops exponentially (see Section 8.2). During this time, n continues to track n_{eq} until eventually there aren’t enough WIMPs left to

annihilate and n levels off from the exponential decay of n_{eq} . In the late Universe, the temperature is much too small to produce additional WIMPs and the expansion rate is large enough that WIMPs are too rare to ever meet. Hence, their number in a comoving volume approaches a constant; it is this process that we call freeze-out. The leftover WIMPs define the thermal relic density that we observe today. Given a WIMP mass m_χ and annihilation cross section $\langle\sigma v_{\text{rel}}\rangle$, solving Eq. (55) for large times will tell us the number density of WIMPs at the present date, and hence the dark matter relic density. In other words, the integration of Eq. (55) will tell us whether or not the combination $m_\chi, \langle\sigma v_{\text{rel}}\rangle$ accounts for the observed dark matter relic density. It is this integration that constitutes the main focus of this work.

8.2 The Effective Relativistic Degrees of Freedom

Let us work in units such that $\hbar = c = k = 1$. The Friedmann equations give

$$H = \sqrt{8\pi G_n \rho/3}, \tag{56}$$

where G_n is Newton's gravitational constant and ρ is the energy density. In general, for a species i with g_i internal degrees of freedom with chemical potential $\mu = 0$, we have

$$\rho_i = \frac{g_i}{2\pi^2} \int_{m_i}^{\infty} \frac{\sqrt{E^2 - m_i^2}}{\exp(E/T_i) \pm 1} E^2 dE, \quad (57)$$

where the $+$ sign corresponds to fermions and the $-$ sign corresponds to bosons. Let us define the often-useful parameter $x_i = m_i/T_i$. Making the substitution $u_i = E/T_i = x_i E/m_i$ in Eq. (57) leads to

$$\rho_i = \frac{g_i}{2\pi^2} T_i^4 \int_{x_i}^{\infty} \frac{\sqrt{u_i^2 - x_i^2}}{\exp(u_i) \pm 1} u_i^2 du_i. \quad (58)$$

Then, in terms of the photon temperature T , the total energy density is simply

$$\rho_{\text{tot}} = T^4 \sum_{i=\text{all species}} \left(\frac{T_i}{T}\right)^4 \rho_i, \quad (59)$$

where T_i is the temperature of the species, which in general can be different from the photon temperature. However, for almost all of the history of the Universe, $T_i = T$ and we will henceforth assume that this is true. Now let us consider the contribution of a non-relativistic species to the total energy

density at some temperature T . This species has $m \gg T$, so $x_i \gg 1$. By examining Eq. (58), if x_i is very large, the range of integration only contains contributions from large u , and since there is a factor of $\exp(u)$ in the denominator, ρ_i is exponentially suppressed. One can show that

$$\rho_i(m_i \ll T) = \frac{g_i}{(2\pi)^{3/2}} m_i T^3 x_i^{3/2} e^{-x_i}. \quad (60)$$

A non-relativistic gas of particles acts like pressureless dust, so as long as χ is non-relativistic, we can write $\rho_\chi = m_\chi n_\chi$, where n_χ is the same number density that appears in Eq. (55). Hence, the equilibrium number density for non-relativistic dark matter is given by

$$n_{\text{eq}} = \frac{g_\chi}{(2\pi)^{3/2}} T^3 x_\chi^{3/2} e^{-x_\chi}. \quad (61)$$

On the other hand, if a given species is relativistic, $m_i \ll T$, so $x_i \approx 0$. In that case, one can explicitly evaluate Eq. (58) to find

$$\rho_i(m_i \gg T) = \frac{\pi^2}{30} g_i T^4 \quad \text{for bosons,} \quad (62)$$

$$\rho_i(m_i \gg T) = \frac{7}{8} \cdot \frac{\pi^2}{30} g_i T^4 \quad \text{for fermions.} \quad (63)$$

Hence, it is customary to define the effective number of relativistic degrees of freedom g_* via the relation

$$\rho_{\text{tot}} = \frac{\pi^2}{30} g_* T^4. \quad (64)$$

Combining Eqs. (58), (59) and (64) implies that

$$g_*(T) = \frac{15}{\pi^4} \sum_{i=\text{all species}} g_i \int_{x_i}^{\infty} \frac{\sqrt{u^2 - x_i^2}}{\exp(u) \pm 1} u^2 du. \quad (65)$$

In principle, given a list of particles in the Standard Model, along with their masses m_i and internal degrees of freedom g_i , we can compute g_* using Eq. (65) and hence determine ρ which appears in the Hubble parameter mentioned earlier. However, there are some issues we need to address first. First of all, there are technically two types of effective degrees of freedom, one associated with energy density (defined in Eq. (64)) and one associated with entropy density, sometimes called g_{*s} . As long as our assumption that all particle species share a common temperature holds, any occurrence of g_{*s} can be replaced by g_* . The distinction is most relevant in the case of neutrinos. One can show that for $T \gtrsim 1$ MeV, weak interactions of the form $\bar{\nu}\nu \leftrightarrow e^+e^-$ (and permutations) occur at a rate much greater than the rate of expan-

sion of the Universe. For $T \lesssim 1$ MeV, the expansion rate dominates and the neutrinos are no longer in thermal equilibrium. The neutrinos then decouple from the thermal plasma and eventually acquire their own temperature which turns out to be $(4/11)^{1/3}$ times smaller than the photon temperature. When $T \approx m_e$, entropy stored in annihilated electron-positron pairs will therefore transfer to the photons instead of the neutrinos. The upshot of this is that for $T \lesssim 0.5$ MeV, g and g_{*s} differ by ≈ 1 , an effect which we will ignore and simply write $g = g_* = g_{*s}$.

The next issue is that Eq. (65) makes no reference or attempt to include the effects of QCD interactions. For leptons and electroweak gauge bosons we treat each individual species as a free particle and simply substitute its mass and internal degrees of freedom into Eq. (65) but evidently the situation is much more complicated for quarks and gluons. For a review of various approaches to dealing with QCD effects, see Ref. [66]. For up, down and strange quarks as well as gluons, we define an effective mass m_Λ at which these particles “appear.” This effective mass is related to the temperature range of the QCD phase transition, but the two are not equal. We treat charm, bottom and top quarks as free particles with their respective masses. We find that $m_\Lambda \approx 600$ MeV provides the best agreement with other, more

accurate results. In particular, we attempt to reproduce the results of Ref. [67] as shown in Figure 10. Our g is accurate to within $\approx 10\%$ everywhere. For ease of computation, fitting functions based on the functional forms of the individual species' contributions to g were created for our g and the g of Ref. [67]. The fitting functions are given in Appendix C.1.

8.3 The Relic Density Equation

Now that we have an understanding of g , Eq. (55) is well-defined because we know ρ_{tot} from Eq. (64) and thus H from Eq. (56). However, we would still like to make some transformations to simplify the integration process. For $x \gtrsim 1$, χ is non-relativistic, so we use n_{eq} given by Eq. (61). Since the entropy in a comoving volume is conserved, the quantity $s = (2\pi^2/45)gT^3$ is constant. We therefore scale n as $Y = n/s$. The equilibrium distribution becomes

$$Y_{\text{eq}} = \frac{45}{2\pi^4} \left(\frac{\pi}{8}\right)^{1/2} (g_\chi/g)x^{3/2}e^{-x}, \quad (66)$$

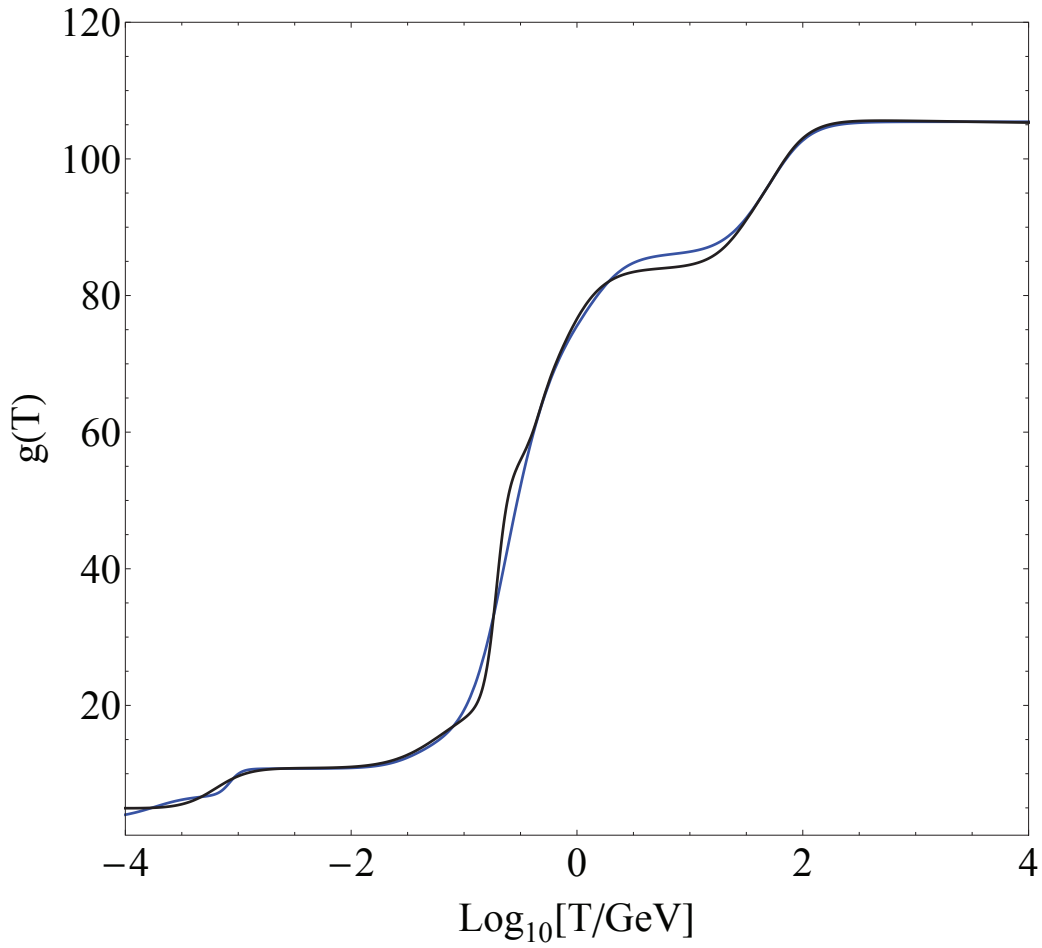


Figure 10: The number of effective relativistic degrees of freedom $g(T)$ of Ref. [67] (black line) and this work (blue line). Note that Ref. [67] only shows $g(T)$ for $-3 < \log_{10}(T) < 3$, so the values of T outside this range were extrapolated.

where now we specifically define $x = m_\chi/T$. After substituting H and ρ , the Boltzmann equation in Eq. (55) becomes

$$\frac{dY}{dx} = \frac{\lambda}{x^2} \left[1 + \frac{1}{3} \frac{d(\ln g)}{d(\ln T)} \right] \sqrt{g} (Y_{\text{eq}}^2 - Y^2), \quad (67)$$

where, in SI units, $\lambda = \sqrt{\pi/45G_n} m_\chi \langle \sigma v_{\text{rel}} \rangle$. To convert this to natural units but retain our ability to use m_χ in GeV and $\langle \sigma v_{\text{rel}} \rangle$ in cm^3s^{-1} , we set $G_n = 1$ and multiply λ by the Planck quantities $T_{\text{pl}}/E_{\text{pl}}V_{\text{pl}}$ with T_{pl} in seconds, E_{pl} in GeV and V_{pl} in cm^3 . The result is that $\lambda = C(m_\chi/\text{GeV})(\langle \sigma v_{\text{rel}} \rangle/\text{cm}^3\text{s}^{-1})$ where $C \approx 2.7636 \times 10^{35}$.

The present-day value of the Hubble parameter H_0 is written as $H_0 = 100h \text{ km/s Mpc}$, where $h = 0.673 \pm 0.012$ is the Hubble scale factor [23]. The relic abundance today is usually reported in terms of Ωh^2 , where Ω is the ratio of the present relic density to the critical mass density. The critical mass density is $\rho_{\text{crit}} = 3H_0^2/8\pi G_n$, where H_0 is the present value of the Hubble parameter when $T_0 = 2.7255 \pm 0.0006 \text{ K}$ [23]. The present relic density is $\rho_\chi = m_\chi s_0 Y_0$, where $s_0 \approx 2891.2 \text{ cm}^{-3}$ and $Y_0 = Y(x \rightarrow \infty)$ from Eq. (67). Combining all these factors together allows us to write $\Omega h^2 = KY_0(m_\chi/\text{GeV})$ with $K \approx 2.7889 \times 10^8$. Hence we will make one final

transformation, $\Omega(x) = Km_\chi Y(x)$ which leads to our final set of equations,

$$\Omega_{\text{eq}} = (4.03688 \times 10^7)(m_\chi/\text{GeV})(g_\chi/g)x^{3/2}e^{-x}, \quad (68)$$

$$\frac{d\Omega}{dx} = \frac{\Lambda}{x^2} \left[1 + \frac{1}{3} \frac{d(\ln g)}{d(\ln T)} \right] \sqrt{g} (\Omega_{\text{eq}}^2 - \Omega^2), \quad (69)$$

with $\Lambda = 9.9093 \times 10^{26} \langle \sigma v_{\text{rel}} \rangle$. Now, $\Omega(x \rightarrow \infty)$ is exactly the present value of Ωh^2 (note that h^2 is already folded into $\Omega(x \rightarrow \infty)$) so we can simply integrate this equation directly from $\Omega(x=1) = \Omega_{\text{eq}}(x=1)$ and compare the asymptotic value to the measured result $\Omega h^2 = 0.1193 \pm 0.0014$ [68].

The only missing piece is now the quantity $\langle \sigma v_{\text{rel}} \rangle$. By definition, the thermally averaged cross section is

$$\langle \sigma v_{\text{rel}} \rangle = \int_0^\infty (\sigma v_{\text{rel}}) f_{\text{MB}}(v) dv, \quad (70)$$

where $f_{\text{MB}}(v)$ is the Maxwell-Boltzmann distribution (valid as long as the dark matter particles are non-relativistic, which they are by assumption) which can be written in terms of the reduced mass $m_r = m_\chi/2$ and the temperature T as

$$f_{\text{MB}}(v) = 4\pi \left(\frac{m_r}{2\pi T} \right)^{3/2} v^2 e^{-m_r v^2/2T}. \quad (71)$$

We can easily write Eq. (70) in terms of x as

$$\langle \sigma v_{\text{rel}} \rangle = \frac{x^{3/2}}{2\pi^{1/2}} \int_0^\infty (\sigma v_{\text{rel}}) v^2 e^{-xv^2/4} dv, \quad (72)$$

which can be readily evaluated for a given cross section and substituted into Eq. (69).

8.3.1 S-Wave Annihilation

In the case where the WIMPs annihilate with no relative angular momentum, we say that the annihilation is of the s-wave type. The implication for the cross section is that σv_{rel} is approximately constant at low relative velocities. For a dark matter mass $m_\chi \sim 100$ GeV one can show that freeze-out occurs at a temperature $T \sim m_\chi/20$. Equivalently, freeze-out occurs when the Hubble-expansion rate $H(T)$ is equal to the dark matter annihilation rate $\langle \sigma v_{\text{rel}} \rangle n(T)$. Combining those two facts leads to the well-known approximation $\Omega h^2 \sim 3 \times 10^{-27} \text{cm}^3 \text{s}^{-1} / \langle \sigma v_{\text{rel}} \rangle$ [70] and, since $\Omega h^2 \sim 0.1$, the “canonical” value of the thermally averaged cross section is generally taken to be around $3 \times 10^{-26} \text{cm}^3 \text{s}^{-1}$. We will write $\sigma v_{\text{rel}} = \alpha$ for some constant α and define the

dimensionless parameter $\bar{\alpha}$ as

$$\alpha = \bar{\alpha} \times 10^{-26} \text{ cm}^3 \text{ s}^{-1}. \quad (73)$$

Hence, in Eq. (72), the constant simply factors out and we have $\langle \sigma v_{\text{rel}} \rangle = \alpha$.

Substituting this into Eq. (69) gives

$$\frac{d\Omega}{dx} = \frac{\Lambda_s}{x^2} \left[1 + \frac{1}{3} \frac{d(\ln g)}{d(\ln T)} \right] \sqrt{g} (\Omega_{\text{eq}}^2 - \Omega^2), \quad (74)$$

where $\Lambda_s = (9.9093)\bar{\alpha}$; note that we expect $\bar{\alpha} \sim 1$.

In summary, we pick trial values of m_χ/GeV and $\bar{\alpha}$ and integrate Eq. (74) with Eq. (68) and compare the asymptotic value of $\Omega(x)$ to the known result Ωh^2 ; if they agree, then m_χ/GeV and $\langle \sigma v_{\text{rel}} \rangle = \bar{\alpha} \times 10^{-26} \text{ cm}^3 \text{ s}^{-1}$ are physically allowed.

8.3.2 P-Wave Annihilation

In the case where the WIMPs annihilate with relative angular momentum 1, we say that the annihilation is of the p-wave type. The implication for the cross section is that $\sigma v_{\text{rel}} = \beta v_{\text{rel}}^2$. Substituting this into Eq. (72) gives $\langle \sigma v_{\text{rel}} \rangle = 6\beta/x$. Setting $\langle \sigma v \rangle$ equal to the canonical value of $3 \times 10^{-26} \text{ cm}^3 \text{ s}^{-1}$

and taking $x = 20$ as in the s-wave approximation, we see that we should expect $\beta \simeq 10^{-25} \text{ cm}^3 \text{ s}^{-1}$. Again, anticipating this order of magnitude, we will define

$$\beta = \bar{\beta} \times 10^{-25} \text{ cm}^3 \text{ s}^{-1}. \quad (75)$$

Substituting the thermally averaged cross section into Eq. (69) gives

$$\frac{d\Omega}{dx} = \frac{\Lambda_p}{x^3} \left[1 + \frac{1}{3} \frac{d(\ln g)}{d(\ln T)} \right] \sqrt{g} (\Omega_{\text{eq}}^2 - \Omega^2) \quad (76)$$

where $\Lambda_p = (594.558)\bar{\beta}$; note that we expect $\bar{\beta} \sim 1$ which will imply that the allowed cross section is $\bar{\beta} \times 10^{-25} v_{\text{rel}}^2 \text{ cm}^3 \text{ s}^{-1}$.

8.3.3 Resonant Annihilation

For a scalar WIMP annihilating through a scalar mediator particle R in the s channel, the Lagrangian contains a term $(\mu/2)\chi\chi R$ for some constant μ .

The annihilation cross section can be written as

$$\sigma v_{\text{rel}} = \frac{\Gamma_R}{E_{\text{cm}}} \frac{2\mu^2}{(E_{\text{cm}}^2 - m_R^2)^2 + m_R^2 \Gamma_R^2}, \quad (77)$$

where m_R and Γ_R are the mass and width of the mediator, respectively. Since we're starting the integration at $x = 1$, we have that $m_\chi > T$ for all times, so we can write a non-relativistic expression for the center of mass energy E_{cm} . Since there are two χ s, each with velocity $v_{\text{rel}}/2$ in the center of mass frame, we have

$$E_{\text{cm}}^2 = m_{\text{tot}}^2 + p_{\text{cm}}^2 \approx (2m_\chi)^2 + \left(2m_\chi \frac{v_{\text{rel}}}{2}\right)^2 = 4m_\chi^2 + m_\chi^2 v_{\text{rel}}^2. \quad (78)$$

In general, we're most concerned with writing down a version of Eq. (77) which accurately captures the behavior of the cross section near the resonance peak. Therefore, we will write E_{cm}^2 in Eq. (77) to second order in v_{rel} as it appears in Eq. (78). The factor of $1/E_{\text{cm}}$ out front only affects the overall shape of the curve and not the location of the resonance itself. For this reason, we will simplify our expression by writing $1/E_{\text{cm}} \approx 1/2m_\chi$. Substituting these relations into Eq. (77) gives

$$\sigma v_{\text{rel}} = \frac{\mu^2}{m_\chi} \frac{\Gamma_R}{(4m_\chi^2 - m_R^2 + m_\chi^2 v_{\text{rel}}^2)^2 + m_R^2 \Gamma_R^2}. \quad (79)$$

It can quickly be shown by factoring out m_χ^2 from the denominator and multiplying the entire expression by $m_R/2m_\chi$ (approximately equal to 1 near

the resonance) that Eq. (79) can be written as [69]

$$\sigma v_{\text{rel}} = \frac{\mu^2}{2m_\chi^4} \frac{\gamma_R}{(v_{\text{rel}}^2 - \epsilon_R)^2 + \gamma_R^2}, \quad (80)$$

where

$$\epsilon_R = \frac{m_R^2 - (2m_\chi)^2}{m_\chi^2} \quad \text{and} \quad \gamma_R = \frac{m_R \Gamma_R}{m_\chi^2}. \quad (81)$$

What do these new variables mean? Let's consider what happens if $2m_\chi < m_R$, which corresponds to $\epsilon_R > 0$. In this case, the dark matter particles don't have enough rest energy to be at the resonance peak, but increases in v_{rel} caused by thermal excitations can push them up to it. If $2m_\chi > m_R$ then $\epsilon_R < 0$ and the dark matter particles have too much rest energy to ever be at the resonance. Increases in v_{rel} caused by thermal excitations will push them away from the peak. Of course, if $2m_\chi = m_R$, then $\epsilon_R = 0$ and the dark matter particles are exactly at the resonance. On the other hand, γ_R is effectively the width of the resonance, scaled by the mass of the χ . If γ_R is very small, then Eq. (80) approaches a delta function centered at $v_{\text{rel}}^2 = \epsilon_R$.

With this new expression for the cross section, we can compute the thermally averaged cross section as usual with Eq. (72). One can show (see Appendix D for details of the computation) that the result can be expressed

as

$$\langle \sigma v_{\text{rel}} \rangle = -\frac{\sqrt{\pi}\mu^2}{4m_\chi^4} x \text{Re} \left[i\theta e^{\theta^2} \text{erfc}(\theta) \right], \quad (82)$$

where

$$\theta = \sqrt{x(-\epsilon_R + i\gamma_R)}/2, \quad (83)$$

and where $\text{erfc}(z) = 1 - \text{erf}(z)$ and $\text{erf}(z)$ is the standard error function, which is well-tabulated even for complex arguments. We will take

$$\mu = \bar{\mu} \times 10^{-13} \text{ GeV} \quad (84)$$

to obtain an overall factor of 10^{-26} in front of the cross section. Therefore, substituting Eq. (82) into Eq.(69) gives

$$\frac{d\Omega}{dx} = \frac{\Lambda_R}{x} \text{Re} \left[i\theta e^{\theta^2} \text{erfc}(\theta) \right] \left[1 + \frac{1}{3} \frac{d(\ln g)}{d(\ln T)} \right] \sqrt{g} (\Omega_{\text{eq}}^2 - \Omega^2), \quad (85)$$

where $\Lambda_R = -9.9093\sqrt{\pi}\bar{\mu}^2/4m_\chi^4$. In summary, for a mediator particle of mass m_R and width Γ_R , we solve Eq. (85) using Eq. (83) and Eq. (81); if the result is consistent with the observed relic density, then the parameter set $(\bar{\mu} \times 10^{-13} \text{ GeV}, m_\chi)$ is physically allowed by observation. Since the cross section changes by many orders of magnitude, especially near the resonance,

we expect the allowed values of $\bar{\mu}$ to change by many orders of magnitude as m_χ varies.

There is one small detail we still need to address. So far we have been saying that the present relic density is obtained by integrating to $x \rightarrow \infty$. Technically this is not true since the amount of time that has passed since the early Universe is clearly finite. However, $kT_0 \sim 10^{-13}$ GeV and since we're generally concerned with 10^{-1} GeV $< m_\chi < 10^4$ GeV, the “present time” corresponds to at least $x \sim 10^{12}$. For any practical implementation, we can not integrate this far so we have to pick some “large enough” value to stop at. This is usually taken to be $x \approx 1000$. We will have more to say about the accuracy of this choice in Section 9.5.

9 Integration of the Boltzmann Equation Using Möbius Schemes

The only legitimate use of a computer is to play games.

Eugene Jarvis, *Supercade*

9.1 Preliminary Computations

Before we discuss the actual implementation of a numerical algorithm for integrating Eq. (69), we will quickly comment on the derivative $g_D(T)$, where

$$g_D(T) = \frac{d(\ln g)}{d(\ln T)}. \quad (86)$$

It is clearly far too slow to compute this manually at each step from $g(T)$. Instead, we pre-compute a list of values for this term and fit yet another function to the result. In principle one could simply fit the entire term $[1 + (1/3)g_D(T)]\sqrt{g}$, but the shape of this function is not well-suited to elementary fits, particularly near $T \sim 0.1$ GeV where there is a small oscillation superimposed over a relatively flat region. A yet faster method would be to just use the pre-computed values at every step. In any case the details of the fit for the function $g_D(T)$ are given in Appendix C.2.

9.2 Introduction to Möbius Schemes

We're faced with the task of having to integrate the relic density equation over a fairly large range. The first thing to note is that the equation for the relic density Eq. (69) is of the Riccati form [71], given in general as

$$\dot{y} = a(t)y + b(t) - yc(t)y - yd(t), \quad (87)$$

where $y(t)$ is an $n \times m$ matrix and the coefficients $a(t), b(t), c(t)$ and $d(t)$ are $n \times n, n \times m, m \times n$ and $m \times m$ matrices, respectively. Fortunately, the Riccati equation arises naturally in a fairly large number of applications and there have been many proposed numerical and semi-analytical algorithms to solve it [72, 73, 74, 75, 76, 77, 78, 79, 80]. In this work, we will employ a class of numerical methods called Möbius schemes, introduced in Ref. [81].

We will focus on the case where $n = m = 1$, so that all the functions in Eq. (87) are scalars. Therefore, Eq. (87) can be written as

$$\dot{y} = b(t) + [a(t) - d(t)]y - c(t)y^2. \quad (88)$$

There is now an ambiguity in choosing $a(t)$ and $d(t)$ but we will return to

this later. Let us now define the Riccati matrix $R(t)$ as

$$R(t) = \begin{pmatrix} a(t) & b(t) \\ c(t) & d(t) \end{pmatrix}. \quad (89)$$

If the functions $u(t)$ and $v(t)$ satisfy

$$\begin{aligned} \frac{d}{dt} \begin{pmatrix} u(t) \\ v(t) \end{pmatrix} &= \begin{pmatrix} a(t) & b(t) \\ c(t) & d(t) \end{pmatrix} \begin{pmatrix} u(t) \\ v(t) \end{pmatrix} \\ &\equiv R(t) \begin{pmatrix} u(t) \\ v(t) \end{pmatrix}, \end{aligned} \quad (90)$$

then $y(t) = u(t)/v(t)$ solves the Riccati equation. We can show this by direct substitution via

$$\begin{aligned} \dot{y} &= \frac{d}{dt} \left[\frac{u(t)}{v(t)} \right] \\ &= \frac{\dot{u}}{v} - \frac{u\dot{v}}{v^2} \\ &= \frac{1}{v} (au + bv) - \frac{u}{v^2} (cu + dv) \\ &= a \left(\frac{u}{v} \right) + b - c \left(\frac{u}{v} \right)^2 - d \left(\frac{u}{v} \right) \\ &= b(t) + [a(t) - d(t)] y - c(t) y^2, \end{aligned} \quad (91)$$

as required. Consider the two vectors $(u(t_i), v(t_i))^T$ and $(u(t_{i+1}), v(t_{i+1}))^T$, where $t_{i+1} = t_i + h$. It can be shown that there exists a linear transformation, namely a Möbius transformation, which takes the vector $(u_i, v_i)^T$ to $(u_{i+1}, v_{i+1})^T$. The matrix of the Möbius transformation $\mathcal{M}(t)$ is given in terms of four unknown functions as

$$\mathcal{M}(t) = \begin{pmatrix} \alpha(t) & \beta(t) \\ \gamma(t) & \delta(t) \end{pmatrix}. \quad (92)$$

We will call these functions the Möbius functions. Then, by definition, we can write

$$\begin{aligned} \begin{pmatrix} u_{i+1} \\ v_{i+1} \end{pmatrix} &= \begin{pmatrix} \alpha_i(h) & \beta_i(h) \\ \gamma_i(h) & \delta_i(h) \end{pmatrix} \begin{pmatrix} u_i \\ v_i \end{pmatrix} \\ &\equiv \mathcal{M}_i(h) \begin{pmatrix} u_i \\ v_i \end{pmatrix}. \end{aligned} \quad (93)$$

The subscript i on the Möbius functions emphasizes that they are determined

at t_i . Hence, if we know that at time t_i we have $y_i = u_i/v_i$, we can write

$$\begin{aligned}
y_{i+1} &= \frac{u_{i+1}}{v_{i+1}} \\
&= \frac{\alpha_i(h)u_i + \beta_i(h)v_i}{\gamma_i(h)u_i + \delta_i(h)v_i} \\
&= \frac{\alpha_i(h)y_i + \beta_i(h)}{\gamma_i(h)y_i + \delta_i(h)}, \tag{94}
\end{aligned}$$

after multiplying the numerator and denominator by $1/v_i$. Evidently we require the denominator of Eq. (94) to be nonzero. It turns out that this condition is satisfied for the scalar Boltzmann equation (see Section 9.3). Note also that that Eq. (94) is completely exact; the approximation enters when we try to actually calculate the Möbius functions - let us do that now. First define $\mathbf{w}_i(h) = (u(t_i + h), v(t_i + h))^T$ so that the Möbius transformation reads $\mathbf{w}_i(h) = \mathcal{M}_i(h)\mathbf{w}_i(0)$. For numerical methods, h will be small, so we can expand the left hand side as

$$\mathbf{w}_i(h) \simeq \mathbf{w}_i(0) + \dot{\mathbf{w}}_i(0)h + \frac{1}{2}\ddot{\mathbf{w}}_i(0)h^2 + \mathcal{O}(h^3). \tag{95}$$

But then, we have $\dot{\mathbf{w}}_i(0) = R(t_i)\mathbf{w}_i(0)$ at all times from the original definition

of \mathbf{w} . Substituting this into Eq. (95) gives

$$\mathbf{w}_i(h) \simeq \mathbf{w}_i(0) + R(t_i)\mathbf{w}_i(0)h + \frac{1}{2}(\dot{R}(t_i) + R^2(t_i))\mathbf{w}_i(0)h^2 + \mathcal{O}(h^3). \quad (96)$$

But then, this entire expression is proportional to $\mathcal{M}_i(h)\mathbf{w}_i(0)$, so we have

$$\mathcal{M}_i(h) \simeq \mathbb{I}_2 + R(t_i)h + \frac{1}{2}(\dot{R}(t_i) + R^2(t_i))h^2 + \mathcal{O}(h^3). \quad (97)$$

We can estimate the derivative using the finite difference $\dot{R}(t_i) = (2/h)[R(t_i + h/2) - R(t_i)] + \mathcal{O}(h)$. This will introduce extra error terms proportional to h^3 so Eq. (97) becomes

$$\mathcal{M}_i(h) \simeq \mathbb{I}_2 + R(t_i + h/2)h + \frac{1}{2}R^2(t_i)h^2 + \mathcal{O}(h^3). \quad (98)$$

Finally, we note that $R^2(t_i + h/2) \simeq R^2(t_i) + \mathcal{O}(h)$, hence at the cost of introducing additional error terms proportional to h^3 , we have the simple formula

$$\mathcal{M}_i(h) \simeq \mathbb{I}_2 + R(t_i + h/2)h + \frac{1}{2}R^2(t_i + h/2)h^2 + \mathcal{O}(h^3). \quad (99)$$

This has the important advantage of requiring only one evaluation of $R(t)$ at each time step. When integrating between t_0 and t_{max} we take $N = (t_{max} - t_0)/h \sim 1/h$ steps and since the local truncation error goes like h^3 , we expect the global error to go like $Nh^3 \sim h^2$. Now we have a numerical method suitable for application to the problem at hand.

9.3 Application to the Relic Density

Comparing the form of the relic density equation in Eq. (69) to the general form of the scalar Riccati equation in Eq. (88), we see that the Riccati coefficients are given by

$$a(x) - d(x) = 0, \tag{100}$$

$$b(x) = \frac{\Lambda}{x^2} \left[1 + \frac{1}{3} \frac{d(\ln g)}{d(\ln T)} \right] \sqrt{g} \Omega_{\text{eq}}^2, \tag{101}$$

$$c(x) = \frac{\Lambda}{x^2} \left[1 + \frac{1}{3} \frac{d(\ln g)}{d(\ln T)} \right] \sqrt{g}. \tag{102}$$

This is the problem we alluded to earlier concerning the ambiguity in the choice of $a(t)$ and $d(t)$. It turns out that this is just a specific case of the more general observation that a given Riccati equation does not uniquely determine the associated Riccati matrix (although the converse is obviously true). In

fact, it turns out that the freedom in choosing $a(t)$ and $d(t)$ is an advantage in general. By changing $a(t)$ and $d(t)$ we can change the eigenvalues of the Riccati matrix, which changes the accuracy of the numerical methods. In general, if there are eigenvalues of R with large negative real parts then the stiffness of the system may become an issue. In particular, the relic density equation is stiff. On the other hand, the general accuracy of the method is improved when R is taken to have eigenvalues which are small in absolute value. We can quickly verify that for our system, in general with $d(t) = a(t)$, the eigenvalues of R are $\lambda = a \pm bc$. The exact method by which a should be chosen is not fully understood; however, based on the previous comments there are two immediate candidates: $a(t) = 0$ or $a(t) = b(t)c(t)$. In the case of $a(t) = 0$, the eigenvalues of R are minimized in absolute value, so we expect this method to have the highest overall accuracy. The choice $a(t) = b(t)c(t)$ eliminates the negative real part of the eigenvalues, so we expect this method to perform better with respect to handling stiffness. We can compare these two approaches using a standard convergence analysis as shown in Figure 11. We use the s-wave annihilation of Eq. (74) with $m_\chi = 100 \text{ GeV}$, $\alpha = 2.2$ and integrate from $x = 1$ to $x = 1000$ with $h \in \{0.1, 0.05, 0.01, 0.005, 0.001\}$. The “true” value is taken to be the same integration with $h \rightarrow h/10$; then

the error is the difference between these two results. Since the slopes are

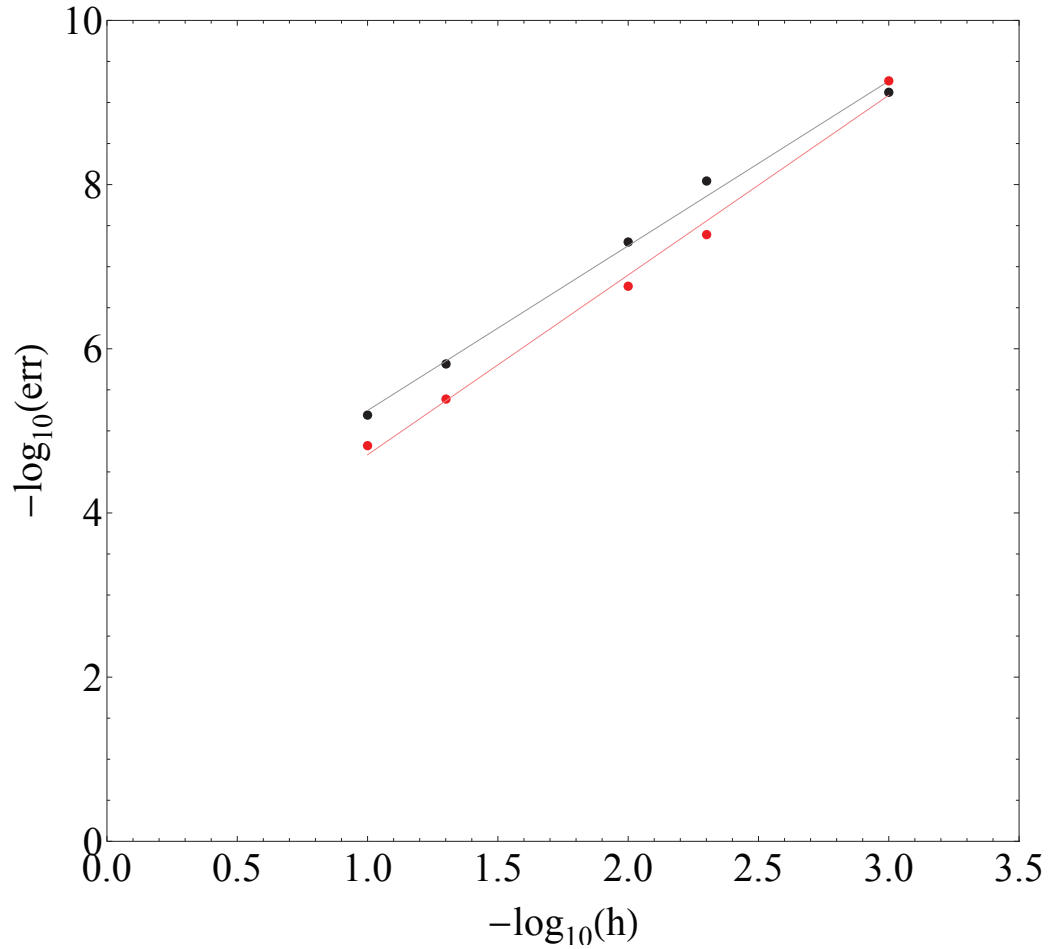


Figure 11: Convergence analysis of two different Möbius schemes for s-wave annihilation. The black dots correspond to $a(t) = 0$ and the black line has equation $y = 2.01x + 3.24$. The red dots correspond to $a(t) = b(t)c(t)$ and the red line has equation $y = 2.19x + 2.52$.

both ≈ 2 we have a globally second order method as expected. We see that the choice $a(t) = 0$ does indeed have better overall accuracy, but the choice

$a(t) = b(t)c(t)$ has faster convergence, indicated by its higher slope. Since we generally want to use values of h between 0.1 and 0.001, we will henceforth take $a(t) = 0$ to minimize the overall error. Hence, we can directly compute the Möbius matrix

$$\mathcal{M}^{(2)}(x_0, h) = \left(\begin{array}{cc} 1 + \frac{1}{2}b(t)c(t)h^2 & hb(t) \\ hc(t) & 1 + \frac{1}{2}b(t)c(t)h^2 \end{array} \right) \Bigg|_{t=x_0+h/2}, \quad (103)$$

where the superscript is to emphasize that this is a second order method. And finally, by using Eq. (94), the formula for the update of the relic density in terms of the elements of Eq. (103) is

$$\Omega_{\text{Möbius}}^{(2)}(x_0 + h) = \frac{\mathcal{M}_{11}^{(2)}(x_0, h)\Omega(x_0) + \mathcal{M}_{12}^{(2)}(x_0, h)}{\mathcal{M}_{21}^{(2)}(x_0, h)\Omega(x_0) + \mathcal{M}_{22}^{(2)}(x_0, h)}. \quad (104)$$

Evidently the actual numerical implementation of this can be trivially optimized by noting, for example, that $\mathcal{M}_{11}^{(2)} = \mathcal{M}_{22}^{(2)}$ but we will return to the practical details later. One final note is that the denominator of Eq. (104) is strictly positive since $b(t)$ and $c(t)$ are strictly positive (see Eqs. (101) and (102)) and $\Omega(x)$ is strictly positive by definition. Hence, it is impossible to accidentally choose a value of h such that Eq. (104) is ill-defined.

9.4 Comparison with Runge-Kutta

Now that we have some understanding of the Möbius scheme, let us pause for a moment and compare it to an equivalent Runge-Kutta scheme. The second order Runge-Kutta (RK2) scheme updates the relic density as

$$k_1 = \Omega'(x_0, \Omega(x_0)), \quad (105)$$

$$k_2 = \Omega'(x_0 + h, \Omega(x_0) + hk_1), \quad (106)$$

$$\Omega_{\text{RK2}}(x_0 + h) = \Omega(x_0) + \frac{1}{2}h(k_1 + k_2). \quad (107)$$

We will examine the behavior of this method by manually computing the first two time steps. During the first time step, we have $x_0 = 1$ and $\Omega(x_0) = \Omega_{\text{eq}}(1)$ for $m = 100$ GeV, hence $\Omega'(x_0, \Omega(x_0)) = 0$, so $k_1 = 0$. On the other hand, k_2 pushes the value of x_0 away slightly so that we end up with a term like $\Omega_{\text{eq}}^2(x_0 + h) - \Omega_{\text{eq}}^2(x_0) \simeq 2\Omega_{\text{eq}}(x_0)\Omega'_{\text{eq}}(x_0)h$. Since $\Omega_{\text{eq}}(x_0) \sim 10^8$, and the rest of the prefactor in the derivative is $\sim 10^2$ we have $k_2 \sim 10^{18}h$, so $\Omega_{\text{RK2}}(x_0 + h) \sim 10^8 + 10^{18}h^2$. In order for this not to immediately blow up, we at least need $10^{18}h^2 \sim 10^8$, so we need $h \sim 10^{-5}$ which gives $\Omega(x_0 + h) \sim 2\Omega_{\text{eq}}(x_0)$. But then, at the next time step, in $k_1 = \Omega'(x_0 + h, \Omega(x_0 + h))$ we have the term $\Omega_{\text{eq}}^2(x_0 + h) - 4\Omega_{\text{eq}}^2(x_0) \sim \Omega_{\text{eq}}^2(x_0) \sim 10^{16}$. Combining this with

the prefactor, we'll have $k_1 \sim 10^{18}$. Barring a miraculous cancellation with k_2 (which does not happen; in fact k_2 is even bigger than k_1) the result of the second time step is $\Omega_{\text{RK2}}(x_0 + 2h) \sim 10^8 + 10^{18}h$. Even with $h \sim 10^{-5}$, this continues to blow up, so it turns out that the first step was too big and we actually need something like $h \sim 10^{-10}$. In fact, this time step will keep the numerical solution under control but for obvious reasons, we don't want to use such a small increment especially when we need to integrate over several orders of magnitude in x . Now, to be completely fair, Ω changes by several orders of magnitude only in the range $1 \leq x \lesssim 20$, not over the entire range. Hence, one could argue that an adaptive time step would remove some of the difficulty. This is true, but even integrating from $x = 1$ to $x = 2$ is still on the order of ten billion iterations which corresponds to twenty billion evaluations of a reasonably complicated derivative. Extending this to the classical fourth-order Runge-Kutta method doesn't do much to help the situation. We therefore conclude that explicit Runge-Kutta methods of this type are not suitable for the relic density problem. Of course, this is to be expected since the equation is numerically stiff. It's worth mentioning that one can also attempt to rectify this problem with a transformation of the form $W = \ln \Omega$ as in Ref. [67]. The idea is that now W does not change by many

orders of magnitude. However, the transformed equation will contain a factor of $\exp(2\Omega_{\text{eq}} - \Omega) - \exp(\Omega)$, so we still have the same problem as before, namely, trying to calculate the difference between exponentially sensitive terms.

Now let us repeat this analysis with our Möbius scheme. To simplify the process, we will use the first order scheme, which corresponds to discarding the h^2 terms in the second order scheme from Eqs. (103) and (104). The relic density is updated via

$$\Omega_{\text{Möbius}}^{(1)}(x_0 + h) = \frac{\Omega(x_0) + b(x_0)h}{\Omega(x_0)c(x_0)h + 1}. \quad (108)$$

Again, we begin the integration at $x_0 = 1$, so $\Omega(x_0) = \Omega_{\text{eq}}(1) \sim 10^8$. The Riccati coefficients are $c(x_0) \sim \text{prefactor} \sim 10^2$ and $b(x_0) \sim \text{prefactor} \cdot \Omega_{\text{eq}}^2(x_0) \sim 10^{18}$. For a reasonable time step $h \sim 10^{-2}$ we have

$$\begin{aligned} \Omega_{\text{Möbius}}(x_0 + h) &\sim \frac{10^8 + 10^{18} \cdot 10^{-2}}{10^8 \cdot 10^2 \cdot 10^{-2} + 1} \\ &\sim 10^8. \end{aligned} \quad (109)$$

So $\Omega_{\text{Möbius}}(x_0 + h) \sim \Omega(x_0)$, as is required from a numerical scheme. One could take a second step to show that this will continue to be true, but it should be clear now that this is a general feature of the method. To wit, the Möbius

functions do not depend on the actual value of $\Omega(x_0)$. Of course, the updated step does, but the transformation is such that it automatically adapts to its size, as we just saw. This analysis was done with the first order method, but the second order method is obtained with no additional evaluations of $b(t)$ and $c(t)$, another advantage over second-order Runge-Kutta.

To conclude this section, we would like to address the transformation of Riccati differential equations to second-order linear differential equations [82]. In particular, the general solution of $y' + r(x)y^2 + q(x) = 0$ can be written as

$$y(x) = \frac{c_1 z_1'(x) + c_2 z_2'(x)}{r(x)(c_1 z_1(x) + c_2 z_2(x))}, \quad (110)$$

where c_1, c_2 are arbitrary constants and $z_1(x), z_2(x)$ are solutions of

$$z'' + \left[p(x) - \frac{r'(x)}{r(x)} \right] z' = 0. \quad (111)$$

In fact, Eq. (111) is trivially reducible to first order, so one can write down the solutions $z_1(x)$ and $z_2(x)$, at least formally. The problem with this is that $p(x)$ depends on $g(T)$ in a complicated way, and the formal solution requires its anti-derivative. Still this solution is, strictly speaking, completely analytic and may be of some use on its own. The other idea is that one can

use Runge-Kutta to solve Eq. (111) (since it is linear) and then compute the true solution using Eq. (110). Again, formally this will work, but using Eq. (111) requires computing the derivative of $r(x)$ which is highly non-trivial. We conclude that Runge-Kutta methods may be applied to this problem at the expense of requiring the computation of derivatives of the Riccati coefficients. Since the Möbius scheme requires no such operations, it seems to be the superior method.

9.5 Far-field Approximations

We saw in Section 8 that the true value of the relic density is obtained when the “time” parameter x is integrated from $x \sim 1$ to a large, effectively infinite value. Practically, it is customary to integrate up to $x \sim 1000$; we will now evaluate the accuracy of this choice and, in doing so, obtain a useful approximation to be used later.

For large x , Ω_{eq} goes to zero exponentially, hence we can write Eq. (74)

as

$$\frac{d\Omega}{dx} \simeq -\frac{\Lambda_s}{x^2} \left[1 + \frac{1}{3} \frac{d(\ln g)}{d(\ln T)} \right] \sqrt{g}\Omega^2. \quad (112)$$

This is clearly a separable differential equation, so we have

$$\int_{\Omega_\infty}^{\Omega} \Omega^{-2} d\Omega = -\Lambda_s \int_{\infty}^x \left[1 + \frac{1}{3} \frac{d(\ln g)}{d(\ln T)} \right] \sqrt{g} x^{-2} dx, \quad (113)$$

$$\frac{1}{\Omega_\infty} - \frac{1}{\Omega} = \Lambda_s \int_x^{\infty} \left[1 + \frac{1}{3} \frac{d(\ln g)}{d(\ln T)} \right] \sqrt{g} x^{-2} dx. \quad (114)$$

Hence, if we integrate out to some x value, x_{large} we can get a more accurate estimate of Ω_∞ via

$$\Omega_\infty = \frac{\Omega(x_{\text{large}})}{1 + \Omega(x_{\text{large}})\Lambda_s \mathcal{G}(m, x_{\text{large}})}, \quad (115)$$

$$\mathcal{G}(m, x) = \int_x^{\infty} \left[1 + \frac{1}{3} \frac{d(\ln g)}{d(\ln T)} \right] \sqrt{g} x^{-2} dx. \quad (116)$$

The relative error in $\Omega(x_{\text{large}})$ is therefore

$$\begin{aligned} \text{error}(x_{\text{large}}) &= \frac{|\Omega(x_{\text{large}}) - \Omega_\infty|}{\Omega_\infty} \\ &= \Lambda_s \Omega(x_{\text{large}}) \mathcal{G}(m, x_{\text{large}}). \end{aligned} \quad (117)$$

A quick computation shows that $\mathcal{G}(m_\chi = 10^4 \text{ GeV}, 1000) \approx 0.01$; since \mathcal{G} is an increasing function of m_χ , we can write $\mathcal{G}(m, 1000) \leq 0.01$ for $m_\chi < 10^4 \text{ GeV}$. If $\Omega(x_{\text{large}}) \approx 0.1$ and $\alpha \sim 1$, then $\Lambda \sim 10 \text{ error}(x_{\text{large}}) \lesssim 1\%$. So we conclude

that integrating out to $x = 1000$ introduces an error on the result of about 1%. This will likely be swamped by other errors, most notably in g , so it appears that $x = 1000$ is indeed, “far enough.”

We will now provide a simple argument based on the previous comments which can greatly speed up the integration. From Eq. (68), we have

$$\begin{aligned}\Omega_{\text{eq}} &= (4.03688 \times 10^7)(m_\chi/\text{GeV})(g_\chi/g)x^{3/2}e^{-x} \\ &\leq (4 \times 10^7)(10^4)(2/2)x^{3/2}e^{-x} \\ &\leq 10^{12}x^{3/2}e^{-x},\end{aligned}\tag{118}$$

so

$$\Omega_{\text{eq}}^2 \leq 10^{24}x^3e^{-2x},\tag{119}$$

and

$$\Omega_{\text{eq}}^2(x = 100) \leq 10^{-56}.\tag{120}$$

Hence, if we integrate up to $x_{\text{large}} = 100$ we can very safely use the approximation that the Ω_{eq}^2 term is negligible and Eq. (115) is valid with $x_{\text{large}} = 100$. We will refer to this method as the “far field” method. To illustrate its performance, we will consider s-wave annihilation with $m_\chi = 100$ GeV and $\alpha = 2.2$.

First, we integrate from $x = 1$ to $x = 10,000$ with $h = 0.001$ and $h = 0.0005$ to find that the true value is $\Omega h^2 = 0.1111381 \pm 0.000001$. Using the “vanilla” Möbius method and integrating from $x = 1$ to $x = 1000$ with $h = 0.01$ gives $\Omega h^2 \approx 0.1121780$, corresponding to a relative error of 0.935%, which is in agreement with our previous claim that the error should be $\sim 1\%$. On the other hand, using the far-field method, we integrate from $x = 1$ to $x = 100$ with $h = 0.01$ and apply \mathcal{G} and Eq. (115) to find $\Omega h^2 \approx 0.1110535$. This corresponds to a relative error of 0.0761%. We conclude that the far-field method is not only ten times faster than the vanilla method, but is also ten times more accurate.

There is one obvious issue with the far-field method: to use it, we need to actually compute $\mathcal{G}(m_\chi, 100)$. Depending on the functional form of the cross section, and the numerical integration scheme used for \mathcal{G} , it may be faster to compute it numerically at discrete points for each mass. On the other hand, if one is searching through a very large number of masses, it is probably better to find an explicit functional form for $\mathcal{G}(m_\chi, 100)$ once and be done with it. For s-wave annihilation we have determined a fitting function for $\mathcal{G}(m_\chi, 100)$ which can be found in Appendix C.3.

Particle χ	g_χ
Real scalar	1
Complex scalar	2
Majorana Fermion	2
Dirac Fermion	4
Vector boson	3

Table 11: Intrinsic degrees of freedom g_χ for various particle types.

9.6 Summary of Algorithm

For convenience, we provide a pseudo-code outline of a practical implementation of the results discussed so far. The process Algorithm 1 takes in a mass m_χ and the scaling factor of the cross section $\bar{\alpha}$ and returns the quantity Ωh^2 at the present date. It assumes that we have expressions for $g(T)$ and $g_D(T) = d \ln g / d \ln T$ which can be found in Appendix C. The algorithm is nearly identical for p-wave and resonant-annihilation cross sections. For different particle types, the number of intrinsic degrees of freedom g_χ will be different. Table 11 summarizes the values of g_χ for the most common particle types.

Algorithm 1 Calculating the s-wave relic density using the Möbius scheme

Require: Fitting functions from Appendix C or some other method of calculating terms that depend on $g(T)$.

```

1: function  $\Omega h^2(m, \bar{\alpha}; h = 0.01)$     ▷  $h = 0.01$  is the suggested time step.
2:    $g_\chi = 2$                                ▷ Can put other choices here (see Table 11)
3:    $\Lambda = (9.9093) * \bar{\alpha}$                  ▷  $\bar{\alpha}$  is defined in Eq. 73
4:    $x_0 = 1$ 
5:    $\Omega_0 = (4.03688 * 10^7) * m * (g_\chi/g(m, x_0)) * x_0^{3/2} * \exp(-x_0)$   ▷ This is
    $\Omega_{\text{eq}}(m, x = x_0)$ .
6:    $x_{\text{max}} = 1000$                            ▷ Set  $x_{\text{max}} = 100$  for the far-field scheme.

7:   while  $x_0 < x_{\text{max}}$  do
8:      $x_p = x_0 + h/2$ 
9:      $g_p = g(m, x_p)$     ▷ Save some time by computing  $g$  and its square
   root first.
10:     $g_{p,\text{sqrt}} = \sqrt{g_p}$ 
11:     $c = (\Lambda/x_p^2) * (1 + g_D(m, x_p)/3) * g_{p,\text{sqrt}}$     ▷  $g_D(m, x)$  is the
   derivative term in Eq. 86.
12:     $\Omega_{\text{eq},p} = (4.03688 * 10^7) * m * (g_\chi/g_p) * x_p^{3/2} * \exp(-x_p)$ 
13:     $b = c * \Omega_{\text{eq},p}^2$ 
14:     $\alpha = 1 + (1/2) * b * c * h^2$     ▷ Note that  $\alpha$  is the Möbius function
15:     $\beta = b * h$ 
16:     $\gamma = c * h$ 
17:     $\delta = \alpha$ 

18:     $\Omega_0 = (\alpha * \Omega_0 + \beta)/(\gamma * \Omega_0 + \delta)$     ▷ Update  $\Omega_0$  with the Möbius
   functions.
19:     $x_0 = x_0 + h$ 
20:  end while
21:   $\Omega_\infty = \Omega_0$     ▷ Set  $\Omega_\infty = \Omega_0/(1 + \Omega_0 * \Lambda * \mathcal{G}(m, x = 100))$  for the
   far-field scheme
22:  return  $\Omega_\infty$ 
23: end function

```

10 Results

For it would suffice for them to take their pencils in their hands and to sit down at the abacus, and say to each other (and if they so wish also to a friend called to help): Let us calculate.

Gottfried Leibniz, *Dissertatio de Arte Combinatoria*

Using Algorithm 1 we can finally solve the original problem of determining what set of $(m_\chi, \langle \sigma v_{\text{rel}} \rangle)$ is allowed by observation. We will use the results in Section 8 and consider the individual cases of s-wave, p-wave and resonant annihilation.

10.1 S-Wave

For s-wave annihilation, the cross section is parametrized as $\langle \sigma v_{\text{rel}} \rangle = \bar{\alpha} \times 10^{-26} \text{ cm}^3 \text{ s}^{-1}$ (see Eq. (73)). We scan 10^2 logarithmically distributed points in the range $m_\chi \in (10^{-1}, 10^4)$ GeV and 10^2 linearly distributed points in $\bar{\alpha} \in (1, 6)$ for a total of 10^4 points. For each point, we compute Ωh^2 ; if this quantity satisfies $0.118 \leq \Omega h^2 \leq 0.121$ then we consider it consistent with the observed dark matter relic density. The resulting (m_χ, α) contour is shown in Figure 12 for the $g(T)$ of Ref. [67] and of this work. It should be noted that, while each contour has a different $g(T)$, each was generated using the Möbius scheme in Algorithm 1. This is not the same method of solving the Boltzmann

equation used in Ref. [67]. The shape of the contour is in agreement with Figure 5 of Ref. [67] but is shifted $\approx 0.1 \times 10^{-26} \text{ cm}^3\text{s}^{-1}$ down. This is due to the fact that Ref. [67] took $\Omega h^2 = 0.11$ and we take $\Omega h^2 \approx 0.12$ which is enough to account for the $\approx 3\%$ difference. This result validates our method of solving the Boltzmann equation and our approximation for $g(T)$. The large variation in the contour for $1 \lesssim x \lesssim 10$ is due to the large change in $g(T)$ over the QCD phase transition. The effect of varying the internal degrees of freedom g_χ for our $g(T)$ is shown in Figure 13.

10.2 P-Wave

For p-wave annihilation, the cross section is parametrized by the constant β via $\sigma v_{\text{rel}} = \beta v_{\text{rel}}^2$, so that $\langle \sigma v_{\text{rel}} \rangle = 6\beta/x$. We define $\beta = \bar{\beta} \times 10^{-25} \text{ cm}^3\text{s}^{-1}$ (see Eq. (75)). We scan 10^2 logarithmically distributed points in the range $m_\chi \in (10^{-1}, 10^4)$ GeV and 10^2 linearly distributed points in $\bar{\beta} \in (1, 4)$ for a total of 10^4 points. For each point, we compute Ωh^2 ; if this quantity satisfies $0.118 \leq \Omega h^2 \leq 0.121$ then we consider it consistent with the observed dark matter relic density. The resulting (m_χ, β) contour is shown in Figure 14 for the $g(T)$ of Ref. [67] and of this work. The difference between the two results gives us some idea of the modelling uncertainty on $g(T)$. As

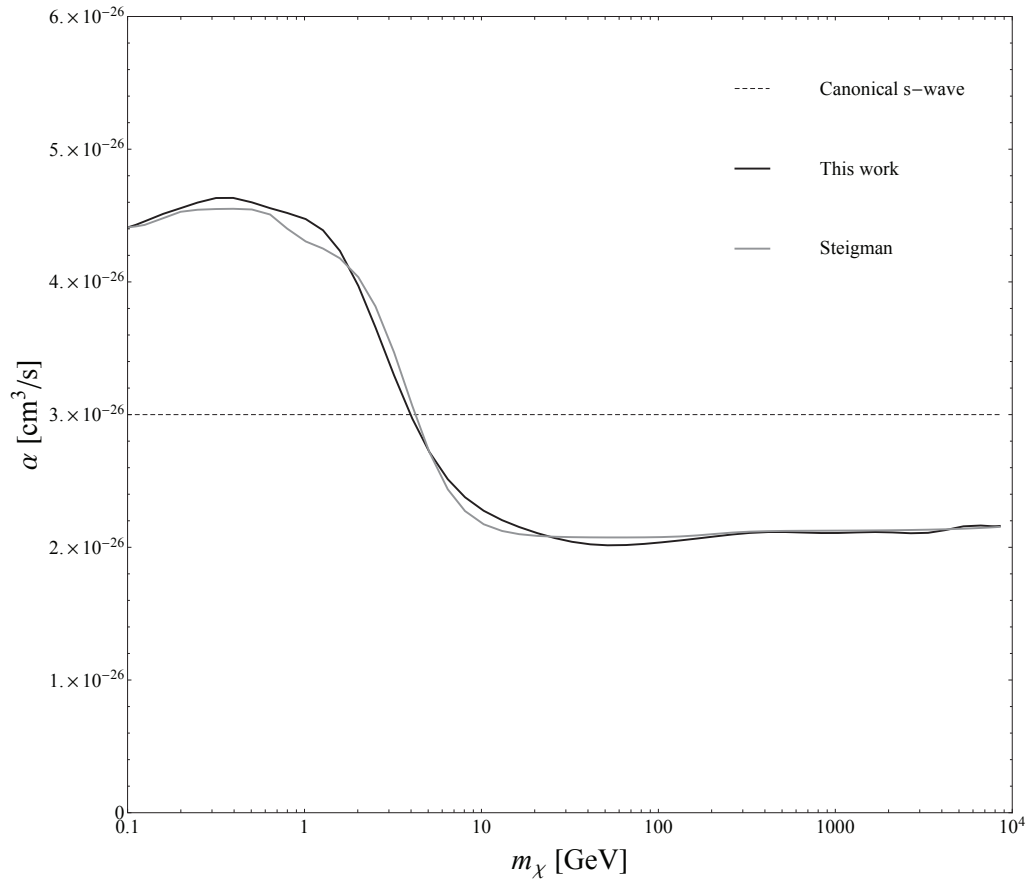


Figure 12: The value of α as a function of m_χ for s-wave annihilation with $g_\chi = 2$ using the Möbius scheme of Algorithm 1. For s-wave annihilation, the thermally averaged cross section is equal to α . Results are shown using the $g(T)$ of Ref. [67] (gray line) and this work (black line). The dashed horizontal black line is the canonical value $\langle\sigma v_{\text{rel}}\rangle = 3 \times 10^{-26} \text{cm}^3 \text{s}^{-1}$.

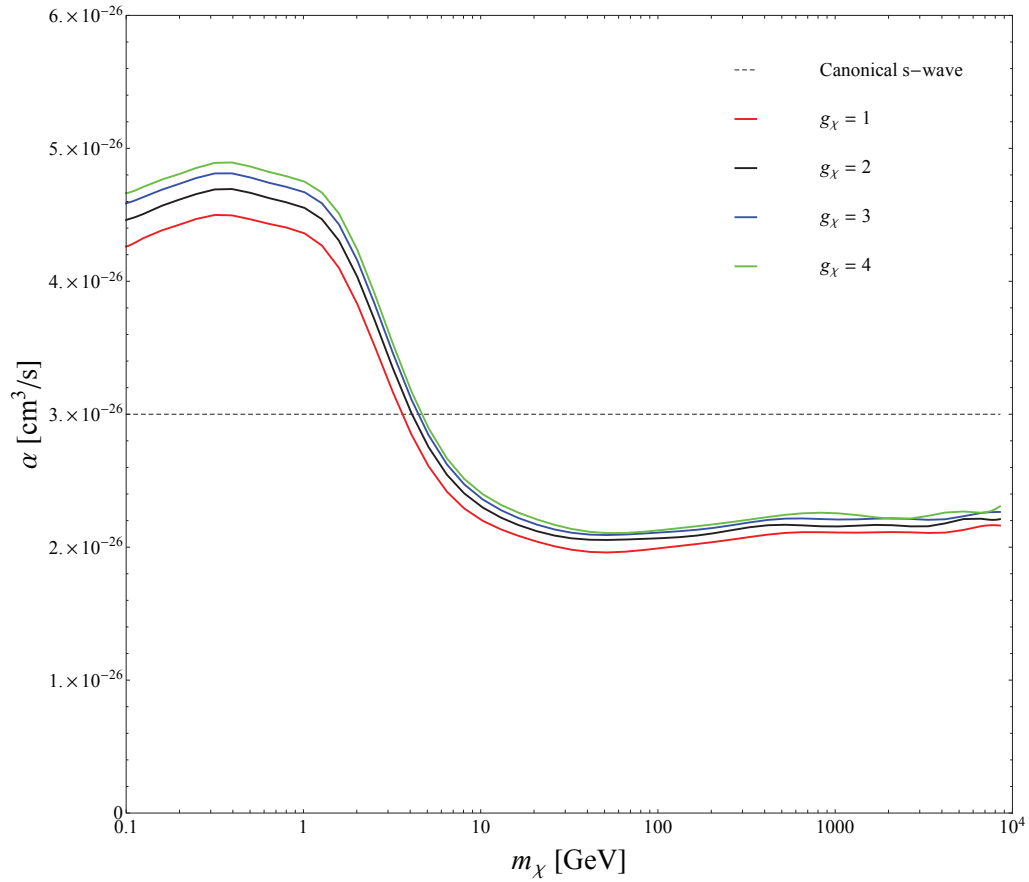


Figure 13: The effect of the number of internal degrees of freedom g_χ on the required cross section for s-wave annihilation. The particle types corresponding to each g_χ are given in Table 11. These results were all calculated using the $g(T)$ of this work and the Möbius scheme of Algorithm 1. Note that the general magnitude of α increases with increasing g_χ .

in the s-wave case, each contour was computed using Algorithm 1. To determine the canonical expectation, we use $\langle\sigma v_{\text{rel}}\rangle = 3 \times 10^{26} \text{ cm}^3\text{s}^{-1}$ along with the approximation discussed in Section 8.3.1 that freeze-out happens at $x = 20$. Since $\langle\sigma v_{\text{rel}}\rangle = 6\beta/x$, we quickly find that the canonical expectation is $\beta = 1 \times 10^{-25} \text{ cm}^3\text{s}^{-1}$. The effect of varying the number of internal degrees of freedom g_χ for our $g(T)$ is shown in Figure 15.

There are two key features to note in Figure 14. The first is that the canonical approximation obtained from taking $x = 20$ undershoots the true value of the annihilation cross section by a factor of ~ 2 . The second is that, unlike the s-wave annihilation in Figure 12, the required cross section increases monotonically for m_χ above about 10 GeV. To understand why this increase happens, let us consider the range of possible temperature values in this regime. Suppose that m_χ is very large - on the order of 10^4 GeV. Then, since $x = m_\chi/T$ and $1 \leq x \leq 1000$, we see that the integration of the Boltzmann equation runs from $T = 10^4$ GeV to $T = 10$ GeV. Figure 10 shows that $g(T)$ is approximately constant for T between 10^4 GeV and 10^2 GeV and then experiences a small dip between 100 GeV and 10 GeV. By this point in the integration x is already very large, so $d\Omega/dx$ in Eq. (76) is very small and the change in $g(T)$ has almost no effect. The net result is

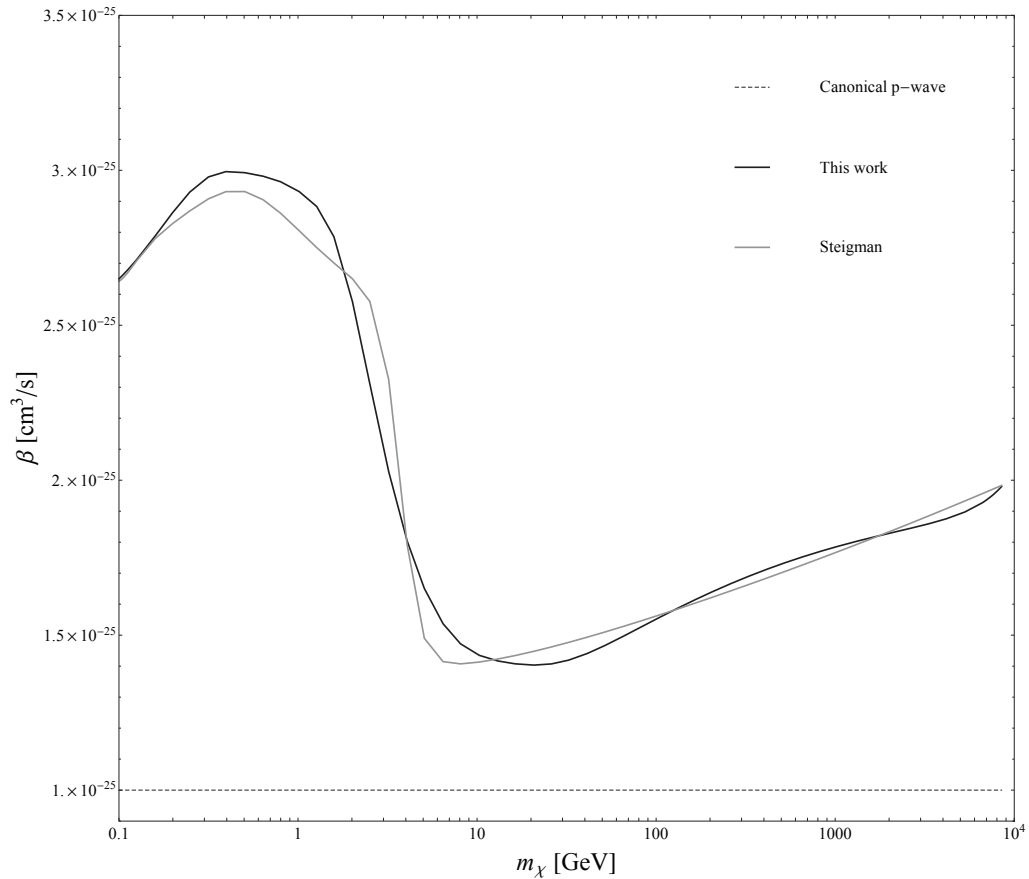


Figure 14: The value of β as a function of m_χ for p-wave annihilation with $g_\chi = 2$ using the Möbius scheme of Algorithm 1. For p-wave annihilation, the thermally averaged cross section is equal to $6\beta/x$. Results are shown using the $g(T)$ of Ref. [67] (black line) and this work (blue line). The dashed horizontal black line is the canonical value $\beta = 1 \times 10^{-25} \text{ cm}^3\text{s}^{-1}$; see text for details.

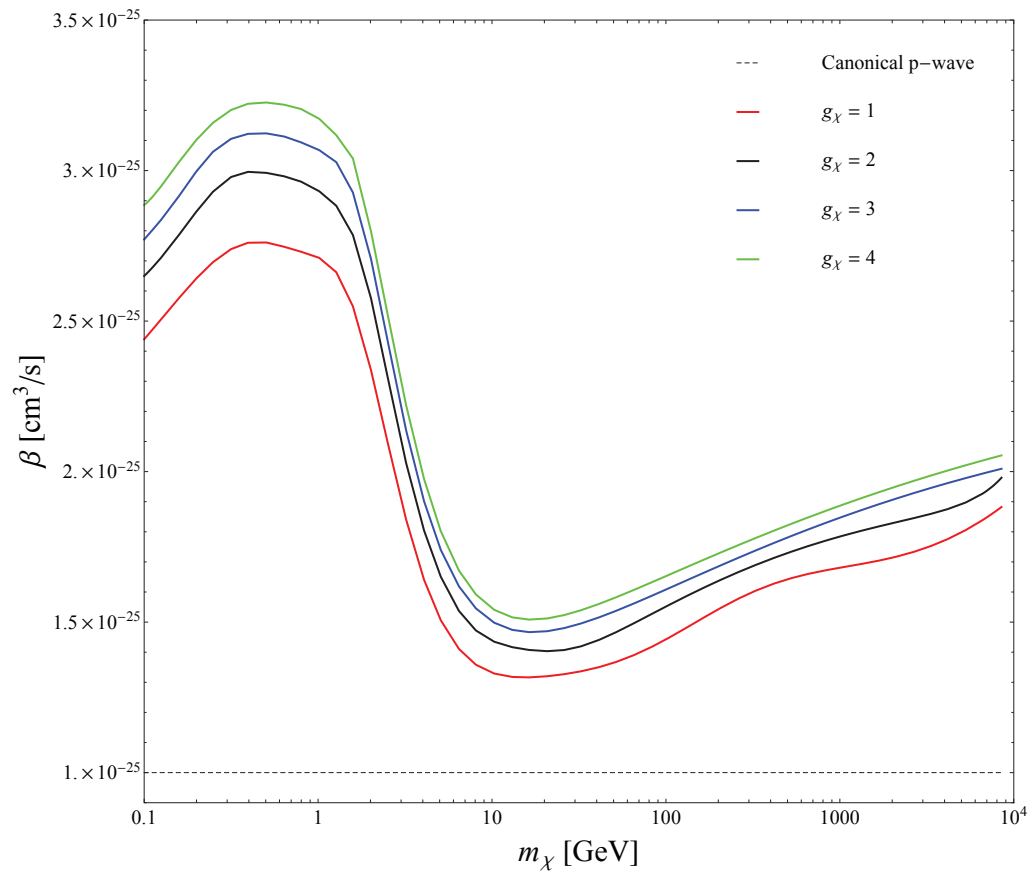


Figure 15: The effect of the number of internal degrees of freedom g_χ on the required cross section for p-wave annihilation. The particle types corresponding to each g_χ are given in Table 11. These results were all calculated using the $g(T)$ of this work and the Möbius scheme of Algorithm 1. Note that the general magnitude of β increases with increasing g_χ .

that as long as m_χ is large enough, $g(T)$ is approximately constant and equal to its maximum value $g_{\max} \approx 105$. Therefore, to understand the increase at high mass, we should study the behavior of solutions to the Boltzmann equation when $g(T) = g_{\max}$.

Let us begin with the case of s-wave annihilation. Taking $g(T) = g_{\max}$ allows us to write Eq. (74) as

$$\frac{d\Omega}{dx} = \frac{\Lambda_s \sqrt{g_{\max}}}{x^2} (\Omega_{\text{eq}}^2 - \Omega^2), \quad (121)$$

where $\Lambda_s = (9.9093)\bar{\alpha}$ and $\Omega_{\text{eq}} = (4.03688 \times 10^7)(m_\chi/\text{GeV})(g_\chi/g_{\max})x^{3/2}e^{-x}$. We are only interested in the behavior of Eq. (121) in terms of $\bar{\alpha}$ and m_χ , so we will immediately substitute numbers where appropriate. Taking $g_\chi = 2$ implies that $\Omega_{\text{eq}} = A(m_\chi/\text{GeV})x^{3/2}e^{-x}$ where $A \approx 7.69 \times 10^5$. Furthermore, we can write Eq. (121) as

$$\frac{d\Omega}{dx} = \frac{\Lambda'_s \bar{\alpha}}{x^2} (\Omega_{\text{eq}}^2 - \Omega^2), \quad (122)$$

where $\Lambda'_s \approx 100$. For $x \sim 1$, we have that $\Omega(x) \approx \Omega_{\text{eq}} = A(m_\chi/\text{GeV})x^{3/2}e^{-x}$ to a very good approximation. Physically we know that freeze-out occurs when $\Omega(x) \approx \Omega_{\text{eq}}$ is no longer true. This will happen at a value of x , x_{freeze} ,

such that $\Omega_{\text{eq}}(x_{\text{freeze}}) \sim 10\Omega_{\infty}$, where $\Omega_{\infty} = \Omega(x \rightarrow \infty)$ is the present relic abundance. We know that $\Omega(x)$ must deviate from Ω_{eq} eventually to approach Ω_{∞} ; any other order of magnitude will undershoot or overshoot this. Since $\Omega_{\infty} \sim 10^{-1}$, we have

$$A(m_{\chi}/\text{GeV})x_{\text{freeze}}^{3/2}e^{-x_{\text{freeze}}} \sim 1. \quad (123)$$

It's worth noting that the numerical solution of Eq. (123) for $m_{\chi} = 100 \text{ GeV}$ is $x_{\text{freeze}} \approx 23$, which is very close to the canonical approximation and gives some confidence that our argument is correct. The analytic solution to Eq. (123) can be written as

$$x_{\text{freeze}} = -\frac{3}{2}W_{-1}\left[\frac{-2}{3(Am_{\chi}/\text{GeV})^{2/3}}\right], \quad (124)$$

where $W_{-1}(z)$ is the Lambert W function [83]. To simplify this, we can use the fact that if z is a small real number, then $W_{-1}(z) \approx \log(-z) - \log(-\log(-z))$. Therefore,

$$x_{\text{freeze}} = 17.5 + \log\left(\frac{m_{\chi}}{\text{GeV}}\right) + \mathcal{O}\left(\log\log\frac{m_{\chi}}{\text{GeV}}\right), \quad (125)$$

where A has been replaced with its numerical value. When $\Omega(x)$ levels off from $\Omega_{\text{eq}}(x)$, to what function does it transition? For $x \gg x_{\text{freeze}}$, we have that $\Omega_{\text{eq}}(x) \approx 0$, so we can solve Eq. (122) analytically as in Section 9.5 for $\Omega_{\text{far}}^s(x)$ - the solution to Eq. (122) for large x . The result is that

$$\Omega_{\text{far}}^s(x) \simeq \frac{x\Omega_\infty}{x - \bar{\alpha}\Lambda'_s\Omega_\infty}. \quad (126)$$

Matching $\Omega_{\text{far}}^s(x)$ to $\Omega_{\text{eq}}(x)$ at x_{freeze} introduces an error of $\mathcal{O}(1)$. Since $\Omega_{\text{eq}}(x_{\text{freeze}}) = 1$ by design, the matching condition gives $\Omega_{\text{far}}^s(x_{\text{freeze}}) = 1$. Isolating the cross section coefficient gives

$$\begin{aligned} \bar{\alpha} &\simeq \frac{1 - \Omega_\infty}{\Lambda'_s\Omega_\infty} x_{\text{freeze}} \\ &\sim 1.58 + 0.09 \log\left(\frac{m_\chi}{\text{GeV}}\right). \end{aligned} \quad (127)$$

Hence, by transforming $\bar{\alpha}$ back to α , we expect

$$\alpha \simeq \left(1.58 + 0.09 \log\left[\frac{m_\chi}{\text{GeV}}\right]\right) \times 10^{-26} \text{ cm}^3\text{s}^{-1}, \quad (128)$$

when $g(T) = g_{\text{max}}$. To test this, we will repeat the s-wave annihilation calculation in Figure 12 with $g(T)$ as in Figure 10 and with $g(T) = g_{\text{max}}$. In

order to actually see the rise in α predicted at high masses, we extend the scan to include $10^{-1} < m_\chi/\text{GeV} < 10^7$. The results are shown in Figure 16. We see that the approximate analytic prediction in Eq. (128) is shifted up from the numerical result by $\approx 0.1 \times 10^{-26} \text{ cm}^2\text{s}^{-1}$, but otherwise agrees exactly. In particular, the dependence $\alpha \sim 0.09 \log(m_\chi/\text{GeV})$ seems to be accurate, which explains why the cross section increases with increasing mass. We also note that Figure 5 of Ref. [67] only considers $10^{-1} < m_\chi/\text{GeV} < 10^3$. The contour is approximately flat for $10 < m_\chi/\text{GeV} < 10^3$ so one might assume (incorrectly) that it will continue to be flat for arbitrarily high masses. Figure 16 shows that this is not true; it is simply a fortuitous cancellation of the logarithmic increase of α with the variation in $g(T)$. Setting $g(T) = g_{\text{max}}$ for all m_χ shows that the logarithmic increase is a feature of the s-wave Boltzmann equation.

Finally, we can return to the original problem of explaining the rise in the contour of Figure 14 at high masses. The analysis for the p-wave case is almost the same as the s-wave case, except we begin with Eq. (76). In direct analogy with Eq. (122), we have

$$\frac{d\Omega}{dx} = \frac{\Lambda'_p \bar{\beta}}{x^3} (\Omega_{\text{eq}}^2 - \Omega^2), \quad (129)$$

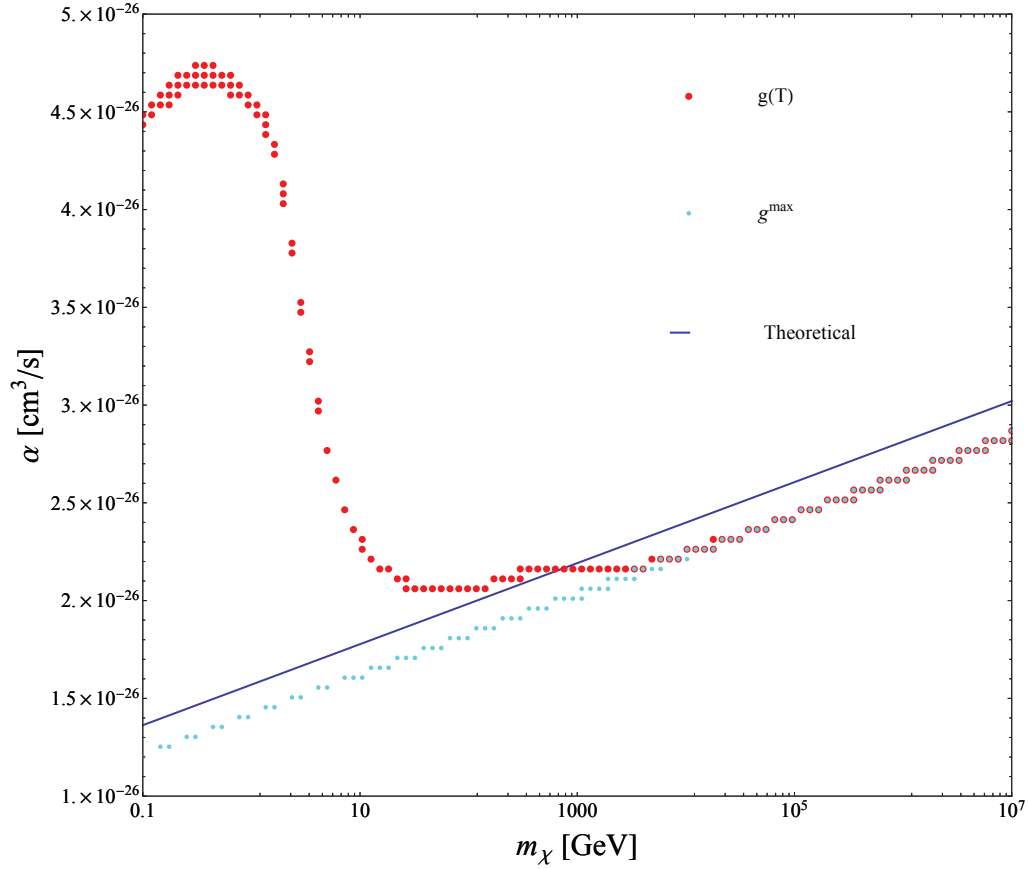


Figure 16: Illustration of the increase of the required s-wave cross section at high masses. The red dots show the same calculation as in Figure 12. The cyan dots show the same calculation as in Figure 12, except with $g(T)$ set equal its maximum value g_{\max} . The blue line is the approximate analytic prediction of Eq. (128). All calculations in this Figure have been done using $g_\chi = 2$.

where $\Lambda'_p \approx 6100$. Solving Eq. (129) in the large x regime gives $\Omega_{\text{far}}^p(x)$ as

$$\Omega_{\text{far}}^p(x) \simeq \frac{2x^2\Omega_\infty}{2x^2 - \bar{\beta}\Lambda'_p\Omega_\infty}. \quad (130)$$

Applying the matching condition $\Omega_{\text{far}}^p(x_{\text{freeze}}) \sim 1$ with x_{freeze} given by Eq. (123) as before gives

$$\begin{aligned} \bar{\beta} &\simeq \frac{2(1 - \Omega_\infty)}{\Lambda'_p\Omega_\infty} x_{\text{freeze}}^2 \\ &\simeq 0.905 + 0.103 \log\left(\frac{m_\chi}{\text{GeV}}\right) + 0.00295 \log^2\left(\frac{m_\chi}{\text{GeV}}\right), \end{aligned} \quad (131)$$

where $\log^2(x) = [\log(x)]^2$. Hence, by transforming $\bar{\beta}$ back to β , we expect

$$\beta \simeq \left(0.905 + 0.103 \log\left[\frac{m_\chi}{\text{GeV}}\right] + 0.00295 \log^2\left[\frac{m_\chi}{\text{GeV}}\right]\right) \times 10^{-25} \text{ cm}^3 \text{ s}^{-1} \quad (132)$$

when $g(T) = g_{\text{max}}$. Figure 17 shows the prediction of Eq. (132) compared with the exact numerical calculation. We see that, as in the s-wave case, the matching procedure has introduced a global error of $\approx 0.1 \times 10^{-25} \text{ cm}^3 \text{ s}^{-1}$, but otherwise the agreement is excellent.

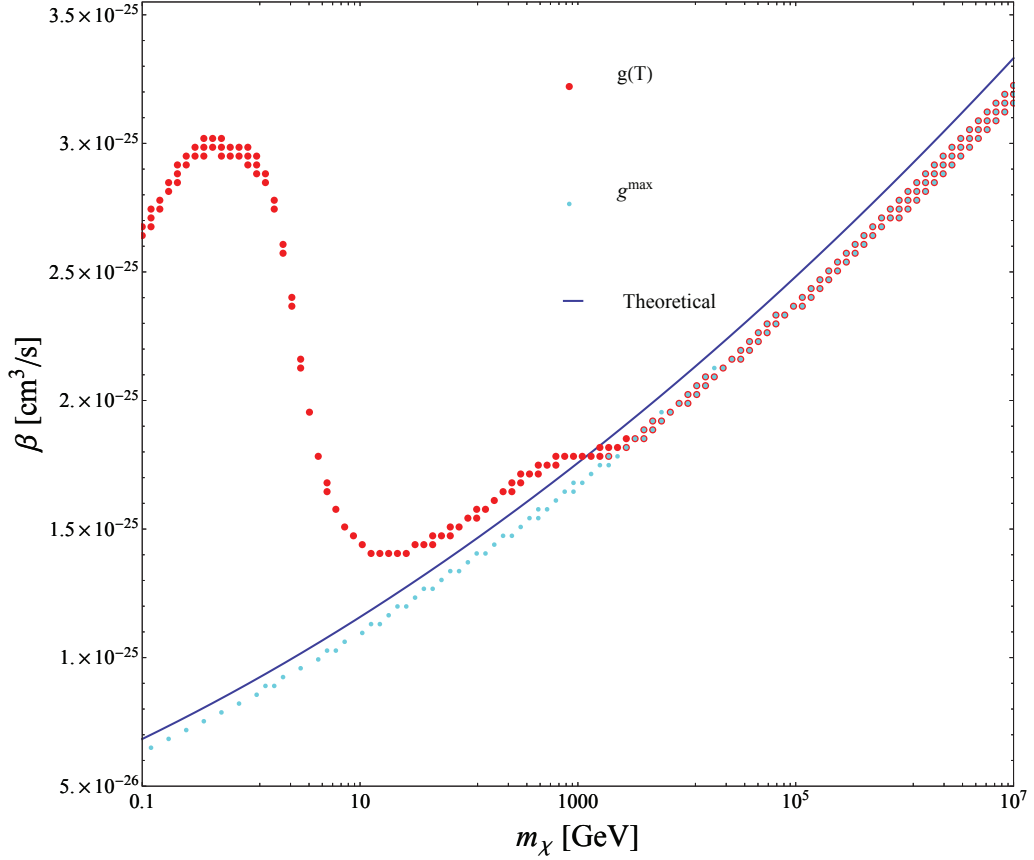


Figure 17: Illustration of the increase of the required p-wave cross section at high masses. The red dots show the same calculation as in Figure 14. The cyan dots show the same calculation as in Figure 14, except with $g(T)$ set equal its maximum value g_{\max} . The blue line is the approximate analytic prediction of Eq. (132). All calculations in this Figure have been done using $g_\chi = 2$.

10.3 Resonant Annihilation Through the Higgs Pole

For resonant annihilation, the cross section is given in Eqs. (82) and (83). We will consider the case where the mediator particle R is specifically the SM Higgs boson, which implies $m_R \approx 125$ GeV and $\Gamma_R \approx 4$ MeV. The resonant cross section, unlike the s-wave and p-wave cross sections, changes by many orders of magnitude over the integration range. Hence, we begin by computing the canonical approximation, given by setting $x = 20$ and $\langle\sigma v_{\text{rel}}\rangle = 3 \times 10^{-26} \text{ cm}^3\text{s}^{-1}$ in Eq. (82) and solving for μ as a function of m_χ . This approximation gives us some idea of the size of μ for the full calculation. Since the actual resonance peak occurs at $m_R/2 \approx 62.5$ GeV, we scan 10^2 logarithmically distributed points in the range $m_\chi \in (30, 90)$ GeV and 10^2 logarithmically distributed points in $\bar{\mu} \in (10^3, 10^7)$. For each point, we compute Ωh^2 ; if this quantity satisfies $0.118 \leq \Omega h^2 \leq 0.121$ then we consider it consistent with the observed dark matter relic density. The resulting (m_χ, μ) contour is shown in Figure 18 along with the canonical approximation for our $g(T)$ and with $g_\chi = 2$. Note that the form of the cross section given in Eq. (77) is specifically for scalar dark matter, so that only $g_\chi = 1$ (real scalar) and $g_\chi = 2$ (complex scalar) are possible (see Table 11). Repeating the calculation with $g_\chi = 1$ results in a contour which is shifted downward

from that shown in Figure 18 by only $\approx 1\%$. This effect is too small to be visible on the scale set by the large variation of μ in Figure 18.

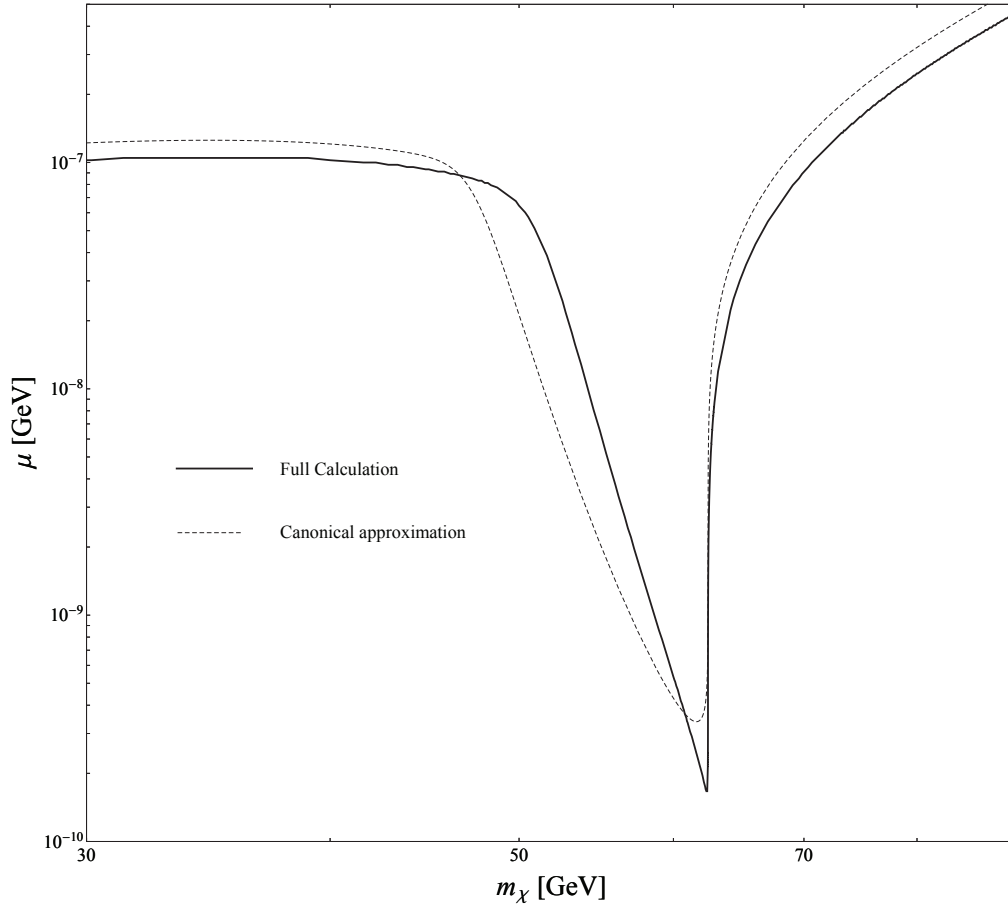


Figure 18: The value of μ as a function of m_χ for resonant annihilation through a Standard Model Higgs boson (solid black line). For resonant annihilation, the thermally averaged cross section is given in Eqs. (82) and (83). The dashed black line is the expected cross section obtained by assuming that freeze-out happens exactly at $x = 20$ (see text for details). All results were calculated using $g_\chi = 2$; the results for $g_\chi = 1$ is negligibly different.

11 Conclusions to Part 2

If people did not sometimes do silly things, nothing intelligent would ever get done.

Ludwig Wittgenstein, *Vermischte Bemerkungen*

We have calculated the thermally averaged annihilation cross section required to reproduce the observed dark matter relic density as a function of the dark matter mass for several different types of annihilation. In the case of s-wave annihilation, this calculation was performed in Ref. [67] and we were able to reproduce these results to within $\approx 10\%$ using a simplified calculation of the number of effective relativistic degrees of freedom, $g(T)$. We find, as Ref. [67] finds, that the full calculation deviates significantly from the canonical approximation, although the canonical approximation is a good estimate of the order of magnitude of the required cross section. We have provided a detailed tabulation of fitting functions for $g(T)$ and its derivatives. These may be useful as a starting point for future relic density calculations. We provide the required s-wave cross section for $g_\chi = 1, 2, 3$ and 4. The difference from the $g_\chi = 2$ calculation of Ref. [67] is at most 7%.

In the case of p-wave annihilation, we find that the canonical approximation underestimates the general magnitude of the required cross section from the full calculation by a factor of ~ 2 . We provide the required coefficient of

the v_{rel}^2 term in the p-wave cross section for $g_\chi = 1, 2, 3$ and 4. The variation with g_χ is about 10% relative to $g_\chi = 2$. We also noted that the required cross section increases monotonically for dark matter masses above 10 GeV. An investigation into the properties of the Boltzmann equation shows that, as long as $g(T)$ is constant, the required cross section increases logarithmically with the dark matter mass. This is a general feature of the Boltzmann equation, and we note that the apparent mass-independence of the required cross section in the s-wave case is due to an accidental cancellation. In particular, the required s-wave cross section is roughly constant for dark matter masses between 10 GeV and 10^4 GeV. However, if one extends the plot to include dark matter masses up to 10^7 GeV, we quickly see the logarithmic increase as advertised.

Finally, we calculate the required cross section in the case where the dark matter annihilates through a Standard Model Higgs boson. The canonical approximation differs from the full calculation by only a few percent away from the resonance, but can differ by nearly an order of magnitude when m_χ is only slightly less than half the Higgs mass. In principle, one could easily repeat this calculation for different mediator masses and widths, but it's difficult to imagine a readable way of presenting the results for a continuous

swath of parameters. One potentially useful observation is that for a mediator of a given mass, increasing its width does not change the shape of the required cross section near the resonance. For example, compare a mediator with $m = m_H$ and $\Gamma = \Gamma_H$ (i.e. the SM Higgs boson) to a mediator with $m = m_H$ and $\Gamma = 2\Gamma_H$. We find that the required cross sections for the two different mediators are identical to within less than 1% for $55 \lesssim m_\chi/\text{GeV} \lesssim 63$. We did not attempt to further quantify this, but it may be possible to make some general statements about the effect of the width by studying Eqs. (79) and (82) more closely.

All of our calculations were performed with the so-called Möbius method - a numerical scheme specifically designed for ODE classes of which the Boltzmann equation is a member. This method is particularly useful because standard explicit methods (such as Runge-Kutta) are not well-suited to stiff equations. We only considered the case of a single dark matter species, i.e. the scalar Boltzmann equation. The Möbius method also applies to a very general class of multi-dimensional ODEs which depend on the square of the dependent variable. It may be worth investigating the possibility of applying Möbius-type methods to the case of multiple dark matter species.

Appendices

A Statistical Uncertainty On the Asymmetry

Random chance was not a sufficient explanation of the Universe - in fact, random chance was not sufficient to explain random chance.

Robert A. Heinlein, *Stranger in a Strange Land*

Each event that we see has a definite p_T and p_z of the Higgs boson, but depending on whether or not a given value is less than $p_{i,j}^{\text{cut}}$ it either contributes 1 or 0 to the quantity $N(p < p_{i,j}^{\text{cut}})$. Hence, we can interpret $N(p < p_{i,j}^{\text{cut}})/N_{\text{tot}}$ as the sample mean of a set of N_{tot} Bernoulli trials with probability of success $\mathcal{P} = \int_0^{p_{i,j}^{\text{cut}}} f_{i,j}(x) dx$ where $f_{i,j}(x)$ is the underlying physical distribution of $p_{i,j}$. The expected value of the sample mean is the mean of the underlying Bernoulli distribution, \mathcal{P} . The variance of the sample mean is the the variance of the underlying Bernoulli distribution, $\mathcal{P}(1 - \mathcal{P})$, divided by the number of samples. Therefore, the expected value and variance of $A_{i,j}$ are

$$E[A_{i,j}] = 1 - 2\mathcal{P} = A_{i,j}, \quad (133)$$

$$V[A_{i,j}] = \frac{4}{N_{\text{tot}}}\mathcal{P}(1 - \mathcal{P}) = \frac{1}{N_{\text{tot}}}(1 - A_{i,j}^2). \quad (134)$$

Hence, given a measurement of $A_{i,j}$, the error on $A_{i,j}$ is

$$\sigma_{A_{i,j}} = \sqrt{\frac{1 - A_{i,j}^2}{N_{\text{tot}}}}. \quad (135)$$

Why is the statistical error zero when $A = \pm 1$? In these cases, p^{cut} is either at exactly 0 or infinity. Hence, no matter what the distributions are doing, A will be identically equal to ± 1 .

B Group Theory

If I were again beginning my studies, I would follow the advice of Plato and start with mathematics.

Galileo Galilei, *Due Nuove Scienze*

In order to really explain where quark masses come from in the Standard Model, we need some background in group theory. If for no other reason than to help future generations, we include a fairly in-depth summary of the key facts required to understand most of the group theory in particle physics. This section follows the discussions in Refs. [84, 85, 86].

B.1 Introduction to Groups

A group is a set of objects, G , along with an operation \star which acts on the objects. The following four conditions must be satisfied:

1. The closure relation: If g_1 and g_2 are elements of G , then $g_1 \star g_2$ must be an element of G .
2. The associativity relation: $(g_1 \star g_2) \star g_3 = g_1 \star (g_2 \star g_3)$ for any g_1, g_2 and g_3 .
3. The identity: There is a unique element g_0 with the property that $g_0 \star g_i = g_i \star g_0 = g_i$ for any g_i .
4. The inverse: For every element g , there exists an element h such that $h \star g = g \star h = g_0$ and we write that $h = g^{-1}$.

Note that the set G can be anything (integers, real numbers, complex numbers ...) and the operation \star can be anything (addition, modular addition, scalar multiplication, matrix multiplication ...) as long as the group conditions are satisfied.

Consider the set of integers \mathbb{Z} along with the operation $\star = +$, ordinary addition. In this case, the group elements g_i and g_j are the integers i and

j . Clearly the addition of two integers is another integer, so we have that $g_i \star g_j = i + j = g_{i+j}$ and therefore the closure relation is satisfied. It is obvious that if i, j, k are integers, then $(i + j) + k = i + (j + k)$ so the associativity relation is satisfied. If we take $g_0 = 0$, then we have $g_0 \star g_i = 0 + i = i = g_i$ and $g_i \star g_0 = i + 0 = i = g_i$ and therefore 0 is the unique identity element. For a given element g_i , if we take $h_i = -i$, then $g_i \star h_i = i - i = 0 = g_0$ and vice versa, so every element has an inverse. Therefore, the set of integers under ordinary addition is a group.

B.2 Group Classification

The *order* of a group is the number of elements it contains. If the number of elements is finite, the group itself is said to be finite - otherwise it is said to be infinite. Furthermore, a group may be discrete (such as the set of integers under addition) or continuous (such as the set of real numbers under addition).

The group with only one element is $G = \{g_0\}$, where g_0 must be the identity element. This is an example of a finite discrete group and is the only group of order 1; it is unambiguously referred to as \mathbb{Z}_1 . The group with two elements is $G = \{g_0, g_1\}$, where we must have $g_1 \star g_1 = g_0$ for the closure

relation to be satisfied. The group structure can be summarized in a table such as

(G, \star)	g_0	g_1
g_0	g_0	g_1
g_1	g_1	g_0

Note that this is the only possible group of order 2 and is referred to as \mathbb{Z}_2 .

Similarly, there is only one group of order 3, \mathbb{Z}_3 given by

(G, \star)	g_0	g_1	g_2
g_0	g_0	g_1	g_2
g_1	g_1	g_2	g_0
g_2	g_2	g_0	g_1

However, there are two groups of order 4. If the elements of a group are such that $g_i \star g_j = g_j \star g_i$, then the group is said to be *Abelian* - otherwise it is non-Abelian (the word ‘commutative’ can be used in place of ‘Abelian’).

B.3 Representations

A *representation* of a group is an assignment of a concrete object to every group element such that the structure of the group is preserved. A group may have many (even an infinity of) representations.

Consider the group of order 2, \mathbb{Z}_2 discussed previously. Let us represent this group using the integers 0 and 1 for g_0 and g_1 and the operation ‘addition mod 2’ for \star . In other words, we’re representing the group as binary addition. Now, we have that

$$g_0 \star g_0 = (0 + 0) \bmod 2 = 0 \bmod 2 = 0 = g_0,$$

$$g_0 \star g_1 = (0 + 1) \bmod 2 = 1 \bmod 2 = 1 = g_1,$$

$$g_1 \star g_0 = (1 + 0) \bmod 2 = 1 \bmod 2 = 1 = g_1,$$

$$g_1 \star g_1 = (1 + 1) \bmod 2 = 2 \bmod 2 = 0 = g_0.$$

This agrees with the group table of \mathbb{Z}_2 . Therefore, the structure of the group is preserved; since the group operation is addition, we call this the additive representation.

Let us try to represent \mathbb{Z}_2 a different way. Let us use the integers 1 and

-1 for g_0 and g_1 and the operation ‘scalar multiplication’ for \star . Then,

$$g_0 \star g_0 = 1 \times 1 = 1 = g_0,$$

$$g_0 \star g_1 = 1 \times (-1) = -1 = g_1,$$

$$g_1 \star g_0 = (-1) \times 1 = -1 = g_1,$$

$$g_1 \star g_1 = (-1) \times (-1) = 1 = g_0.$$

So we see that the structure of the group is still preserved. Since the group operation is multiplication, we call this the multiplicative representation.

One of the most useful types of representation is the matrix representation. In this case, we use

$$g_0 \doteq \begin{pmatrix} 1 & 0 \\ 0 & 1 \end{pmatrix}, \quad g_1 \doteq \begin{pmatrix} 0 & 1 \\ 1 & 0 \end{pmatrix},$$

along with ‘matrix multiplication’ for \star . It is easy to check that this representation preserves the group structure. Since we use 2×2 matrices, this is a matrix representation of dimension 2. A dimension 3 matrix representation

of \mathbb{Z}_2 is

$$g_0 \doteq \begin{pmatrix} 1 & 0 & 0 \\ 0 & 1 & 0 \\ 0 & 0 & 1 \end{pmatrix}, \quad g_1 \doteq \begin{pmatrix} 0 & 1 & 0 \\ 1 & 0 & 0 \\ 0 & 0 & 1 \end{pmatrix},$$

which also preserves the group structure. It's clear that a group may have matrix representations of different dimensionality. The matrix representation of dimension equal to the order of the group is called the *regular* representation.

The point is that a group may be represented by a variety of objects and operations, as long as the abstract structure which defines the group is preserved. There is only one group of order two, but as we've seen, this group has multiple representations. One other thing to note is that we can write $1 = e^{i0}$ and $-1 = e^{i\pi}$, suggesting that the group elements are in some sense 'rotations' by an angle of π . In fact, the set $\{e^{i0}, e^{i\pi/3}, e^{2i\pi/3}\}$ under scalar multiplication is a representation of \mathbb{Z}_3 . In this case, the group elements are rotations by $\pi/3$.

B.4 Reducible Representations

We saw previously that the group of order two can have a matrix representation of dimension 2 or 3. In this case, we say that the representation of dimension 3 is *reducible* because there exists a representation of lower dimension. Conversely, the representation of dimension 2 is irreducible. In order to explain this idea more concretely, let us consider a different group. The *symmetry* group of 3 objects, denoted S_3 , has a structure such that the group elements can be interpreted as permuting a string of length 3. There are $3! = 6$ permutations for such a string, and so there are 6 group elements and $\text{order}(S_3) = 6$. Suppose we have the objects ABC , then the group elements can be interpreted as

1. The identity: $g_0(ABC) = (ABC)$,
2. Moving every object to the left: $g_1(ABC) = (BCA)$,
3. Moving every object to the right: $g_2(ABC) = (CAB)$,
4. Swapping the first and second: $g_3(ABC) = (BAC)$,
5. Swapping the first and third: $g_4(ABC) = (CBA)$,
6. Swapping the second and third: $g_5(ABC) = (ACB)$,

where the group operation \star instructs us to apply the permutations from right to left. In other words, $g_3 \star g_1$ means move every object to the left then swap the first and second. It's easy to see that this is equivalent to swapping the first and third, so $g_3 \star g_1 = g_4$. On the other hand, we also have $g_1 \star g_3 = g_5$ so this group is actually non-Abelian. The rest of the operations can be determined in the same way. We have

(G, \star)	g_0	g_1	g_2	g_3	g_4	g_5
g_0	g_0	g_1	g_2	g_3	g_4	g_5
g_1	g_1	g_2	g_0	g_5	g_3	g_4
g_2	g_2	g_0	g_1	g_4	g_5	g_3
g_3	g_3	g_4	g_5	g_0	g_1	g_2
g_4	g_4	g_5	g_3	g_2	g_0	g_1
g_5	g_5	g_3	g_4	g_1	g_2	g_0

One important attribute of S_3 is that it contains a *subgroup* (a group within a group). We see that the elements $\{g_0, g_1, g_2\}$ by themselves (i.e. the first three rows and first three columns) have the exact same structure as \mathbb{Z}_3 and therefore form a subgroup of order 3.

Now, S_3 is a group of order 6, so we must have that the regular matrix representation consists of 6×6 matrices. Obviously the representation of the

identity element is \mathbb{I}_6 , the 6×6 identity matrix. The representation of g_1 , for example, is a matrix $D(g_1)$ which can be written as

$$D(g_1) \doteq \begin{pmatrix} 0 & 0 & 1 & 0 & 0 & 0 \\ 1 & 0 & 0 & 0 & 0 & 0 \\ 0 & 1 & 0 & 0 & 0 & 0 \\ 0 & 0 & 0 & 0 & 1 & 0 \\ 0 & 0 & 0 & 0 & 0 & 1 \\ 0 & 0 & 0 & 1 & 0 & 0 \end{pmatrix}.$$

Now, suppose we use unit vectors to label the 6 possible states of the string ABC . In other words, write $|ABC\rangle = (1, 0, 0, 0, 0, 0)^T$, $|BCA\rangle = (0, 1, 0, 0, 0, 0)^T$ etc. It's easy to see that $D(g_1)|ABC\rangle = |BCA\rangle$ as we would expect.

There is another possibility; we can write $|ABC\rangle = (1, 2, 3)^T$, $|BCA\rangle = (2, 3, 1)^T$. In this case, we see that the representation

$$D(g_1) \doteq \begin{pmatrix} 0 & 1 & 0 \\ 0 & 0 & 1 \\ 1 & 0 & 0 \end{pmatrix}$$

has the property that $D(g_1)|ABC\rangle = |BCA\rangle$, but in this case we have a

representation of dimension 3. Evidently, it is not always the case that the regular representation is irreducible. Furthermore, we see that the dimension of the representation may depend on how we choose to write the set of objects the group acts on.

If X_n is a matrix, then it is the *direct sum* of a $m \times m$ matrix A_m and a $k \times k$ matrix B_k , denoted $X_n = A_m \oplus B_k$ if and only if X_n is in *block diagonal* form,

$$X_n = \begin{pmatrix} A_m & \mathbf{0} \\ \mathbf{0} & B_k \end{pmatrix},$$

where $n = m + k$. The representation of any group is reducible if it can be written in block diagonal form. Examining the matrix representation of g_1 in S_3 seen previously, we see that it is in block diagonal form, which agrees with this idea (note that *every* matrix of the group must be written in block diagonal form before we can say that the representation is reducible).

B.5 Lie Groups

A Lie group is a group that can be parametrized by one or more continuous variables. Consider the set of rotations of a line in a plane. The group is the set of angles $\theta \in [0, 2\pi)$ and the group operation is the addition of angles. In

other words, $g(\theta)$ rotates the line by an angle of θ and $g(\theta_1) \star g(\theta_2) = g(\theta_1 + \theta_2)$; performing two rotations is the same as performing one combined rotation. We can represent an element g_i as θ_i ; this is a continuous group because θ_i can continuously take any value in $[0, 2\pi)$. Therefore, $g_i \star g_j = \theta_i + \theta_j$, which is g_k for some k . We can also represent the elements as matrices of dimension 2 via

$$g(\theta) \doteq \begin{pmatrix} \cos \theta & \sin \theta \\ -\sin \theta & \cos \theta \end{pmatrix},$$

which is just a rotation matrix, as expected. It's easy to see that $g(\theta_1) \star g(\theta_2) = g(\theta_1 + \theta_2)$ via matrix multiplication and some trigonometric identities.

The most general Lie group is the group which continuously transforms points in n -dimensional complex space to other points in n -dimensional complex space. This group can be represented by $n \times n$ invertible matrices with complex entries. We call this group $GL(n, \mathbb{C})$, the *general linear group*. When this group transforms a collection of points in \mathbb{C}^n , the points stay in \mathbb{C}^n . One important point is that the elements of $GL(n, \mathbb{C})$ can be represented and thought of as $n \times n$ matrices (this is called the *fundamental* representation) but the structure of the group can also be represented by matrices of higher dimension.

It is a fact of linear algebra that when a linear transformation represented by a matrix acts on a collection of points, the volumes subtended by the points before and after are related by the determinant of the matrix. For the choice $|\det A| = 1$, the volumes are equal. For the choice $\det A = 1$, the handedness of the system is preserved (i.e. the right hand rule still works). The subgroup of the general linear group consisting of only those matrices with determinant equal to 1 is called the *special linear* group $SL(n, \mathbb{C})$.

Suppose we restrict our attention to $SL(n, \mathbb{R})$, the special linear group with only real elements. One further subgroup is those matrices whose rows and columns are orthonormal; this can be stated in matrix notation as $A^T A = \mathbb{I}$. In this case, the magnitude of a vector $v^2 = \langle v|v \rangle$ transforms as $v^2 \rightarrow \langle v|A^T A|v \rangle = \langle v|v \rangle = v^2$. In other words, *orthogonal* matrices, matrices with real entries and satisfying $A^T A = \mathbb{I}$ preserve the magnitude of vectors they transform (in general they preserve the usual dot product of two vectors). The *special orthogonal* group $SO(n)$ consists of $n \times n$ orthogonal matrices with determinant 1; when these matrices act on a collection of points, they preserve the space (\mathbb{R}), volume subtended, handedness and distances from the origin. In other words, this group represents rotations.

Generalizing to complex entries, by replacing the transpose by the con-

jugate transpose; complex matrices with the property that $A^\dagger A = \mathbb{I}$ will preserve the magnitude of a complex vector. Matrices with this property are called *unitary* matrices. The *special unitary* group $SU(n)$ consists of $n \times n$ unitary matrices with determinant 1; when these matrices act on a collection of points, they preserve the space (\mathbb{C}), volume subtended, handedness and distances from the origin. This group can represent rotations in abstract space. The group $SU(2)$ is generally used to represent spin.

We know that $SO(n)$ in general preserves the dot product $x \cdot y = x_1y_1 + x_2y_2 + \dots x_ny_n$. The group $SO(m, n)$ preserves the quantity $-x_1y_1 - x_2y_2 - \dots x_my_m + x_{m+1}y_{m+1} + \dots x_{m+n}y_{m+n}$. We note that $SO(1, 3)$ preserves the value $s^2 = -x_0y_0 + x_1y_1 + x_2y_2 + x_3y_3$, or in particular $s^2 = -c^2t^2 + x^2 + y^2 + z^2$ which is the spacetime invariant. For this reason, $SO(1, 3)$ is known as the Lorentz group; the group of ‘rotations’ in time and space.

B.6 Generators

A Lie group can be parametrized in terms of the continuous parameters $\alpha_1, \alpha_2 \dots \alpha_n$ where the elements of the group are then $g(\alpha_i)$. For an n -dimensional matrix representation D_n , we have the set of representations $D_n(g(\alpha_i))$. It is possible to write the representation in terms of a matrix

exponential, i.e. $D_n(\alpha_i) = \exp(i\alpha_j X_j)$ where X_j is a constant matrix given by $X_j = -i\partial D_n/\partial\alpha_j(\alpha_j = 0)$ and the argument in the exponential is summed over j . The X_j are referred to as the generators of the group and there is one such generator associated with every parameter required to specify a particular element of the group. The group $SO(3)$ represents rotations in 3-dimensional space; we know that there are three Euler angles, so this group will have three generators. A particular set of generators defines a particular representation of a group.

The α_n which parametrize a group together span a vector space. The generators form a basis for the vector space. Like unit vectors, they ‘point’ in some generalized direction; the parameter values themselves indicate how far to ‘go’ in that direction. The *dimension* of a Lie group is the number of generators of the group. The group $SO(3)$ has dimension 3 but $SO(2)$ has dimension 1 since only one angle is needed to parametrize rotations in a plane. A generator for $SO(2)$ could be

$$X = \frac{1}{i} \begin{pmatrix} 0 & 1 \\ -1 & 0 \end{pmatrix}.$$

Hence we can write a given element of $SO(2)$ as $D_2(\theta) = e^{i\theta X}$. One can show

by computing the matrix exponential that $D_2(\theta)$ is just the rotation matrix in two dimensions. By contrast, in the two-dimensional representation, the generators of $SU(2)$ are the Pauli matrices. There are three Pauli matrices, so $SU(2)$ is a group of dimension 3.

B.7 Lie Algebras

In the case of finite discrete groups such as \mathbb{Z}_3 seen previously, we wrote out group tables to determine the structure of the group. Once a group's group table is known, the group is fully defined. In analogy to this, for the continuous case, we define the set of all possible commutation relations between the generators $[X_i, X_j] = if_{ijk}X_k$, where the f_{ijk} are the *structure constants* of the group. The structure constants for a group do not depend on the representation of the group. Therefore, if we know the structure constants of the group, a set of matrices which satisfy the commutation relations will be a valid set of generators of the group and hence we can represent the group itself. The generators along with the commutation relations form the *Lie algebra* of the group. Explicitly, the operation $g_1(\alpha) \star g_2(\beta)$ is represented by $\exp(i\alpha_j X_j) \exp(i\beta_k X_k)$ with \star being matrix multiplication. The Baker-

Campbell-Hausdorff formula states that

$$e^{i\alpha_j X_j} e^{i\beta_k X_k} = e^{i(\alpha_j X_j + \beta_k X_k) - \frac{1}{2}[\alpha_j X_j, \beta_k X_k]},$$

so if we know all the commutation relations, we know all the $g_1 \star g_2$ and thus the structure of the group is known as claimed.

Consider the matrices T^a with entries given by $T_{bc}^a = -if_{abc}$, where f_{abc} are the structure constants. It turns out that these matrices satisfy the commutation relations $[T^a, T^b] = if_{abc}T^c$ and hence are a valid set of generators. Therefore, the structure constants themselves can be used to represent the group; this is called the *adjoint* representation. The adjoint representation consists of $n \times n$ matrices where n is the dimension of the group.

C Fitting Functions

With four parameters I can fit an elephant, and with five I can make him wiggle his trunk.

John von Neumann, quoted in *A meeting with Enrico Fermi*

The Boltzmann equation (Eq. (55)) depends on the number of effective relativistic degrees of freedom $g(T)$ defined in Section 8 as well as its derivatives. In this section, we tabulate the fitting functions which were determined

i	a_i	b_i	c_i
0	54.4001847325632	0	0
1	-5.21851385605901	5.73384667545766	-1.39103982795970
2	-5.23428081152995	0.554397127291908	-1.380735947821070
3	-4.473230186533089	4.52994948502524	-1.27420658287623
4	7.97846055610160	1.834385570168683	1.263924455391742
5	1.748694915398551	11.00386955238206	1.27606401011004
6	1.746500250487622	4.52615329025027	1.377325782935213
7	15.71263908984222	2.128089878975963	1.37860247401252
8	5.23648738822757	1.11712494694123	1.37929429957152
9	1.74530444893990	0.632261515283890	1.379669331581412
10	1.944474854677174	30.2667128960069	4.2754508483654

Table 12: Coefficients of Eq. (136) for this work.

to speed up the numerical evaluation of these terms.

C.1 Fit: $g(T)$

The fitting function for the effective number of relativistic degrees of freedom $g(T)$ defined in Eq. (65) is given by

$$g(T) = a_0 + \sum_{i=1}^{10} a_i \tanh(b_i + c_i \ln T), \quad (136)$$

where the coefficients are given in Table 12 for $g(T)$ in Eq. (65) and in Table 13 for the $g(T)$ of Figure 5 in Ref. [67]. For verification purposes, our g has $g(T = 1) = 75.56696556119$ and the g of Ref. [67] has $g(T = 1) = 76.580116066049$.

i	a_i	b_i	c_i
0	0	0	0
1	15.65986624170187	6.46025601017189	-1.726053208263437
2	-26.70504095394427	5.40693162761880	-1.438285968750500
3	12.45532076318792	29.21883859212544	-1.171863321844933
4	69.1475141572348	1.056300423423517	-0.00381309388077595
5	5.085877251800023	2.682137542579444	0.966434746234678
6	11.70667984596390	0.372861819237716	1.223195852543570
7	3.11773724692379	10.7905209996929	1.465246573387031
8	-11.53628319634140	30.29176965394856	1.492849543678854
9	3.516901481850295	2.730682302108746	3.492713189962700
10	16.66009546742754	6.57613365535683	4.00544572429150

Table 13: Coefficients of Eq. (136) for $g(T)$ in Figure 5 of Ref. [67].

i	a_i	b_i	c_i
1	0.1168587537427299	1.039827423073069	-3.77788936703736
2	0.2083558250203382	0.560185457793934	0.553096452590331
3	0.65851311885171	1.779024535544066	1.680695971952689
4	0.571067275117574	4.26665030019122	2.148990896042849
5	0.1958396755995783	2.44529545090343	3.53099115765425
6	0.906238394511875	10.77202737129058	7.11730647255778
7	0.500948061731970	1.361708147468051	8.90071654677579

Table 14: Coefficients of Eq. (137) for this work.

i	a_i	b_i	c_i
1	0.1265426976094876	0.968695355781597	-3.745251738515207
2	-0.1065426474217870	1.670918496566320	-0.1461913035489704
3	4.45897030337236	0.473657821932394	1.69327375833649
4	-4.21812230744765	0.546325305486837	1.695805703559141
5	1.76561051976980	14.18398789096893	1.714973273298307
6	0.579581950941633	1.7740524042248	7.494673453597660
7	0	0	0

Table 15: Coefficients of Eq. (137) for [67].

C.2 Fit: $g_D(T)$

The derivative term $g_D(T) = d(\ln g)/d(\ln T)$ as defined in Eq. (86) can be parametrized by the fitting function

$$g_D(T) = \sum_{i=1}^7 a_i e^{-b_i(\ln T + c_i)^2}, \quad (137)$$

where the coefficients are given in Table 14 for our $g_D(T)$ of Eq. (86) and in Table 15 for $g(T)$ in Figure 5 of Ref. [67]. For verification purposes,

our g_D has $g_D(T = 1) = 0.179868214639$ and the g_D of Ref. [67] has $g_D(T = 1) = 0.16726356713860$. These fitting functions are plotted in Figure 19.

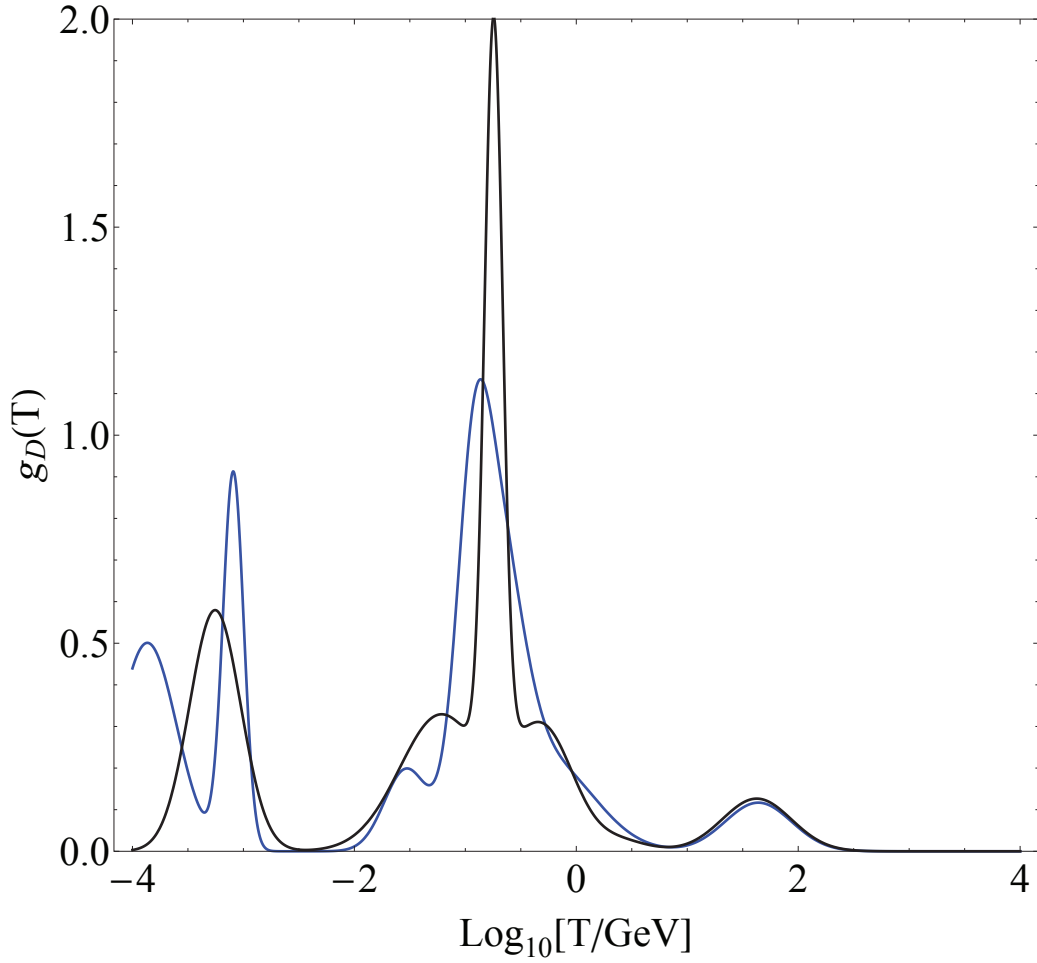


Figure 19: The derivative term $g_D(T) = d(\ln g)/d(\ln T)$ of Ref. [67] (black line) and this work (blue line). Evidently the greatest disagreement occurs for $\log_{10} T \approx -1$, around the QCD phase transition. This is to be expected since we mostly ignored the details in this region.

i	a_i	b_i	c_i
1	0.0406468843802251	3.72439163073604	-4.76823885107540
2	-0.3829258817223047	1.939073906384092	-1.747877154843337
3	-0.700809298057462	2.16454994052473	-1.176915971546974
4	0.943187092338300	1.662956472600760	-0.982369395455364
5	-1.780694703122041	1.204418095590076	-0.0856646655396654
6	0.1318310343723686	5.42996050325933	4.21198482628250

Table 16: Coefficients of Eq. (138) for this work.

i	a_i	b_i	c_i
1	-0.1090299355299574	9.69450212970584	-7.70722064617005
2	0.1295891011161402	3.99601209044486	-3.268738872484690
3	-0.271503696990882	1.89345068009048	-1.502243757888103
4	-0.057625564594923	4.82061135507871	-1.252403579373817
5	-1.952294674170088	1.169763039465806	0.0341773536632071
6	0.4253427148604513	2.696584980535049	1.400402451518257

Table 17: Coefficients of Eq. (138) using $g(T)$ in Figure 5 of Ref. [67].

C.3 Fit: $\mathcal{G}(m_\chi, x = 100)$

The fitting function for the quantity $\mathcal{G}(m_\chi, x = 100)$ defined in Eq. (116) can be parametrized as

$$\log_{10} \mathcal{G}(m_\chi, x = 100) = \sum_{i=1}^6 a_i \tanh(b_i + c_i \log_{10} T), \quad (138)$$

where the coefficients are given in Table 16 for our $\mathcal{G}(m_\chi, x = 100)$ of Eq. (116) and in Table 17 using the $g(T)$ in Figure 5 of Ref. [67]. For verification purposes, our \mathcal{G} has $\mathcal{G}(m_\chi = 1 \text{ GeV}, x = 100) \approx 0.03260726832243$ and the

\mathcal{G} of Ref. [67] has $\mathcal{G}(m_\chi = 1 \text{ GeV}, x = 100) \approx 0.03279461459171$. These functions are plotted in Figure 20.

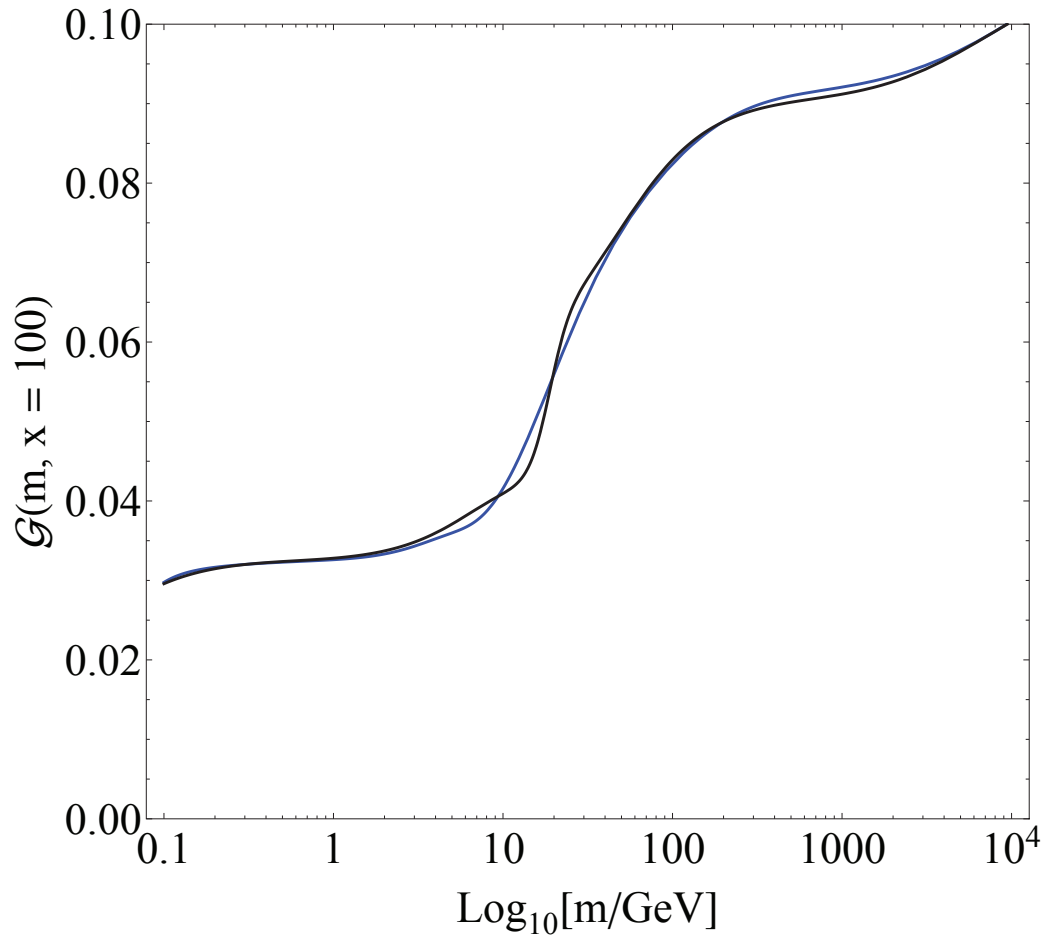


Figure 20: The function $\mathcal{G}(m, x = 100)$ of Ref. [67] (black line) and this work (blue line).

D Evaluation of the Thermally Averaged Resonant Annihilation Cross Section

I could never resist an integral.

Godfrey H. Hardy, quoted in *Twelve Geometric Essays*

The evaluation of the thermally averaged annihilation cross section is very simple when σv_{rel} is written as a polynomial in v_{rel} . For resonant annihilation, σv_{rel} is a somewhat complicated rational function (Eq. (80)) and integrating over the Maxwell-Boltzmann distribution (Eq. (71)) is non-trivial. In this section we provide the details of this calculation which leads to the results reported in Eqs. (82) and (83). By substituting Eq. (80) into Eq. (72), we're left with the following integral

$$\langle \sigma v_{\text{rel}} \rangle = \frac{x^{3/2} \mu^2 \gamma_R}{8\pi^{1/2} m_\chi^4} \int_0^\infty \frac{v_{\text{rel}}^2 e^{-xv_{\text{rel}}^2/4}}{(v_{\text{rel}}^2 - \epsilon_R)^2 + \gamma_R^2} dv_{\text{rel}}. \quad (139)$$

For simplicity, let us drop the subscripts R and 'rel' and the constants out in front. Let us further consider the integral itself to be a function of x and γ via

$$I(x, \gamma) = \int_0^\infty \frac{v^2 e^{-xv^2/4}}{(v^2 - \epsilon)^2 + \gamma^2} dv. \quad (140)$$

We can use differentiation under the integral sign to write this as

$$I(x, \gamma) = -4 \frac{\partial}{\partial x} \int_0^\infty \frac{e^{-xv^2/4}}{(v^2 - \epsilon)^2 + \gamma^2} dv. \quad (141)$$

Now let us treat γ as a Laplace parameter. Taking the inverse Laplace transform of the integrand gives

$$\begin{aligned} \mathcal{L}^{-1}[I(x, \gamma), t] &= -4 \frac{\partial}{\partial x} \int_0^\infty \cos(t(v^2 - \epsilon)) e^{-xv^2/4} dv \\ &= -4 \frac{\partial}{\partial x} \operatorname{Re} \int_0^\infty e^{it(v^2 - \epsilon)} e^{-xv^2/4} dv \\ &= -4 \frac{\partial}{\partial x} \operatorname{Re} \left[e^{-i\epsilon t} \int_0^\infty e^{-(x/4 - it)v^2} dv \right]. \end{aligned} \quad (142)$$

With the transformation $u = (x/4 - it)v$, the remaining integral can be directly evaluated as

$$\mathcal{L}^{-1}[I(x, \gamma), t] = -4\pi^{1/2} \frac{\partial}{\partial x} \operatorname{Re} \left[\frac{e^{-i\epsilon t}}{\sqrt{x - 4it}} \right]. \quad (143)$$

Now we can take the Laplace transform to get back to γ space,

$$\begin{aligned}
I(x, \gamma) &= -4\pi^{1/2} \frac{\partial}{\partial x} \operatorname{Re} \mathcal{L} \left[\frac{e^{-iet}}{\sqrt{x-4it}}, \gamma \right] \\
&= -4\pi^{1/2} \frac{\partial}{\partial x} \operatorname{Re} \mathcal{L} \left[\frac{1}{\sqrt{x-4it}}, \gamma + i\epsilon \right] \\
&= -4\pi^{1/2} \operatorname{Re} \frac{\partial}{\partial x} \mathcal{L} \left[\frac{1}{\sqrt{x-4it}}, \gamma + i\epsilon \right], \tag{144}
\end{aligned}$$

where evidently the real part and the derivative commute. The Laplace transform integral reads

$$\mathcal{L} \left[\frac{1}{\sqrt{x-4it}}, s \right] = \int_0^\infty \frac{e^{-st}}{\sqrt{x-4it}} dt. \tag{145}$$

Making the substitution $u = \sqrt{x-4it}$ leads to

$$\mathcal{L} \left[\frac{1}{\sqrt{x-4it}}, s \right] = \frac{i}{2} e^{isx/4} \int_{\sqrt{x}}^\infty e^{-isu^2/4} du. \tag{146}$$

Making the substitution $w = \sqrt{isu}/2$ leads to

$$\begin{aligned}
\mathcal{L} \left[\frac{1}{\sqrt{x-4it}}, s \right] &= \frac{i}{\sqrt{is}} e^{isx/4} \int_{\sqrt{isx}/2}^\infty e^{-w^2} dw \\
&= \frac{i}{\sqrt{is}} e^{isx/4} \frac{\pi^{1/2}}{2} \left(\frac{2}{\pi^{1/2}} \int_0^{\sqrt{isx}/2} e^{-w^2} dw \right). \tag{147}
\end{aligned}$$

Now we note that the term in brackets is exactly the definition of the complementary error function, hence the result of the Laplace transform is

$$\mathcal{L} \left[\frac{1}{\sqrt{x - 4it}}, s \right] = \frac{i\pi^{1/2}}{\sqrt{is}} e^{isx/4} \operatorname{erfc}(\sqrt{isx}/2), \quad (148)$$

$$\mathcal{L} \left[\frac{1}{\sqrt{x - 4it}}, \gamma + i\epsilon \right] = \frac{i\pi^{1/2}}{\sqrt{-\epsilon + i\gamma}} e^{x(-\epsilon + i\gamma)/4} \operatorname{erfc} \left(\sqrt{x(-\epsilon + i\gamma)}/2 \right). \quad (149)$$

To compare this with the text, let us put $\theta = \sqrt{x(-\epsilon + i\gamma)}/2$. Making this substitution gives

$$\mathcal{L} \left[\frac{1}{\sqrt{x - 4it}}, \gamma + i\epsilon \right] = \frac{i\pi^{1/2}\sqrt{x}}{2\theta} e^{\theta^2} \operatorname{erfc}(\theta). \quad (150)$$

Returning to the original integral from Eq. (144), we have

$$I(x, \gamma) = -2\pi \operatorname{Re} \frac{\partial}{\partial x} \left[\frac{i\sqrt{x}}{\theta} e^{\theta^2} \operatorname{erfc}(\theta) \right]. \quad (151)$$

Since $\theta'(x) = \theta/2x$, one quickly finds that

$$\begin{aligned} I(x, \gamma) &= -2\pi \operatorname{Re} \left[-\frac{i}{\pi^{1/2}\sqrt{x}} + \frac{i}{\sqrt{x}} \theta e^{\theta^2} \operatorname{erfc}(\theta) \right] \\ &= -\frac{2\pi}{\sqrt{x}} \operatorname{Re} \left[i\theta e^{\theta^2} \operatorname{erfc}(\theta) \right], \end{aligned} \quad (152)$$

where we have used the fact that x is real, so $\text{Re}[-i/\pi^{1/2}\sqrt{x}] = 0$. Combining this with Eq. (139) gives the final result,

$$\langle \sigma v_{\text{rel}} \rangle = -\frac{\sqrt{\pi}\mu^2}{4m_x^4} x \text{Re} \left[i\theta e^{\theta^2} \text{erfc}(\theta) \right], \quad (153)$$

which is exactly what we wanted to show.

References

- [1] G. Aad *et al.* [ATLAS Collaboration], “Observation of a new particle in the search for the Standard Model Higgs boson with the ATLAS detector at the LHC,” Phys. Lett. B **716**, 1 (2012) [arXiv:1207.7214 [hep-ex]].
- [2] S. Chatrchyan *et al.* [CMS Collaboration], “Observation of a new boson at a mass of 125 GeV with the CMS experiment at the LHC,” Phys. Lett. B **716**, 30 (2012) [arXiv:1207.7235 [hep-ex]].
- [3] V. Khachatryan *et al.* [CMS Collaboration], “Precise determination of the mass of the Higgs boson and tests of compatibility of its couplings with the standard model predictions using proton collisions at 7 and 8 TeV,” Eur. Phys. J. C **75**, no. 5, 212 (2015) [arXiv:1412.8662 [hep-ex]].
- [4] G. Aad *et al.* [ATLAS Collaboration], “Measurements of the Higgs boson production and decay rates and coupling strengths using pp collision data at $\sqrt{s} = 7$ and 8 TeV in the ATLAS experiment,” Eur. Phys. J. C **76**, no. 1, 6 (2016) [arXiv:1507.04548 [hep-ex]].
- [5] G. Aad *et al.* [ATLAS Collaboration], “Search for the Standard Model Higgs boson produced in association with top quarks and decaying into

- $b\bar{b}$ in pp collisions at $\sqrt{s} = 8$ TeV with the ATLAS detector,” Eur. Phys. J. C **75**, no. 7, 349 (2015) [arXiv:1503.05066 [hep-ex]].
- [6] G. Aad *et al.* [ATLAS Collaboration], “Search for $H \rightarrow \gamma\gamma$ produced in association with top quarks and constraints on the Yukawa coupling between the top quark and the Higgs boson using data taken at 7 TeV and 8 TeV with the ATLAS detector,” Phys. Lett. B **740**, 222 (2015) [arXiv:1409.3122 [hep-ex]].
- [7] G. Aad *et al.* [ATLAS Collaboration], “Search for the $b\bar{b}$ decay of the Standard Model Higgs boson in associated $(W/Z)H$ production with the ATLAS detector,” JHEP **1501**, 069 (2015) [arXiv:1409.6212 [hep-ex]].
- [8] V. Khachatryan *et al.* [CMS Collaboration], “Search for a Standard Model Higgs Boson Produced in Association with a Top-Quark Pair and Decaying to Bottom Quarks Using a Matrix Element Method,” Eur. Phys. J. C **75**, no. 6, 251 (2015) [arXiv:1502.02485 [hep-ex]].
- [9] V. Khachatryan *et al.* [CMS Collaboration], “Search for the associated production of the Higgs boson with a top-quark pair,” JHEP **1409**, 087 (2014) [Erratum: JHEP **1410**, 106 (2014)] [arXiv:1408.1682 [hep-ex]].

- [10] S. Chatrchyan *et al.* [CMS Collaboration], “Search for the standard model Higgs boson produced in association with a W or a Z boson and decaying to bottom quarks,” *Phys. Rev. D* **89**, no. 1, 012003 (2014) [arXiv:1310.3687 [hep-ex]].
- [11] CMS Collaboration, “Search for H to $b\bar{b}$ in association with single top quarks as a test of Higgs couplings,” CMS-PAS-HIG-14-015.
- [12] S. Chatrchyan *et al.* [CMS Collaboration], “Evidence for the direct decay of the 125 GeV Higgs boson to fermions,” *Nature Phys.* **10**, 557 (2014) [arXiv:1401.6527 [hep-ex]].
- [13] G. F. Giudice and O. Lebedev, “Higgs-dependent Yukawa couplings,” *Phys. Lett. B* **665**, 79 (2008) [arXiv:0804.1753 [hep-ph]].
- [14] F. J. Botella, G. C. Branco, M. N. Rebelo and J. I. Silva-Marcos, “What if the Masses of the First Two Quark Families are not Generated by the Standard Higgs?,” arXiv:1602.08011 [hep-ph].
- [15] R. Harnik, J. Kopp and J. Zupan, “Flavor Violating Higgs Decays,” *JHEP* **1303**, 026 (2013) [arXiv:1209.1397 [hep-ph]].

- [16] M. Bauer, M. Carena and K. Gemmler, “Creating the Fermion Mass Hierarchies with Multiple Higgs Bosons,” arXiv:1512.03458 [hep-ph].
- [17] D. Ghosh, R. S. Gupta and G. Perez, “Is the Higgs Mechanism of Fermion Mass Generation a Fact? A Yukawa-less First-Two-Generation Model,” Phys. Lett. B **755**, 504 (2016) [arXiv:1508.01501 [hep-ph]].
- [18] Y. Meng, Z. Surujon, A. Rajaraman and T. M. P. Tait, “Strange Couplings to the Higgs,” JHEP **1302**, 138 (2013) [arXiv:1210.3373 [hep-ph]].
- [19] M. König and M. Neubert, “Exclusive Radiative Higgs Decays as Probes of Light-Quark Yukawa Couplings,” JHEP **1508**, 012 (2015) [arXiv:1505.03870 [hep-ph]].
- [20] G. Perez, Y. Soreq, E. Stamou and K. Tobioka, “Prospects for measuring the Higgs boson coupling to light quarks,” Phys. Rev. D **93**, no. 1, 013001 (2016) [arXiv:1505.06689 [hep-ph]].
- [21] C. Delaunay, T. Golling, G. Perez and Y. Soreq, “Enhanced Higgs boson coupling to charm pairs,” Phys. Rev. D **89**, no. 3, 033014 (2014) [arXiv:1310.7029 [hep-ph]].

- [22] G. Perez, Y. Soreq, E. Stamou and K. Tobioka, “Constraining the charm Yukawa and Higgs-quark coupling universality,” *Phys. Rev. D* **92**, no. 3, 033016 (2015) [arXiv:1503.00290 [hep-ph]].
- [23] K. A. Olive *et al.* [Particle Data Group Collaboration], “Review of Particle Physics,” *Chin. Phys. C* **38**, 090001 (2014).
- [24] C. Delaunay, R. Ozeri, G. Perez and Y. Soreq, “Probing The Atomic Higgs Force,” arXiv:1601.05087 [hep-ph].
- [25] F. Bishara, J. Brod, P. Uttayarat and J. Zupan, “Nonstandard Yukawa Couplings and Higgs Portal Dark Matter,” *JHEP* **1601**, 010 (2016) [arXiv:1504.04022 [hep-ph]].
- [26] A. L. Kagan, G. Perez, F. Petriello, Y. Soreq, S. Stoynev and J. Zupan, “Exclusive Window onto Higgs Yukawa Couplings,” *Phys. Rev. Lett.* **114**, no. 10, 101802 (2015) [arXiv:1406.1722 [hep-ph]].
- [27] A. Falkowski, F. Riva and A. Urbano, “Higgs at last,” *JHEP* **1311**, 111 (2013) [arXiv:1303.1812 [hep-ph]].

- [28] Y. Zhou, “Constraining the Higgs boson coupling to light quarks in the $H \rightarrow ZZ$ final states,” *Phys. Rev. D* **93**, no. 1, 013019 (2016) [arXiv:1505.06369 [hep-ph]].
- [29] D. J. Griffiths, “Introduction To Elementary Particles,” New York, USA: Wiley (1987) 392p.
- [30] M. E. Peskin and D. V. Schroeder, “An Introduction to quantum field theory,” Reading, USA: Addison-Wesley (1995) 842p.
- [31] C. P. Burgess and G. D. Moore, “The standard model: A primer,” Cambridge University Press, Cambridge, UK, 2012, 560p.
- [32] M. D. Schwartz, “Quantum Field Theory and the Standard Model,” Cambridge University Press, Cambridge, UK, 2014, 850p.
- [33] P. Aurenche, “The Standard model of particle physics,” hep-ph/9712342.
- [34] M. Herrero, “The Standard model,” *NATO Sci. Ser. C* **534**, 1 (1999) [hep-ph/9812242].
- [35] J. L. Rosner, “The Standard model in 2001,” hep-ph/0108195.
- [36] I. J. R. Aitchison and A. J. G. Hey, “Gauge Theories in Particle Physics: A Practical Introduction,” Bristol, UK: Higler (1989) 571p.

- [37] A. Pich, “Electroweak Symmetry Breaking and the Higgs Boson,” *Acta Phys. Polon. B* **47**, 151 (2016) [arXiv:1512.08749 [hep-ph]].
- [38] P. W. Higgs, “Broken Symmetries and the Masses of Gauge Bosons,” *Phys. Rev. Lett.* **13**, 508 (1964).
- [39] M. Malinsky, “Fun with the Abelian Higgs Model,” *Eur. Phys. J. C* **73**, 2415 (2013) [arXiv:1212.4660 [hep-ph]].
- [40] J. Goldstone, A. Salam and S. Weinberg, “Broken Symmetries,” *Phys. Rev.* **127**, 965 (1962).
- [41] T. D. Lee and C. N. Yang, “Question of Parity Conservation in Weak Interactions,” *Phys. Rev.* **104**, 254 (1956).
- [42] G. Rajasekaran, “Fermi and the Theory of Weak Interactions,” *Resonance J. Sci. Educ.* **19**, no. 1, 18 (2014) [arXiv:1403.3309 [physics.hist-ph]].
- [43] H. E. Logan, “TASI 2013 lectures on Higgs physics within and beyond the Standard Model,” arXiv:1406.1786 [hep-ph].

- [44] W. J. Murray, “Experimental high energy physics,” in the Proceedings of the School for Experimental High Energy Physics Students, Oxford, UK, August 30-September 12, 2008.
- [45] G. F. Sterman, “Partons, factorization and resummation, TASI 95,” In “Boulder 1995, QCD and beyond” 327-406 [hep-ph/9606312].
- [46] A. D. Martin, “Proton structure, Partons, QCD, DGLAP and beyond,” *Acta Phys. Polon. B* **39**, 2025 (2008) [arXiv:0802.0161 [hep-ph]].
- [47] S. Durr, “Recent Progress in Lattice QCD,” arXiv:1301.1914 [hep-lat].
- [48] N. Carrasco *et al.* [European Twisted Mass Collaboration], “Up, down, strange and charm quark masses with $N_f = 2+1+1$ twisted mass lattice QCD,” *Nucl. Phys. B* **887**, 19 (2014) [arXiv:1403.4504 [hep-lat]].
- [49] F. Maltoni, K. Mawatari and M. Zaro, “Higgs characterisation via vector-boson fusion and associated production: NLO and parton-shower effects,” *Eur. Phys. J. C* **74**, no. 1, 2710 (2014) [arXiv:1311.1829 [hep-ph]].
- [50] F. Demartin, F. Maltoni, K. Mawatari, B. Page and M. Zaro, “Higgs characterisation at NLO in QCD: CP properties of the top-

- quark Yukawa interaction,” *Eur. Phys. J. C* **74**, no. 9, 3065 (2014) [arXiv:1407.5089 [hep-ph]].
- [51] F. Demartin, F. Maltoni, K. Mawatari and M. Zaro, “Higgs production in association with a single top quark at the LHC,” *Eur. Phys. J. C* **75**, no. 6, 267 (2015) [arXiv:1504.00611 [hep-ph]].
- [52] F. Demartin, E. Vryonidou, K. Mawatari and M. Zaro, “Higgs characterisation: NLO and parton-shower effects,” arXiv:1505.07081 [hep-ph].
- [53] S. Chatrchyan *et al.* [CMS Collaboration], “Measurement of the properties of a Higgs boson in the four-lepton final state,” *Phys. Rev. D* **89**, no. 9, 092007 (2014) [arXiv:1312.5353 [hep-ex]].
- [54] J. Alwall *et al.*, “The automated computation of tree-level and next-to-leading order differential cross sections, and their matching to parton shower simulations,” *JHEP* **1407**, 079 (2014) [arXiv:1405.0301 [hep-ph]].
- [55] R. D. Ball *et al.* [NNPDF Collaboration], “Parton distributions with QED corrections,” *Nucl. Phys. B* **877**, 290 (2013) [arXiv:1308.0598 [hep-ph]].

- [56] N. P. Hartland and E. R. Nocera, “A Mathematica interface to NNPDFs,” Nucl. Phys. Proc. Suppl. **234**, 54 (2013) [arXiv:1209.2585 [hep-ph]].
- [57] M. Bahr *et al.*, “Herwig++ Physics and Manual,” Eur. Phys. J. C **58**, 639 (2008) [arXiv:0803.0883 [hep-ph]].
- [58] T. Sjostrand, S. Mrenna and P. Z. Skands, “PYTHIA 6.4 Physics and Manual,” JHEP **0605**, 026 (2006) [hep-ph/0603175].
- [59] M. Cacciari, G. P. Salam and G. Soyez, “FastJet User Manual,” Eur. Phys. J. C **72**, 1896 (2012) [arXiv:1111.6097 [hep-ph]].
- [60] P. Ko, “Review on top forward-backward asymmetry,” arXiv:1301.1410 [hep-ph].
- [61] S. Heinemeyer *et al.* [LHC Higgs Cross Section Working Group Collaboration], “Handbook of LHC Higgs Cross Sections: 3. Higgs Properties,” arXiv:1307.1347 [hep-ph].
- [62] E. W. Kolb and M. S. Turner, “The Early Universe,” Front. Phys. **69**, 1 (1990).

- [63] S. Dodelson, “Modern Cosmology,” Amsterdam, Netherlands: Academic Pr. (2003) 440p.
- [64] G. Bertone, D. Hooper and J. Silk, “Particle dark matter: Evidence, candidates and constraints,” *Phys. Rept.* **405**, 279 (2005) [hep-ph/0404175].
- [65] D. Baumann, “Cosmology,” 2008, [Lecture notes]. Retrieved from <http://www.damtp.cam.ac.uk/user/db275/Cosmology/> .
- [66] M. Drees, F. Hajkarim and E. R. Schmitz, “The Effects of QCD Equation of State on the Relic Density of WIMP Dark Matter,” *JCAP* **1506**, no. 06, 025 (2015) [arXiv:1503.03513 [hep-ph]].
- [67] G. Steigman, B. Dasgupta and J. F. Beacom, “Precise Relic WIMP Abundance and its Impact on Searches for Dark Matter Annihilation,” *Phys. Rev. D* **86**, 023506 (2012) [arXiv:1204.3622 [hep-ph]].
- [68] P. A. R. Ade *et al.* [Planck Collaboration], “Planck 2015 results. XIII. Cosmological parameters,” arXiv:1502.01589 [astro-ph.CO].
- [69] B. Li and Y. F. Zhou, “Direct detection of dark matter with resonant annihilation,” *Commun. Theor. Phys.* **64**, no. 1, 119 (2015) [arXiv:1503.08281 [hep-ph]].

- [70] G. Jungman, M. Kamionkowski and K. Griest, “Supersymmetric dark matter,” *Phys. Rept.* **267**, 195 (1996) [hep-ph/9506380].
- [71] D. Zwillinger, “Handbook of differential equations. Vol. 1,” Gulf Professional Publishing, pp. 354-360, 1998.
- [72] G. Adomian, “An investigation of the asymptotic decomposition method for nonlinear equations in physics,” *Applied Mathematics and Computation*, vol. 24, no. 1, pp. 1-17, 1987.
- [73] G. Adomian, “An adaption of the decomposition method for asymptotic solutions,” *Mathematics and Computers in Simulation*, vol. 30, no. 4, pp. 325-329, 1988.
- [74] H. Bulut and D. J Evans, “On the solution of the Riccati equation by the decomposition method,” *International Journal of Computer Mathematics*, vol. 79, no.1, pp. 103-109, 2002.
- [75] M. A. El-Tawil, A. A. Bahnasawi and A. Abdel-Naby, “Solving Riccati differential equation using Adomian’s decomposition method,” *Applied Mathematics and Computation*, vol. 157, no.2, pp. 503-514, 2004.

- [76] P.-Y. Tsai and C.-K. Chen, "An approximate analytic solution of the nonlinear Riccati differential equation," *Journal of the Franklin Institute*, vol. 347, no. 10, pp. 1850-1862, 2010.
- [77] A. R. Vahidi and M. Didgar, "An improved method for determining the solution of Riccati equations," *Neural Computing and Applications*, vol. 23, no. 5, pp. 1229-1237, 2013.
- [78] A. R. Vahidi, Z. Azimzadeh and M. Didgar, "An efficient method for solving Riccati equation using homotopy perturbation method," *Indian Journal of Physics*, vol. 87, no. 5, pp. 447-454, 2013.
- [79] A. R. Vahidi, M. Didgar and R. C. Rach, "An improved approximate analytic solution for Riccati equations over extended intervals," *Indian Journal of Pure and Applied Mathematics*, vol. 45, no. 1, pp. 27-38, 2014.
- [80] J. Biazar and M. Didgar, "Numerical Solution of Riccati Equations by the Adomian and Asymptotic Decomposition Methods over Extended Domains," *International Journal of Differential Equations*, vol. 2015, Article ID 580741, 7 pages, 2015.

- [81] J. Schiff and S. Shnider, "A Natural Approach to the Numerical Integration of Riccati Differential Equations," *SIAM Journal on Numerical Analysis*, vol. 36, no. 5, pp. 1392-1413, 1999.
- [82] W. Trench, "Elementary Differential Equations," Texas, USA: Trinity University (2013) 663p.
- [83] D. Veberi, "Lambert W Function for Applications in Physics," *Comput. Phys. Commun.* **183**, 2622 (2012) [arXiv:1209.0735 [cs.MS]].
- [84] M. B. Robinson, K. R. Bland, G. B. Cleaver and J. R. Dittmann, "A Simple Introduction to Particle Physics. Part I - Foundations and the Standard Model," arXiv:0810.3328 [hep-th].
- [85] J. Schwichtenberg, "Physics from Symmetry," Gewerbestrasse 11, Switzerland: Springer International Publishing (2015) 279p.
- [86] T. Teubner, "The standard model," in the Proceedings of the School of Experimental High Energy Physics, 2-14 September, 2007, Oxford, UK.